Ship Interactions in Arbitrary Channels

by

Brodie James Hynes

Submitted to the Department of Ocean Engineering
in partial fulfillment of the requirements for the degrees of

Bachelor of Science

and

Master of Science in Ocean Engineering

at the

MASSACHUSETTS INSTITUTE OF TECHNOLOGY

June 1998

Author ....
Department of Ocean Engineering
May 20, 1998

Certified by ....
Justin E. Kerwin
Professor of Naval Architecture
Thesis Supervisor

Certified by ....
F. Thomas Korsmeyer
Lecturer, Department of Ocean Engineering
Thesis Supervisor

Accepted by ....
J. Kim Vandiver
Chairman, Department Committee on Graduate Students

Ship Interactions in Arbitrary Channels

by
Brodie James Hynes

Submitted to the Department of Ocean Engineering
on May 20, 1998, in partial fulfillment of the
requirements for the degrees of
Bachelor of Science
and
Master of Science in Ocean Engineering

Abstract

The focus of this paper is to show the validity of the methods for calculating hydrodynamic forces and solving the equations of motion for ships passing in a channel of arbitrary topography. Previous efforts have been extended to include vertical motions, damping and restoring in the equations of motion. Scenarios involving bodies moving in a channel with a pier, a step and sinusoidal undulations in the bottom topography are explored.

Thesis Supervisor: Justin E. Kerwin
Title: Professor of Naval Architecture

Thesis Supervisor: F. Thomas Korsmeyer
Title: Lecturer, Department of Ocean Engineering

Acknowledgments

I would very much like to thank my family, the entire CHF research group, past and present, and my thesis advisor, Dr. F. Thomas Korsmeyer, for their support, understanding, tolerance and help, and my academic advisor,
Professor Justin E. Kerwin, for patiently seeing me through my undergraduate and graduate careers. My most sincere thanks to Dr. Geoghegan of the MIT Medical Center for saving my life halfway through my thesis. Thanks to my friends who helped me relieve stress during the long haul and to Amy Knowlton and the New England Aquarium for funding the "Hydrodynamic Interactions Between Ships and Whales" study [6] [5] [7]. Finally, to computers, without which, this research would be nowhere.

Contents

List of Figures

List of Tables

Chapter 1

Introduction

This paper validates the methods used for calculating hydrodynamic forces and solving the equations of motion for ships passing in a channel of arbitrary topography. In the course of this work, the previous versions of the rectangular and general Chanel codes have been modified to include vertical motions, a collision check, and damping and restoring in the equations of motion. Furthermore, studies of disparate body interactions, forces on bodies in channels of arbitrary topography, and moored ship analysis, have been performed.

1.1 Background

Most shipping accidents are due to collisions in confined waters. Ships may collide with other ships in a passing maneuver; a narrow or windy channel may prove too difficult for one ship to traverse (as in Prince William Sound, Alaska, where the Exxon Valdez ran aground on March 24, 1989); or a ship may even collide with an iceberg. Computational models offer an inexpensive, quick and accurate way to analyze actual situations and dangerous scenarios.

Many ship interaction models use 2-D strip theory to model ship interactions [3], [18], [19] and [21]. However, this theory requires the assumption that the ship is slender. In addition, channel walls, jetties and piers are limited in their geometries to something which can be described by a Green function and have vertical sides, so a channel with sloping sides, such as the Panama Canal cannot be done with 2-D strip theory [21] or periodic Green function [13]. And while not a restriction, the ships are often placed on parallel tracks with constant velocity. This method does yield results which agree with experiments [3], but it is limited in its applications due to the assumptions made.

Model tests of passing bodies pertinent to this study have been performed by Remery (1974) [18] and Cohen and Beck (1983) [3]. Remery modeled various tankers passing a moored tanker in a water depth 1.15 times the depth of the moored tanker. The ship paths and orientation were parallel. The two mooring scenarios for the second ship were captive and moored using linear springs. Forces on the captive ship were less than those on the ship moored using linear springs.

In the same vein, Cohen and Beck used foil shaped models running with a near zero bottom clearance to represent 2-D strip theory in a tow tank. The scenarios explored were the model moving with a constant drift angle in open water, moving along a single vertical wall, moving in a canal with vertical wall, and passing a second stationary model. Results for the single body from experiments and theory matched well, though theoretical predictions were low for the side force and yaw moment. The results for the two models matched well, and showed the forces on the moving model to be less than on the moored model. Experimental results also show that for reasonably small Froude numbers based on depth, the use of a rigid-lid free surface boundary condition is acceptable for shallow water.

Tuck and Newman (1974) [19] predicted the hydrodynamic sway force and yaw moment on two bodies moving on parallel paths with constant velocity using 2-D strip theory. The scenarios included steady parallel motion, a faster vessel passing a slower one, ships passing in opposite directions, and a vessel at a constant velocity passing a moored vessel. Shallow water effects were examined for the ships moving at the same velocity in the same direction, i.e. a biplane problem. Yeung and Tan

(1980) [21] continued shallow water 2-D strip theory with one body and multiple shapes for a coastline or obstacle. Using conformal mapping in the derivation of the channel Green function, they were able to model an infinite breakwater, a right angle pier, a vertical bank and anything in between. Arbitrary contour channel walls could be arrived at using a semi-numerical representation of the Green function obtained through Schwartz-Christoffel transformation. Results show a bow-in moment and an attractive force when approaching a pier or breakwater, but a bow-out moment and a repulsive force when approaching a bank at various angles.

The following is a desctription of the development of the code used in this study. The Chanel codes are descendants of WAMIT (Wave Analysis MIT), a frequency domain radiation/diffraction panel code.

The original Chanel code and general Chanel code are detailed in [9]. Both are 3-D, time domain, low order panel method programs which compute the hydrodynamic forces on one body fixed and one body moving with constant velocity in a channel. The first code represents the channel as a rectangular box by virtue of a carefully chosen Green function [13], while the other, represents the channel with panels. Both are shown to compare well with experimental results [9].

The channel code with the rectangular channel Green function was further modified by Wu [20] to model two bodies free to move in surge, sway and yaw due to their hydrodynamic interations. Wu also developed a time stepping technique that allowed the time derivative of the added mass to be computed using central difference. The equations of motion integration scheme moved from RK4 to central difference and Euler.

In the course of the research for this paper, the rectangular channel code has been updated to include the heave and pitch modes, a body collision detection scheme, and the inclusion of damping and restoring in the equations of motion. This code is used for the results of the ship passing a sphere presented in §5 and §6.2.

The general channel code has been updated to include all additions the rectangular channel code has enjoyed, including horizontal and vertical motions, collision detection, damping and restoring. The latest versions of the general channel code is used in the ship interaction experiments in §4 and §6.1.

1.2 Scope

A 3-D panel method approach will be used in this study. This study is an extension of the work done by Korsmeyer, Lee and Newman (1993) [9] and Wu (1995) [20]; the condition of steady-state velocities for the case of bodies in a paneled channel [9] is relaxed, as shown in [20] for the rectangular channel.

The present study discusses the development of a time domain panel code which takes two arbitrary paneled bodies and a paneled channel with arbitrary topography, and given initial position and velocities, steps the bodies in time, calculating velocities and accelerations to update body position and compute the forces and moments on each body. The modes of motion for each body include all but roll (surve, sway, heave, pitch and yaw). Irrotational flow is assumed and viscous effects are ignored. Surface effects may be neglected due to small length-based Froude number which allows the use of a rigid lid free surface Green function [3]. The use of a paneled channel allows for arbitrary bottom topography and analysis of the forces on ships moving in those channels.

1.3 Plan of Treatment

Chapter 2 will discuss the theory used in this study, such as potential flow, theory, equations of motion and acceleration techniques for the potential and source formulations.

Chapter 3 will go on to discuss the numerical methods and their application in the code, with a brief discussion of the acceleration technique implemented.

Chapter 4 will discuss convergence tests and verification of the code with previous versions and the results of the Yeung and Tan paper [21].

A numerical study of disparate bodies in passing, specifically a ship passing a sphere, will be discussed in Chapter 5, along with limitations encountered with disparatly proportioned bodies. A study of ship/mine collisions from WWII will be referenced as well.

Results of new cases, such as a ship and a submarine moving in a channel with an undulating bottom, a ship passing over a square trench with a submarine in the trench, a submerged spheroid moving over a step, a ship passing a ship moored with damped springs, and results of the speed increase due to fast multipole acceleration are in Chapter 6.

Chapter 7 will discuss the conclusions of the present study, the validity of the code, feasibility of the use of the code and a list of interesting scenarios the code can model.

Chapter 8 contains future uses and recommendations.

Chapter 2

Mathematical Formulation

2.1 The Laplace Equation

Assuming the fluid is ideal and the flow irrotational, the velocity in the fluid can be represented by a scalar potential, such that $\vec{V} = \nabla\phi$, where $\vec{V}$ is the fluid velocity anywhere in the fluid domain, ∇ is the gradient operator, and ϕ is the velocity potential of the fluid. Invoking the condition of conservation of mass,

$$\frac{\partial \rho}{\partial t} + \nabla \cdot [\rho \vec{V}] = 0 \tag{2.1}$$

in which, $\frac{\partial}{\partial t}$ is the partial derivative with respect to time, and ρ is the fluid density. Let us make another assumption, the fluid is incompressible and of uniform density. From these assumptions, the first term in (2.1) is zero, ρ is divided out from the second term and we see that the fluid velocity must have zero divergence, $\nabla \cdot \vec{V} = 0$. Combining this result with the fluid velocity potential, $\vec{V} = \nabla\phi$, gives Laplace's equation, our field equation

$$\nabla^2\phi = 0 \tag{2.2}$$

2.2 The Boundary Value Problem

In the case of an enclosed fluid volume with submerged bodies, there are three surfaces which are of concern: the free surface, S_F; the fluid boundary, or channel, S_C, which includes the sides, ends and bottom; and the body surface(s), S_B. Deriving the free surface boundary condition requires some physical understanding. Beginning with the linear forward speed free surface condition:

$$\left(\frac{\partial}{\partial t} - U\frac{\partial}{\partial x}\right)^2\phi + g\phi_z = 0 \tag{2.3}$$

where U is the body velocity, we non-dimensionalize using the factor $\frac{L}{g}$, where L is the length scale and g is the acceleration due to gravity, leaving

$$\left(\sqrt{\frac{L}{g}}\frac{\partial}{\partial t} - \frac{LU}{\sqrt{gL}}\frac{\partial}{\partial x}\right)^2\phi + L\phi_z = 0 \tag{2.4}$$

From this equation, we can see that if $g \to \infty$, the terms in the quantity multiplying ϕ go to zero. The physical corollary of gravity becoming infinite is that waves on the free surface would become infinitely long and wave height infinitely small, thus creating a vertically rigid free surface. This is equivalent to the zero-frequency case in the frequency domain. Another implication of infinite gravity is apparent when we examine the term in front of $\frac{\partial}{\partial x}$, $\frac{U}{\sqrt{gL}}$, the Froude number. As $g \to \infty$, the Froude number goes to zero, so this free surface condition is a low Froude number approximation. We are left with

$$\phi_z = 0 \tag{2.5}$$

A no-flux boundary condition is imposed on the channel boundary and the body surface making the complete boundary value problem (BVP):

$$\nabla^2\phi = 0 \qquad in \qquad \mathcal{V} \tag{2.6}$$

$$\phi_z = 0 \qquad on \qquad z = 0 \tag{2.7}$$

$$\hat{n} \cdot \nabla\phi = \vec{U} \cdot \hat{n} \tag{2.8}$$

$$\nabla\phi \to 0 \qquad as \qquad \vec{x} \to \infty \tag{2.9}$$

The BVP can be solved by discretizing the fluid volume. While this is computationally inexpensive, the problem arises in the unsteady problem, where the volume must be discretized after each time step. This discretization scheme becomes too complex. In this paper, we are motivated to solve the BVP using integral equations. While this method is computationally more expensive, the problem is much easier to discretize and it can be accelerated, thus making it computationally less expensive than a volume method. To take advantage of the benefits of solving the problem using integral equations, we must convert the BVP to a boundary integral equation. This is done using Green's theorem.

2.3 Green's Theorem and the Potential Formulation

Let $\vec{x} = (x, y, z)$ be an arbitrary field point and $\vec{\xi} = (\xi, \eta, \zeta)$ be an arbitrary source point, both in the fluid domain. The Green function chosen, satisfying (2.5) and (2.7), is

$$G(\vec{x};\vec{\xi}) = \frac{1}{R} + \frac{1}{R'} \tag{2.10}$$

where, the source potential and reflected source potential are

$$\frac{1}{R} = \frac{1}{\sqrt{(x-\xi)^2 + (y-\eta)^2 + (z-\zeta)^2}} \tag{2.11}$$

$$\frac{1}{R'} = \frac{1}{\sqrt{(x-\xi)^2 + (y-\eta)^2 + (z+\zeta)^2}} \tag{2.12}$$

respectively. Green's theorem ([11] (4.71)), applied to the two scalar potentials, ϕ, the scalar potential for our fluid domain, and $G(\vec{x};\vec{\xi})$, our Green function, gives

$$\iint_S [\phi G_n - G\phi_n] dS = \iiint_{\mathcal{V}} [\phi \nabla^2 G + G \nabla^2 \phi] d\mathcal{V} \tag{2.13}$$

where $S = S_F \cup S_B \cup S_C$ and $\mathcal{V}$ is the enclosed fluid volume. The first term in the right hand side goes to zero by virtue of the Green function; the second term is zero because we are enforcing Laplace's equation in the fluid domain. Thus, it is built in to the problem that the solution shall satisfy (2.2). Now we must work the rest of the boundary conditions into the integral equation. The free surface boundary conditions, $\phi_z = 0$ on $z = 0$, and $\frac{\partial}{\partial n} = \frac{\partial}{\partial z}$ on $z = 0$ yield

$$G_n = G_z = \frac{\partial}{\partial \zeta}(\frac{1}{R} + \frac{1}{R'}) = 0 \qquad on \qquad z = o \tag{2.14}$$

Thus the integral on the free surface is zero through G (again) and because we enforce $\phi_n = \phi_z = 0$ on $z = 0$, which builds another boundary condition into the problem. This leaves

$$\iint_{S_B \cup S_C} [\phi G_n - G\phi_n] dS = 0 \tag{2.15}$$

The next step is to eliminate the integral over the channel, S_C. In the infinite fluid case, $S_C \to S_\infty$ as $\vec{x} \to \infty$, we assume ϕG_n and $G\phi_n$ will decay at least as fast as R^2, the potential of a source, whereupon the integral is zero. Just as we enforced the solution of this problem to satisfy (2.2) by assuming a priori that it would, we assume that in the infinite fluid case, the integral over the boundary is zero. For the case of finite depth, there are two approaches to dealing with the integral over S_C. The first is to use the rectangular channel Green function, [13]. The second approach is to apply the no flux condition, $\hat{n} \cdot \nabla\phi = 0$, to S_C, hence not eliminating the integral. However, this leaves us with an interior Neumann problem, which by definition is an ill posed problem, since there exists a solution $\phi = C + \varphi$, where C is a constant, hence $\nabla\phi = \nabla\varphi$. To make this problem well posed, ϕ must be specified on a surface. If the channel surface is divided into a Neumann surface, S_N, and a Dirichlet surface, S_D, such that $S_C = S_N \cup S_D$, the condition $\phi = C$ may be set on the Dirichlet surface, making the problem well posed. Since C is an arbitrary constant, we may set it to zero. Considering the physical boundary suggests that the Dirichlet surface corresponds to the open ends of the channel. This has been suggested and shown in [9]. Channels have open ends, and in this study the bodies appear as dipoles at the channel ends, and ϕ far from a dipole goes to zero. By specifying ϕ on only one end of the channel, we are provided with a check that the eventual implementation works properly because ϕ should approach zero on the other channel end. This approach requires discretizing S_C.

Given we take the second approach discussed above, we are left with

$$\iint_{S_B \cup S_C} [\phi(\vec{\xi}) G_n(\vec{x}; \vec{\xi}) - G(\vec{x}; \vec{\xi}) \phi_n(\vec{\xi})] dS_\xi = 0 \tag{2.16}$$

Three of the four terms of this equation are known on S_B and S_C: G_n, G, and ϕ_n. We are left to evaluate (2.16) for ϕ. It is important to note that the Green function we chose is singular as $\vec{x} \to \vec{\xi}$. In taking the limit as we approach the singularity, we get

$$2\pi\phi(\vec{x}) - \iint_{S_B \cup S_C} (\phi(\vec{\xi})G_n(\vec{x};\vec{\xi}))dS_\xi = \iint_{S_B \cup S_C} (G(\vec{x};\vec{\xi})\phi_n(\vec{\xi}))dS_\xi \tag{2.17}$$

2.4 Source Formulation

In principal, from (2.17) we can calculate $\vec{V} = \vec{\nabla}\phi$ using finite difference in space. However, this is not very accurate in low-order panel methods. Thus, we look towards the source formulation. The source formulation can be derived from Green's Theorem, as is well known in potential theory.

Let us begin with a source in a fluid, for which we know the associated potential. The strength may be positive or negative. It is known that a surface can be made from two positive strength sources; this is the simplest form of a rigid free surface or wall. If we use many sources of varying sign and strength, it is conceivable that a more complex body or bodies could be formed, and that we could arrange the sources to satisfy the boundary conditions, $\phi_n = 0$ on S_F and S_C, and $\phi_n = \vec{U} \cdot \hat{n}$ on S_B. Then

$$\int_S \sigma(\vec{\xi})G(\vec{x};\vec{\xi})dS_\xi = \phi(\vec{x}) \tag{2.18}$$

can be shown to work by applying it in (2.2). Yet, we do not know ϕ or σ. The source strength can be solved for in the following way. By operating on both sides of (2.18) with $\hat{n} \cdot \vec{\nabla}$, ϕ is now ϕ_n, the boundary condition, which we know on S. That leaves σ as the only unknown.

$$\hat{n} \cdot \vec{\nabla} \int_S \sigma(\vec{\xi})G(\vec{x};\vec{\xi})dS_\xi = \hat{n} \cdot \vec{\nabla}\phi(\vec{x}) \tag{2.19}$$

Using σ from (2.19), we have the fluid velocity more accurately than from performing finite difference on ϕ in space from the solution of Green's Theorem.

$$\int_S \sigma(\vec{\xi})\nabla G(\vec{x};\vec{\xi}) = \vec{\nabla}\phi = \vec{V} \tag{2.20}$$

2.5 Bernoulli's Equation

The pressure at any point in the fluid is given by Bernoulli's equation

$$p(\vec{x},t) = -\rho\left(\frac{\partial\phi}{\partial t} + \frac{1}{2}|\nabla\phi|^2 + gz\right) + p_a \tag{2.21}$$

where $\vec{x}$ is a position vector in a coordinate system fixed in space and z is the vertical coordinate, defined positive upwards. p_a is the atmospheric pressure, assumed to be a constant, and can be defined to be zero. gz is the hydrostatic pressure at a depth z. Integrating the pressure over a body in the fluid domain gives the force on the body

$$F_i = -\rho\iint_{S_B}\left(\frac{\partial\phi}{\partial t} + \frac{1}{2}|\nabla\phi|^2\right)n_i dS + \iint_{S_B} gzn_i dS \tag{2.22}$$

The second integral in (2.22) is a constant for a body whose displacement does not change, as in the cases where a body is submerged, or a surface peircing body that is restricted in heave, roll, and pitch. Since this restriction is enforced in this study, this integral is cancelled by the weight of the body and (2.22) then becomes

$$F_i = -\rho\iint_{S_B}\left(\frac{\partial\phi}{\partial t} + \frac{1}{2}|\nabla\phi|^2\right)n_i dS \tag{2.23}$$

Computing the force by equation (2.23), requires $\frac{\partial\phi}{\partial t}$ in an inertial frame. However, the quantity we can compute is the derivative in a moving frame. To obtain the derivative needed, a convective derivative of the form

$$\frac{d\phi}{dt} = \frac{\partial\phi}{\partial t} + (\nabla\cdot\vec{U}) \tag{2.24}$$

is introduced, where the second term in the righthand side is the convective derivative. We compute the force on the body by

$$F_i = -\rho\iint_{S_B}(\frac{d\phi}{dt} - (\nabla\cdot\vec{U}) + \frac{1}{2}|\nabla\phi|^2)n_i dS \tag{2.25}$$

2.6 Milne-Thomson Approach

The following approach has been established by Milne-Thomson [10] and is provided for background. Milne-Thomson gives an expression for the force on a body in terms of the kinetic energy of the fluid.

Generalized coordinates are the minimum quantities from which the configuration of a dynamical system is defined. It is possible to describe the position of any such system with n generalized coordinates, $x_1, x_2, ..., x_n$.

As we have linearized the problem through the boundary conditions imposed, the velocity potential may be rewritten as

$$\phi = u_i \phi_i \tag{2.26}$$

where u_i is a unit velocity in the i^{th} mode. Milne-Thompson stated

$$F_i = -\frac{d}{dt}\left(\frac{\partial T_L}{\partial u_i}\right) + \frac{\partial T_L}{\partial x_i} \tag{2.27}$$

where

$$T_L = \frac{1}{2} u_i u_j m_{ij} \tag{2.28}$$

is the kinetic energy of the fluid. The added mass is

$$m_{ij} = \rho \iint_{S_B} \phi_i n_j dS \tag{2.29}$$

The force on a body in the fluid may then be written as

$$F_i = -m_{ij}\dot{u}_i - u_j u_k \left(\frac{\partial m_{ij}}{\partial x_k} - \frac{1}{2}\frac{\partial m_{jk}}{\partial x_i}\right) \tag{2.30}$$

2.7 Combined Approach

Combining the above approaches (Bernoulli and Milne-Thompson) yields a method in which the force from the velocity squared term in Bernoulli, the convective correction and a time derivative of the added mass provide the total force in this dynamical system.

The time derivative of (2.29) may be rewritten, exploiting both the generalized nature of the velocity potential, here (2.26), and the definition of the added mass (2.29),

$$\rho \frac{d}{dt} \iint_{S_B} \phi n_i dS = \tag{2.31}$$

$$\rho \iint_{S_B} \frac{du_j}{dt} \phi_j n_i dS + \rho \iint_{S_B} u_j \frac{d\phi_j}{dt} n_i dS = \tag{2.32}$$

$$\dot{u}_j m_{ij} + u_j \frac{dm_{ij}}{dt} \tag{2.33}$$

It was here Wu [20] §2.3 pointed out that the time derivative could be expressed as a spatial derivative:

$$\frac{dm_{ij}}{dt} = \frac{\partial m_{ij}}{\partial x_k} \frac{dx_k}{dt} = u_k \frac{\partial m_{ij}}{\partial x_k} \tag{2.34}$$

whence, 2.25 became

$$F_i = -m_{ij}\dot{u}_j - u_j \frac{dm_{ij}}{dt} + \rho \iint_{S_B} ((U \cdot \nabla\phi) - \frac{1}{2}\nabla\phi \cdot \nabla\phi) n_i dS \tag{2.35}$$

Now that we have the complete expression for the force, we write the equations of motion for this problem:

$$m\dot{u}_i = F_i \tag{2.36}$$

written out, this becomes

$$m\dot{u}_i + \dot{u}_j m_{ij} = -u_j \frac{dm_{ij}}{dt} + \rho \iint_{S_B} ((U \cdot \nabla\phi) - \frac{1}{2}\nabla\phi \cdot \nabla\phi) n_i dS \tag{2.37}$$

Normally for a forced system, damping and restoring will be on the left hand side, and the ordinary differential equation (ODE) is solved for acceleration, velocity and position. However, velocity and position are known at each time step and can be moved to the right hand side where they become part of the forcing of the body. Considering this, our new equation of motion becomes

$$m\dot{u}_i = F_i - Bu_i - C\tilde{x}_i \tag{2.38}$$

where B is the damping matrix, C is the restoring matrix, and $\tilde{x}_i$ is the distance of the body in mode i from the equilibrium position of the system.

2.8 Complete Iterative Method

Begin the problem by acquiring body geometries, initial conditions and boundary conditions. Each time step is made up of three sub-steps; the first is the "minus" sub-step, the second is the time step, and the third is the "plus" sub-step. For the time step, the values for the Green function and its derivatives, necessary for the potential and source formulations, are calculated. The potential is solved for using either an iterative or direct method. The source strength is then computed with the same numerical method. The fluid velocity, added mass and the force from Bernoulli are then calculated. For the plus and minus sub-steps only the potential is found and then the second term in (2.35) is calculated. Finally, after all three sub-steps are completed, the force on the bodies is found from adding the force from Bernoulli and the time derivative of the added mass force from the sub-steps, solving a linear system for acceleration then used in (2.35), and the velocity and acceleration for the next time step are updated.

Chapter 3

Numerical Method

There are multiple versions of the channel code developed in conjunction with this paper. The distinguishing characteristic is how the channel is represented. The code used in [9] uses a paneled channel as well as the channel representation used in [20], which represents the channel using a rectangular channel Green function developed by Professor J.N. Newman [13]. This method uses an infinite series of reflections to create the channel boundaries. The disadvantage is that the channel is rectangular. This code is aptly named the rectangular channel code. The other code, the general channel code, uses a discretized channel as the boundary of the fluid domain. The channel is no longer restricted to having any particular shape, but it must enclose the fluid volume, except for the free surface. The disadvantage of this method is the number of panels required for a simulation increases by at least one order of magnitude, thus greatly increasing computational effort. To lessen the burden of the increased number of unknowns, acceleration techniques in the solution of the potential and source formulations are explored.

The codes also differ in the number of degrees of freedom allowed on each body. The three varieties include

- the original channel code: body 1 moves with rectilinear motion and constant velocity, and body 2 is fixed;
- the channel code detailed in [20]: incorporated the equations of motion to allow

for unrestricted motion in the horizontal plane;

- the current version of the channel code: adds heave and pitch motions to the surge, sway and yaw from above, and the option of damping and restoring the motions of each body.

The discussions in this chapter are geared toward the general channel code.

3.1 Coordinate Systems

For the channel, the global Cartesian coordinate system is chosen with the x-axis along the length, the y-axis along the width, and the z-axis positive up, with $z = 0$ at the free surface. In the rectangular channel code, the origin of the coordinate system is at the side of the channel, such that for a body to be within the channel it must have a positive y-coordinate. There is no restriction on x-coordinate since the channel in this code is infinitely long. In the general channel code, the channel may be placed anywhere below $z = 0$, but must be bounded and sealed by the $z = 0$ plane. The bodies must then lie within the discretized channel. Each discretized body has a local coordinate system, with the origin typically at the center of gravity (CG) of the body, and the positive x-axis extends toward the bow. The origin at the CG simplifies the rotational dynamics of the problem.

The solution of the equations of motion is done in the global frame coordinate system, as are the calculations for the solution of the potential and source formulations. The forces on the bodies are evaluated in the body coordinate system, thus the fluid velocities must be transformed into the body coordinate system. For the calculation of those forces, the transformation matrices are used to go from global to body,

$$\begin{bmatrix} cos\psi cos\theta & sin\theta & sin\psi cos\theta \\ -cos\psi sin\theta & cos\theta & -sin\psi sin\theta \\ -sin\psi & 0 & cos\psi \end{bmatrix} \tag{3.1}$$

and from body to global,

$$\begin{bmatrix} cos\psi cos\theta & -cos\psi sin\theta & -sin\psi \\ sin\theta & cos\theta & 0 \\ sin\psi cos\theta & -sin\psi sin\theta & cos\psi \end{bmatrix} \tag{3.2}$$

where ψ is the pitch angle and θ is the yaw angle. Roll was omitted because it is assumed balanced by the hydrostatic restoring forces.

3.2 Discrete Form of Green's Theorem

A panel method is used to solve the potential and source formulations. The surfaces associated with the boundaries of the fluid domain in these integral equations must be paneled in the general channel code, with the exception of the free surface, where the method of images is employed. The discrete form of (2.17) is

$$2\pi\phi_j - \sum_{i=1 i\neq j}^{N} \iint_{P_i} (\phi G_n) dS_{S_B \cup S_C} = \sum_{i=1}^{N} \iint_{P_i} (G\phi_n) dS_{S_B \cup S_C} \tag{3.3}$$

where P_i is the i^{th} panel on the surfaces S_B and S_C, which are discretized into N elements. Now, the following assumptions are made. Each panel is planar, and ϕ and ϕ_n are piecewise constant (i.e. the potential is constant across each panel). The result is

$$2\pi\phi_j - \sum_{i=1 i\neq j}^{N} \phi_i \iint_{P_i} G_n dS_{S_B \cup S_C} = \sum_{i=1}^{N} \phi_{n_i} \iint_{P_i} G dS_{S_B \cup S_C} \tag{3.4}$$

The integrals are evaluated by the algorithm of [12], and the linear system of rank N is solved for ϕ, either iteratively or directly. The source formulation is solved in the same manner.

To compute the discretized form of (2.25) for each mode,

$$F = -\rho \sum_{i=1}^{N} \left[\frac{\phi_{+\Delta\epsilon} - \phi_{-\Delta\epsilon}}{\Delta t} - (\nabla \cdot U) + \frac{1}{2}|\nabla\phi_i|^2 \right] A_i \hat{n}_i \tag{3.5}$$

where $\Delta\epsilon$ is the magnitude of the sub-step, Δt is the magnitude of the time step, U is the body velocity, A_i is the i^{th} panel area, $\hat{n}_i$ is the i^{th} panel normal and N is the total number of panels.

3.3 Time Stepping

The potential and source formulations are solved at each time step. However, for the time derivative of the added mass in (2.35), Wu [20] employed a "possible displacement" two-sided difference scheme. This method involved sub-steps, at which only the potential formulation was solved. The idea behind these sub-steps is that the two-sided difference scheme offers equivalent accuracy with less computational effort, in that a larger time step can be used than for one-sided finite difference. For each instant in time (i.e. each time step), the bodies are "displaced" forward and backward in space and their positions are calculated with constant velocity. In reality, these positions are never achieved.

The following derivation is taken from [20]. Knowing the velocities and accelerations, the displacement of each body may be calculated:

$$D_i^t = P_{o,i}^{t+\Delta t} - P_{o,i}^t = u_i^t \Delta t + \frac{1}{2}\dot{u}_i^t (\Delta t)^2 \tag{3.6}$$

where D is the displacement of the body, t is the number of the time step, Δt is the magnitude of the time step, P^t is the position vector for the t^{th} time step, o^{th} sub-step, and i^{th} mode. The velocity at the new time step is

$$u^{t+\Delta t} = u^t + \dot{u}^t \Delta t \tag{3.7}$$

The positions of the bodies between the sub-steps $(-,+)$ and the time step (o) are

$$P_+^t - P_o^t = u^t \Delta\epsilon \tag{3.8}$$

and

$$P_-^t - P_o^t = -u^t \Delta\epsilon \tag{3.9}$$

where $\Delta\epsilon$ is the magnitude of the sub-step. Note that the time step and the sub-step indicated by o are the same. Using (3.6)

$$P_-^{t+\Delta t} - P_+^t = \tag{3.10}$$

$$(P_-^{t+\Delta t} - P_o^{t+\Delta t}) + (P_o^{t+\Delta t} - P_o^t) + (P_o^t - P_+^t) = \tag{3.11}$$

$$-u^{t+\Delta t}\Delta\epsilon + u^t\Delta t + \frac{1}{2}\dot{u}^t(\Delta t)^2 - u^t\Delta\epsilon \tag{3.12}$$

Combining (3.10) and (3.7) to eliminate the u^t term and like terms, we find

$$P_-^{t+\Delta t} - P_+^t = u^{t+\Delta t}(\Delta t - 2\Delta\epsilon) - \frac{1}{2}\dot{u}^t\Delta t(\Delta t - 2\Delta\epsilon) \tag{3.13}$$

and we can see that if the magnitude of the sub-step is set equal to half of the magnitude of the time step, then the P_+^t and $P_-^{t+\Delta t}$ positions are the same. This means that the potential formulation for P_+^t can be reused for $P_-^{t+\Delta t}$, thus reducing the number of potential calculations from $3n+1$ to $2n+1$, where n is the number of time steps. However, this detail has not been implemented in the code because the restriction of $\Delta\epsilon = \frac{1}{2}\Delta t$ is not imposed.

3.4 Non-Dimensionalization

The added mass, forces and moments output from the code are nondimensionalized with respect to the initial body velocity, U, the first body's length, L, and the density of water, ρ. For added mass,

$$m_{ij} = \frac{\tilde{m}_{ij}}{\rho L^k} \tag{3.14}$$

where $k = 3$ for the pure translational modes $(i, j = (1,2,3) + 6(n-1)$, $k = 5$ for the pure rotational modes $(j = (4,5,6) + 6(n-1))$, and $k = 4$ for the coupled translational/rotational modes. For forces and moments,

$$F_i = \frac{\tilde{F}_i}{\frac{1}{2}\rho U^2 L^m} \tag{3.15}$$

where $m = 2$ for $i = (1,2,3) + 6(n-1)$ for forces, $m = 4$ for $i = (4,5,6) + 6(n-1)$ for moments and $m = 3$ for the coupled terms; n is the number of the body. The nondimensionalized quantity is indicated by the "~".

3.5 Collision Check

A crude collision check was implemented and used mainly for the disparate body study. The method involved checking if the larger body panels were within the block of the smaller body. This is most effective for full bodies and when the smaller body is much smaller than the larger body (i.e the ratio of the lengths is .1). The other method explored was giving the small body a characteristic radius, transforming the larger body into the coordinate system of the smaller body, and since the smaller body was centered at the origin, checking if the distance of any of the points on the larger body were less than the characteristic radius from the origin. This method is best for bodies with length-to-beam and beam-to-draft ratios near 1. If there were a collision, the time step is noted in a file, the simulation can be animated, and the conditions leading up to the collision could be identified. A more robust collision check could utilize the value of potential for each field/source point pair.

Chapter 4

Verification

This chapter discusses the tests necessary to verify that the code produces accurate results. The first section, 4.1, discusses the convergence studies performed to verify the geomertries used for later verifications and scenarios are properly and suitably discretized. In addition, the convergence tests confirm the methods in the code converge to a single result, in the limit that the number of panels on the bodies becomes infinite (thus representing the body exactly). Section 4.2 confirms that the result the code converged to in 4.1 is the correct result, comparing to both older versions of this code which were validated to published results, and to a published result from a strip theory code [21].

In the following chapters, "body 1" refers to the body with an initial velocity (in surge, for all cases in this paper); "body 2" refers to the body with zero initial velocity and in §6.2, the moored body. For accurate and converged results, it is necessary to have at least two characteristic panel dimensions (CPD) distance between the surfaces of any two bodies, including the channel, (using the larger value of the CPD of the two bodies in question) at any time during a simulation, as evidenced in Figure 5-10. In a paper by Zhao and Faltinsen [22], it is shown that the reason for this requirement in low order panel methods is due to the discontinuity of the potential and the source strength across constant strength low order panels.

4.1 Convergence

This section explores the convergence of the code in time (4.1.1), for the discretization of the bodies (4.1.2) and the channel (4.1.3), and in the limit that the channel becomes infinitely large and far away from the bodies(4.1.4). In the limit that the time step goes to zero, that the number of panels goes to infinity, and that the channel is infinitely far away, the results of the forces and moments on the bodies should converge to one set of values. Figures 4-1 to 4-11 will be discussed. Table 4.1 shows specifications of the bodies used in the verification study. The spheroids were generated using a typical low order panel spheroid generator and discretized so as to keep panel aspect ratios close to 1. The channels were discretized using a rectangular channel low order panel generator.

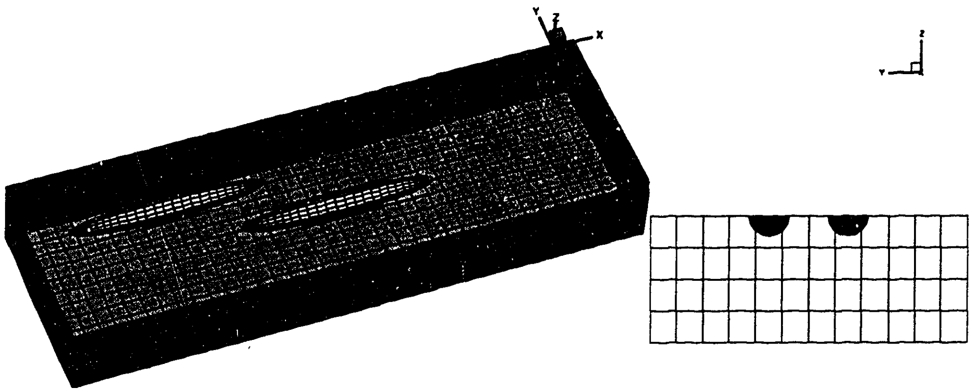

Figure 4-1: Sample geometry for convergence tests and verification with previous versions of channel code, shown with the 256 panel spheroid with square panels and the 816 panel channel.

4.1.1 Time

For time convergence shown in Figures 4-2 and 4-3, Δt of .05 (the gradient symbol), .1 (the square), and .2125 (the circle) are used. The spheroid $\mathcal{A}$ is used for body 1 and body 2 with the channel ($\mathcal{A}$). Body 1 is positioned at $(x, y, z, \psi, \theta) = (-.8, .124, 0, 0, 0)$ with an initial unit velocity in surge and body 2 is at $(0, -.124, 0, 0, 180)$ with no initial velocity, where ψ is the pitch angle and θ is the yaw angle.

Body	Total panels	Length (# of panels)	Width(panels in Girth)	Draft	Largest CPD	Panel Aspect Ratio
Half Spheroid $\mathcal{A}$	256	1(16)	.125(16)	.125	.0625	5.1
Half Spheroid $\mathcal{B}$	256	1(32)	.125(8)	.125	.03125	1.28
Half Spheroid $\mathcal{C}$	480	1(40)	.125(12)	.125	.025	1.53
Half Spheroid $\mathcal{D}$	576	1(24)	.125(24)	.125	.04167	5.1
Half Spheroid $\mathcal{E}$	960	1(60)	.125(16)	.125	.01667	1.36
VLCC	280	1(20)	.1667(7)	.05	.05	3
Spheroid $\mathcal{F}$	576	1(32)	.125(16)	.125	.03125	1.28
Spheroid $\mathcal{G}$	576	.625(32)	.078(16)	.078	.01953	1.28
Channel $\mathcal{A}$	816	3(36)	1(12)	.4(4)	.08333	1
Channel $\mathcal{B}$	1836	3(54)	1(18)	.4(6)	.05555	1
Channel $\mathcal{C}$	3264	3(72)	1(24)	.4(8)	.04166	1
Channel $\mathcal{D}$	1536	6(72)	1(12)	.4(4)	.08333	1
Channel $\mathcal{E}$	3456	6(108)	1(18)	.4(6)	.05555	1
Channel $\mathcal{F}$	816	30(36)	10(12)	4.(4)	.8333	1
Channel $\mathcal{G}$	816	300(36)	100(12)	40(4)	8.333	1
Channel $\mathcal{H}$	1944	3(36)	1.5(18)	1(12)	.08333	1
Channel $\mathcal{J}$	2160	3(36)	1(12)	1.5(18)	.08333	1
Channel $\mathcal{K}$	4068	2,4(54,108)	1,2(18,36)	.15(4)	.05555	1.5
Channel $\mathcal{L}$	4068	2,4(54,108)	1,2(18,36)	.25(4)	.05555	1.5
Channel $\mathcal{M}$	4068	2,4(54,108)	1,2(18,36)	.45(4)	.05555	1.5

Table 4.1: Body specifications for verification studies

Figure 4-2 shows convergence for the forces on body 1. The surge force on body 1 is converged for each size of the time step. Sway force results converge well as the time step is halved each time. Similar convergence is seen for the yaw moment. A time step of .1 is adequate to convey trends in the force curves. However, for more accurate body forces and motions, a finer time step is recommended.

Figure 4-3 shows all forces and moments on body 2 are at their converged values, to graphical accuracy. These results imply that if you are interested in the forces on a body moving very slowly relative to the other body, a coarse time step is acceptable, but for accurate forces on a body moving with a velocity within an order of the other body, a finer time step is necessary.

Note the peak of the forces for body 1 at either end of the plot is due to the interaction with the channel end. This result will be shown in the Channel Discretization section.

4.1.2 Body Discretization

Bodies $\mathcal{A}$, $\mathcal{B}$, $\mathcal{C}$ and $\mathcal{D}$ are used, and represented in the plots with a square, diamond, circle, and gradient respectively. Channel $\mathcal{A}$ is used. The initial positions and velocities are detailed in the section above. Forces and moments on the bodies are shown in Figures 4-4 and 4-5. Results are converged to graphical accuracy for each of the spheroid panelizations except for the one with high aspect ratio panels. The 256 panel discretization is an adequate for converged results.

4.1.3 Channel Discretization

Three chanel discretizations are used with two $\mathcal{A}$ spheroids at initial conditions detailed above: $\mathcal{A}$ (square), $\mathcal{B}$ (circle) and $\mathcal{C}$ (gradient). The solid line is the rectangular channel code result for the same bodies and positions. The 816 panel channel ($\mathcal{A}$) is enough to yield converged results. Note in Figures 4-6 and 4-7 the 1836 panel channel does not yield significantly better results. Also of note is the necessity of significant

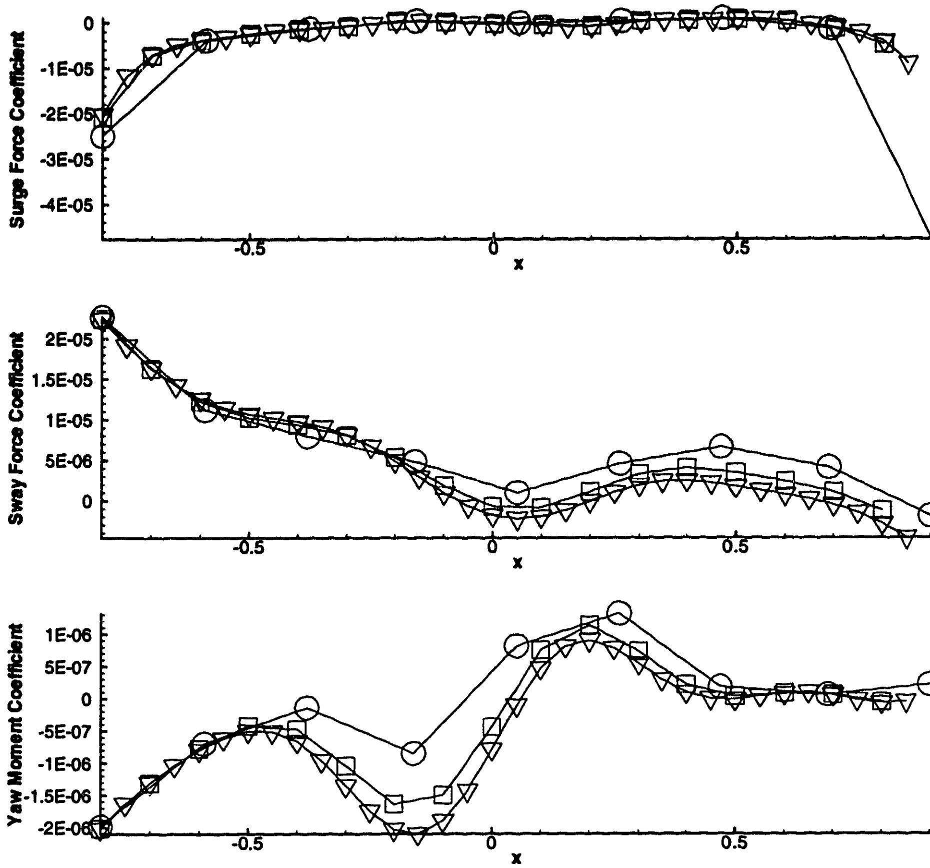

Figure 4-2: Time step convergence test with the forces on body 1.

distance between the end of a body and the channel ends, seen in Figures 4-8 and 4-9. It is approximately five times the diameter, regardless of how the channel end is discretized.

For Figures 4-8 and 4-9, the dashed line is the rectangular channel code with a channel depth of .4 and a width of 1; the solid line is the rectangular channel code with a channel of infinite width and depth. The square symbol represents the general channel code using channel $\mathcal{A}$; the circle and gradient symbols represent channels $\mathcal{D}$ and $\mathcal{E}$.

4.1.4 Semi-Infinite Fluid

This study was performed as a "reality-check". In the limit that the dimensions (length, depth and width) of the paneled channel go to infinity, we expect to converge

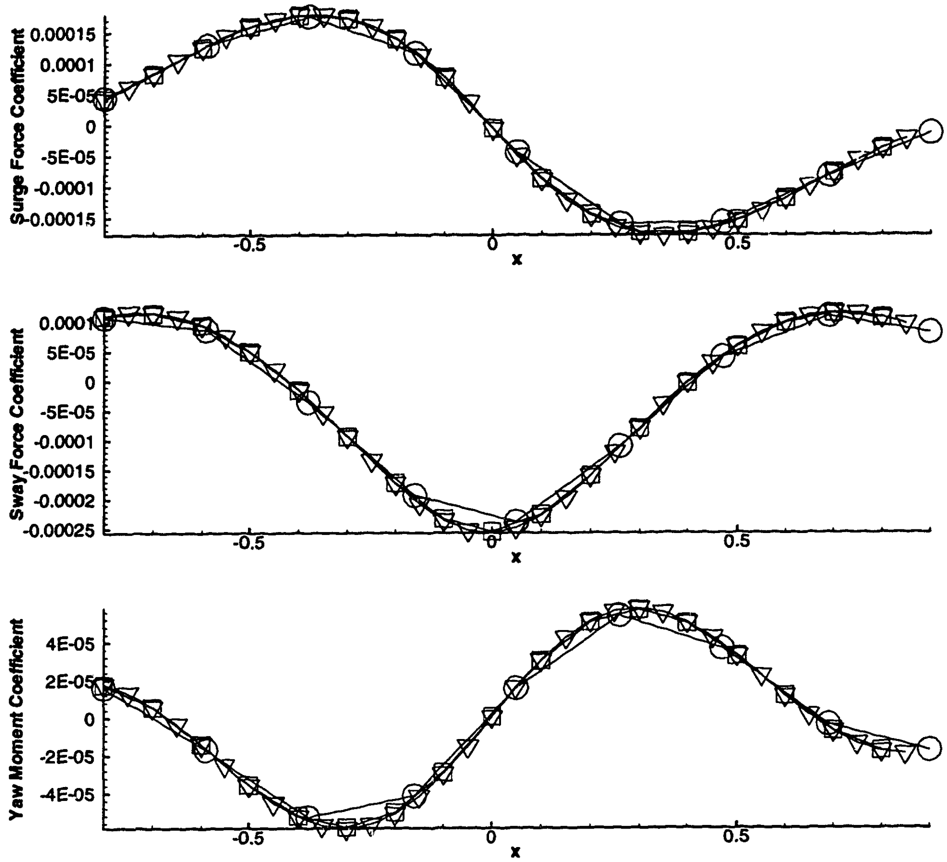

Figure 4-3: Time step convergence with the forces on body 1.

to the infinite fluid result from the rectangular channel code. The channels used were 1x($\mathcal{A}$), or 1 times the default channel dimensions, 10x($\mathcal{F}$) and 100x($\mathcal{G}$), and for the rectangular channel, 1x and ∞, corresponding to the symbols square, circle, gradient, dotted line and solid line in the plot, respectively. The $\mathcal{A}$ spheroid was used. At 1x, the bodies have a clearance from the wall of .3135 body lengths; at 10x, this clearance has grown to 4.8135 body lengths. As the channel walls go to infinity, and their influence diminishes to zero, the rectangular channel code and the general channel codes should converge to the same results. Figures 4-10 and 4-11 show the results as expected and that at 10x, the channel can be considered to be at infinity. For sway in Figure 4-10, the 1x general channel result is not "on" the 1x rectangular channel results because the channel is not long enough (see Figure 4-8), and is not due to

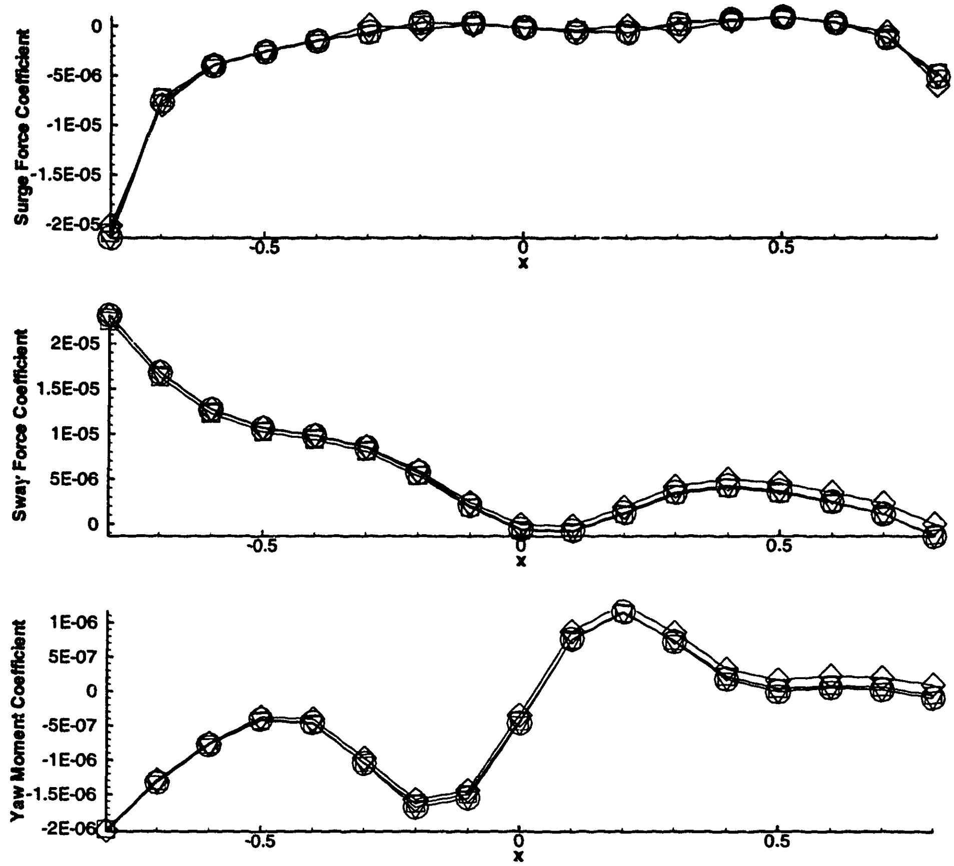

Figure 4-4: Discretization convergence test with the forces for body 1.

panelization (see Figure 4-6).

4.2 Verification

4.2.1 Previous Channel Codes

The current version of the code was able to reproduce results from the original general channel code, for a geometry similar to Figure 3 in [9], as well as the original rectangular channel code and the rectangular channel code with horizontal motions. Recall, the original general channel and rectangular channel codes restrict body 1 to motion with constant velocity in surge and body 2 fixed.

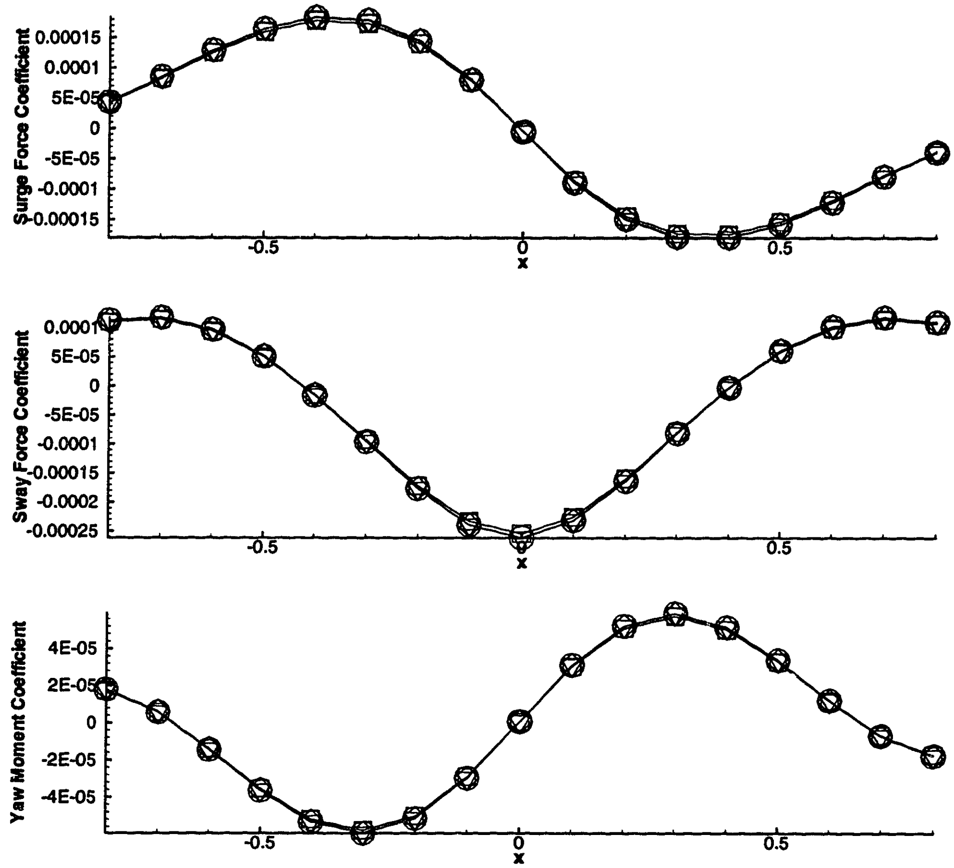

Figure 4-5: Discretization convergence test with the forces for body 2.

4.2.2 General Channel Code with Vertical Motions

This verification involved two cases using the same geometry, but one is rotated 90^o of the other about the x-axis; see Figure 4-12. Force and moments from the top geometry (channel $\mathcal{H}$) are represented with the squares and those from the bottom geometry (channel $\mathcal{J}$) are represented with circles in the following plots. Body 1 is positioned at $(-1.6, .5, -.5, 0, 0)$ and $(-1.6, 0, -.5, 0, 0)$ and has an positive initial unit velocity in surge. Body 2 is positioned at $(0, -.5, -.5, 0, 180)$ and $(0, 0, -1, 0, 180)$ with no initial velocity.

To understand the results, we must first resolve how the forces on each body for the two geometries should relate. From [9] we know that as two bodies approach each other, there is a repulsion in surge and sway and the bodies yaw their closest ends

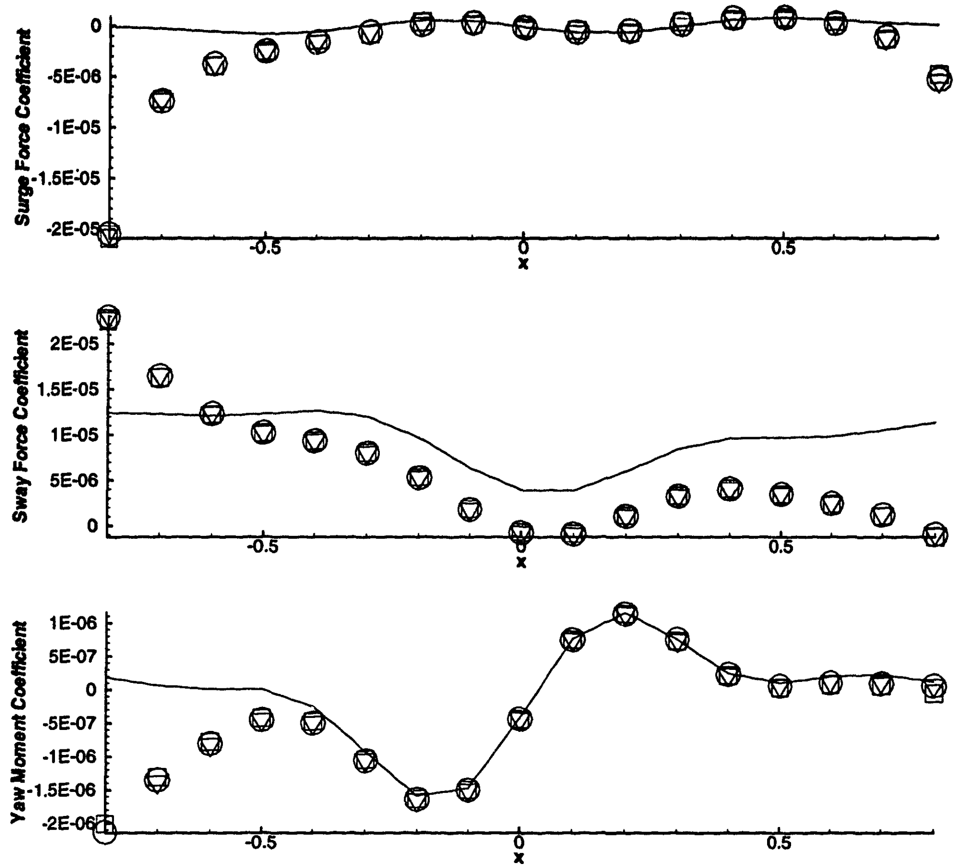

Figure 4-6: Channel discretization convergence test with forces on body 1.

toward each other (i.e. in a bow-bow meeting, the bows will attract). For body 1 (Figure 4-13), surge in channel $\mathcal{H}$ should equal surge in channel $\mathcal{J}$, sway equals heave and yaw equals negative pitch. For body 2 (Figure 4-14), surge for channel $\mathcal{H}$ equals surge for channel $\mathcal{J}$, sway equals negative heave, and yaw equals pitch. The results in Figures 4-13 and 4-14 confirm these expectations, except for sway/heave for body 1, where the results appear to be flipped in time and in sign. This was not resolved, and it appears to be an artifact of this scenario. For other scenarios, these modes compare well to published results, other scenario results, and expectations.

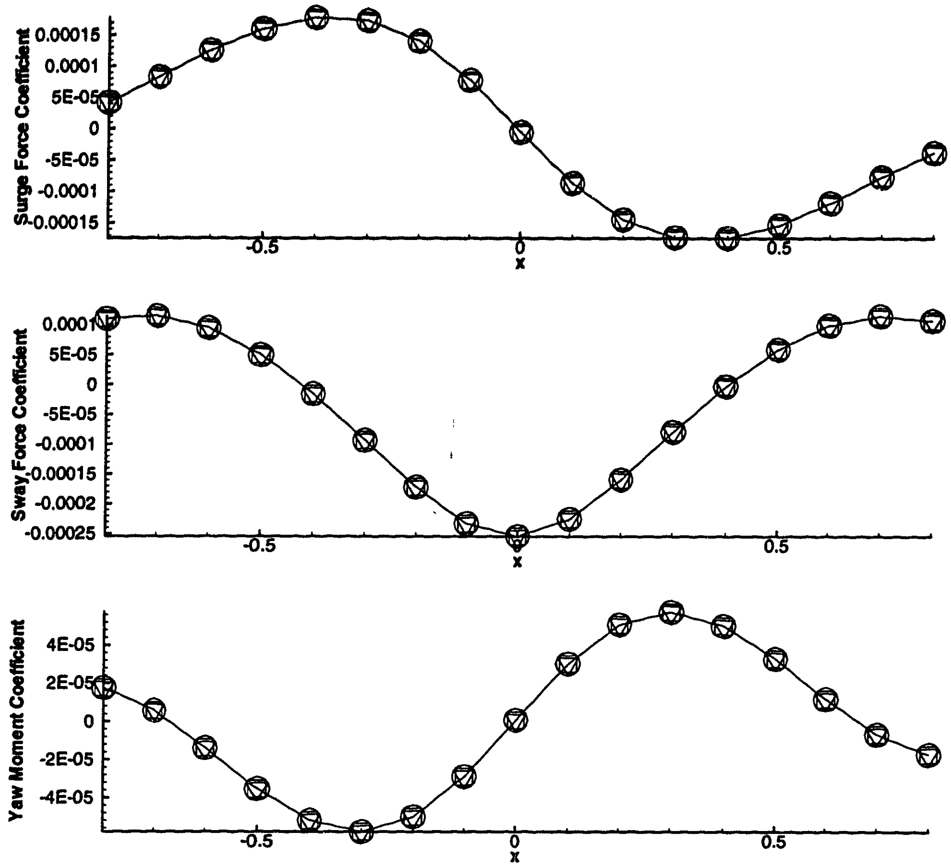

Figure 4-7: Channel discretization convergence test with forces on body 2.

4.2.3 Comparison with Strip Theory with Arbitrary Channel Wall Contour

Yeung and Tan [21] use strip theory to calculate the sway force and yaw moment on a body and conformal mapping to model boundaries in the fluid for a tanker traveling past a wall and pier with internal angles ranging from zero to 180 and for varying keel-clearance-to-draft (KCD) ratios. We are able to model each of these cases, however the first two are easier. The first case is like one body moving in a channel parallel to a wall, and can be reproduced by all previous versions of the code. The second scenario of the ship past a pier, is only able to be modeled using the general channel code, hence the latter is the case explored here. The intent is to reproduce their trends in forces and moments as a ship passes a right-angle pier using a numerical

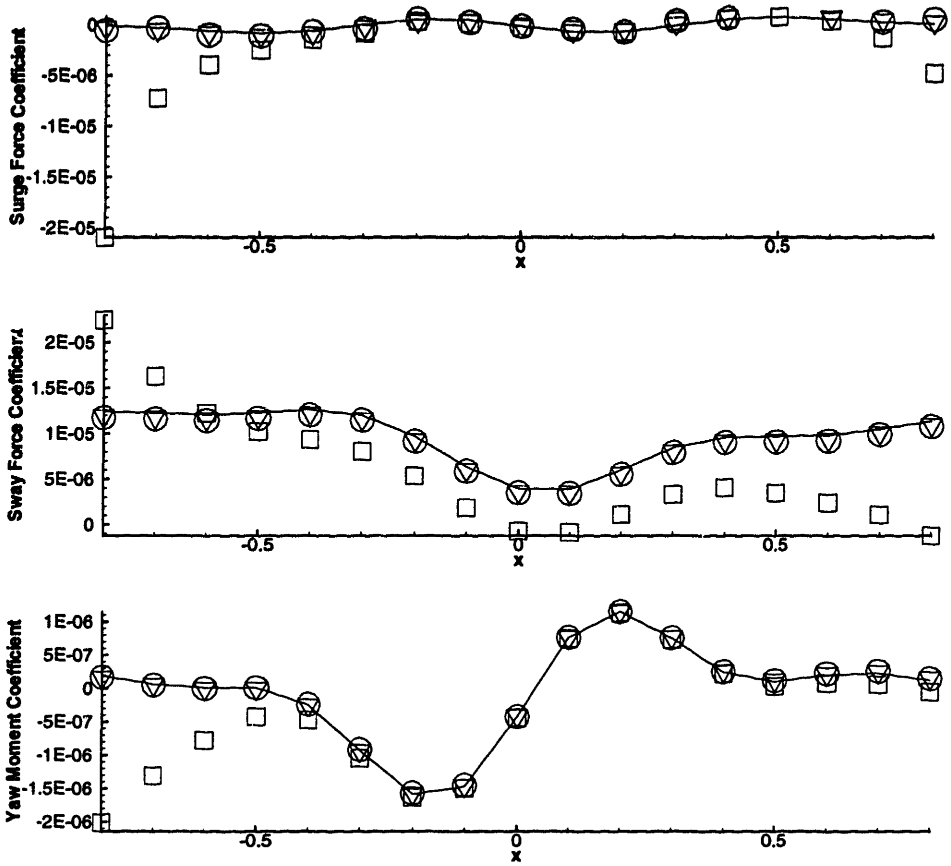

Figure 4-8: Channel length convergence test with forces on body 1.

method different from the one they used (strip theory vs. 3-D panel methods).

The VLCC used in this test was discretized from hull offsets for a real VLCC and is assumed similar to the hull form Yeung and Tan used for their ship. The channel has a geometry similar to the geometry presented in the Yeung and Tan paper, and the ship has the same offset from the pier (one-half ship length from ship centerline to pier), though the criteria of keel clearance and distances from channel boundaries other than the pier had to be compromised. The channels were generated using the same channel generator used for the channels in the previous verification tests. The KCD ratios explored in their paper are 0, .025, .05, and .1. Due to a limit in the number of unknowns for the $O(N^2)$ method used in the general channel code, KCD ratios of .667, .8 and .889 were used in this study. As a result, the distance to the pier

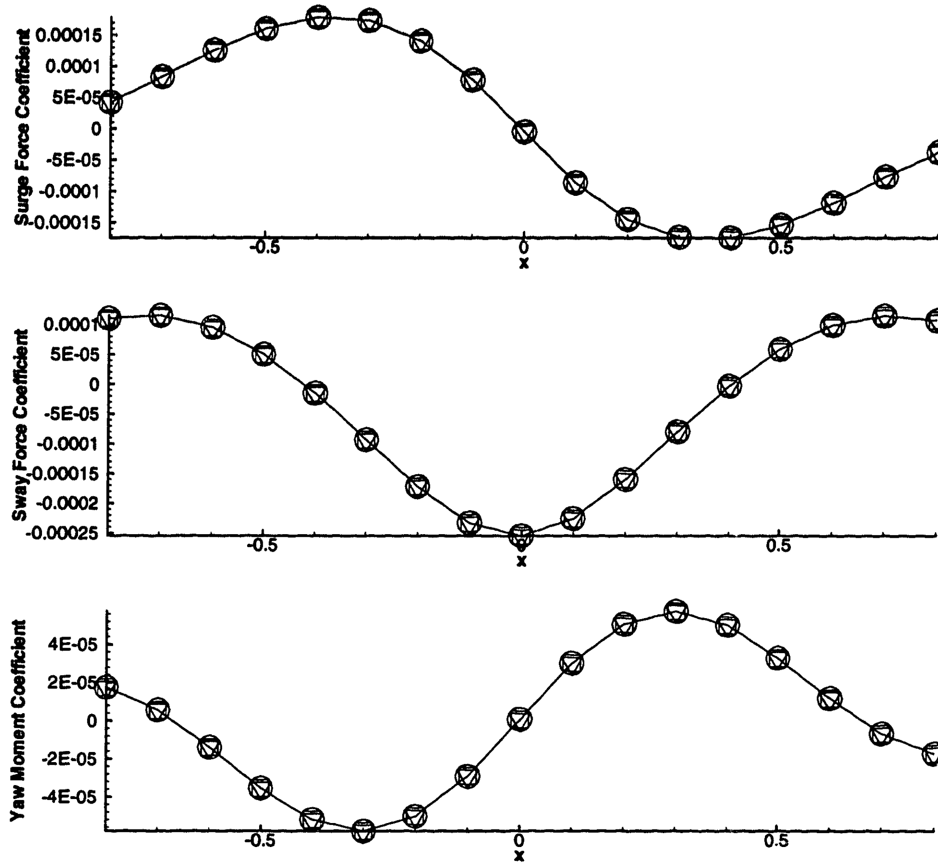

Figure 4-9: Channel length convergence test with forces on body 2.

is much larger than the draft in [21], and the opposite is the case in this study. This was unavoidable due to the computational limitations incurred by the large number of unknowns required for the discretized channel boundary.

In all figures except Figure 4-16, a wall is equidistant across the channel from the ship as the pier. This will contribute to the variation of the magnitude of the forces on the ship from the results in [21]. However, the force and moment trends should be the same. For Figure 4-16, the ship has a clearance of .216 ship lengths from the pier and .616 from the opposite wall. In Figure 4-18, the ship used has been rotated 180° for the case of leaving the pier. This will affect the sign of the sway force compared to the results in the Yeung and Tan study [21].

The figures we are comparing against are 4,5 and 9 from [21]. Figure 4 shows the

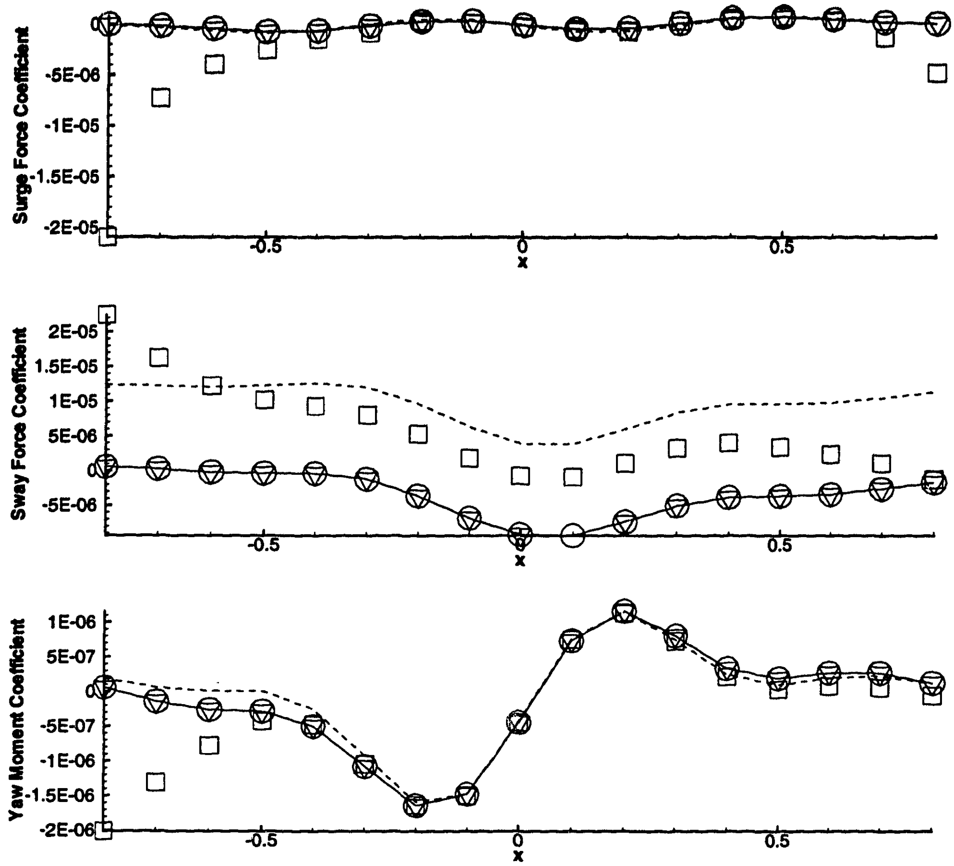

Figure 4-10: Infinite channel convergence test with forces on body 1.

change in sway force and yaw moment for a ship passing a pier with different internal angles. We are most interested in the internal angle equal to 90°, or a right-angle pier. For this case, Figure 4-16 provides the best comparison. Surge is not shown in the paper, sway follows the trend in the paper of an initial attraction followed by a strong repulsion as the bow passes the tip of the pier returning to attraction as the stern passes the tip. However, the final attraction force in [21] is greater than the attraction prior to passing the pier, and here it is not. This may be due to the wall opposite the pier. The yaw force on the ship in the paper shows a peak bow-in moment at -.6 changing to a peak bow out at .5 then decaying to a positive non zero moment. Comparatively, the results here show a slight bow-in at -.8, a peak bow-out (positive yaw moment) at -.4, and a peak bow in at .1 decaying to a constant negative

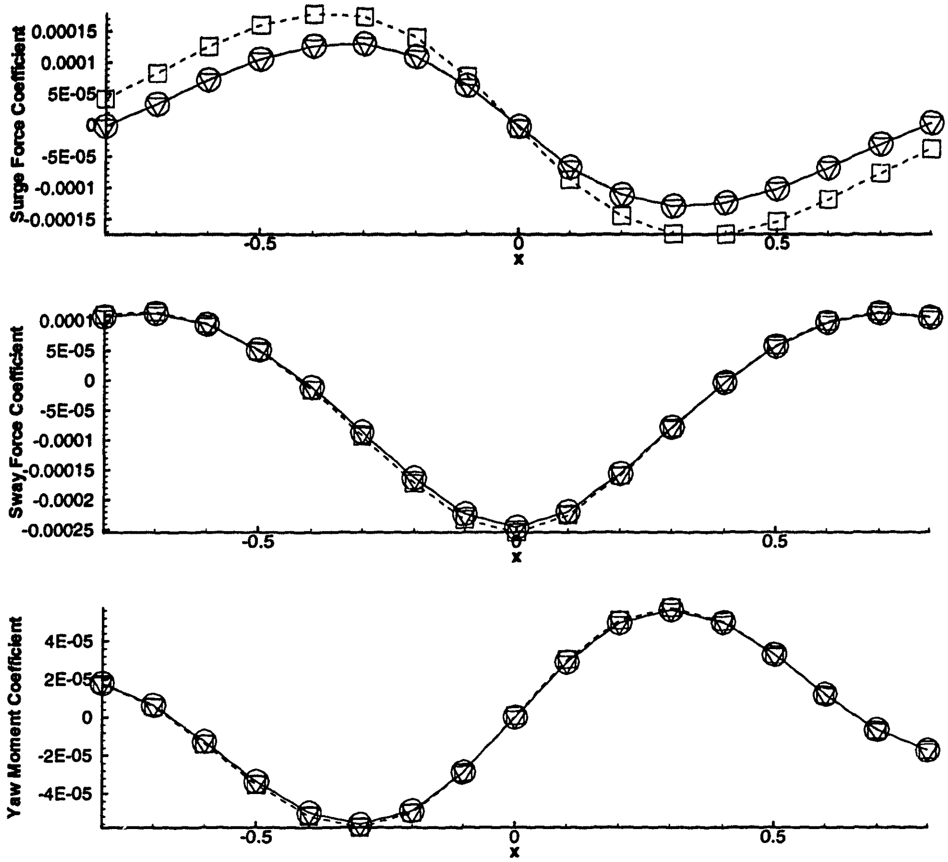

Figure 4-11: Infinite channel convergence test with forces on body 2.

moment. Again, the effects of the wall opposite the pier are suspect in reducing the initial bow-in moment, since this trend is not present in their results. However, it appears that in the limit that the discretized boundaries allow keel clearances and clearances from channel boundaries to duplicate the geometry detailed in [21], the forces on the body found using this panel method will converge to the results found using strip theory. Figure 4-16 does support this, in that, the squares represent a run for a ship equidistant from a pier and a wall parallel to the pier, and the diamonds represent a run for which the ship is closer to the pier than the wall, so, in the limit that the effect of the wall disappears, the forces should approach the Yeung and Tan results.

Figure 5 [21] shows the effect of the KCD ratio on the magnitudes of the forces

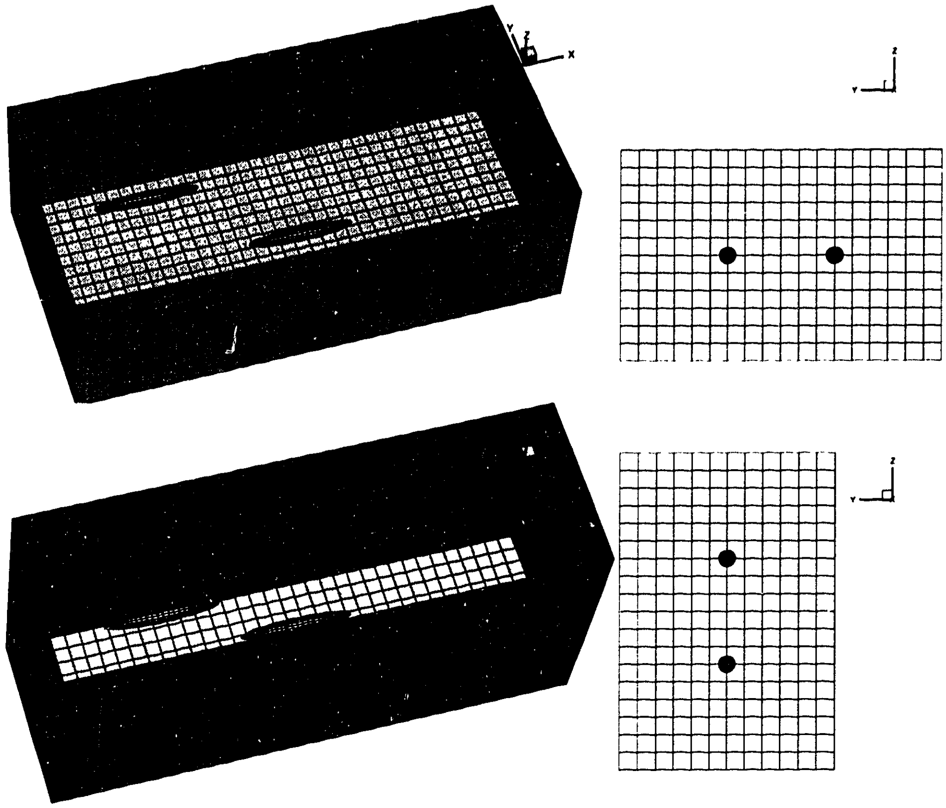

Figure 4-12: Geometries for vertical motions test.

and moments. Likewise, Figure 4-17 shows a similar trend, that as the KCD ratio decreases, the magnitude of the forces increases.

Figure 9 [21] shows the sway force and yaw moment on the ship as it approaches and leaves the pier. For sway, both approaching and leaving the pier, there is a strong attraction to the pier as the ship first encounters the pier, followed by a strong repulsion, dipping to a light attraction before leveling off. There is a constant attraction as the ship passes along the wall of the pier. For yaw, the ship approaching the pier experiences a peak negative yaw moment just before the bow reaches the pier, when the moment changes to a positive peak by the time the stern reaches the point of the pier. This curve is similar to the first half of the yaw plot in Figure 2 in the original channel paper by Korsmeyer, et. al [9]. Similarly, the yaw plot for the leaving ship is like the second half of Figure 2 in [9]. If we take this approach looking at the moment plots, we see that the results from both papers match well. In Figure 4-18,

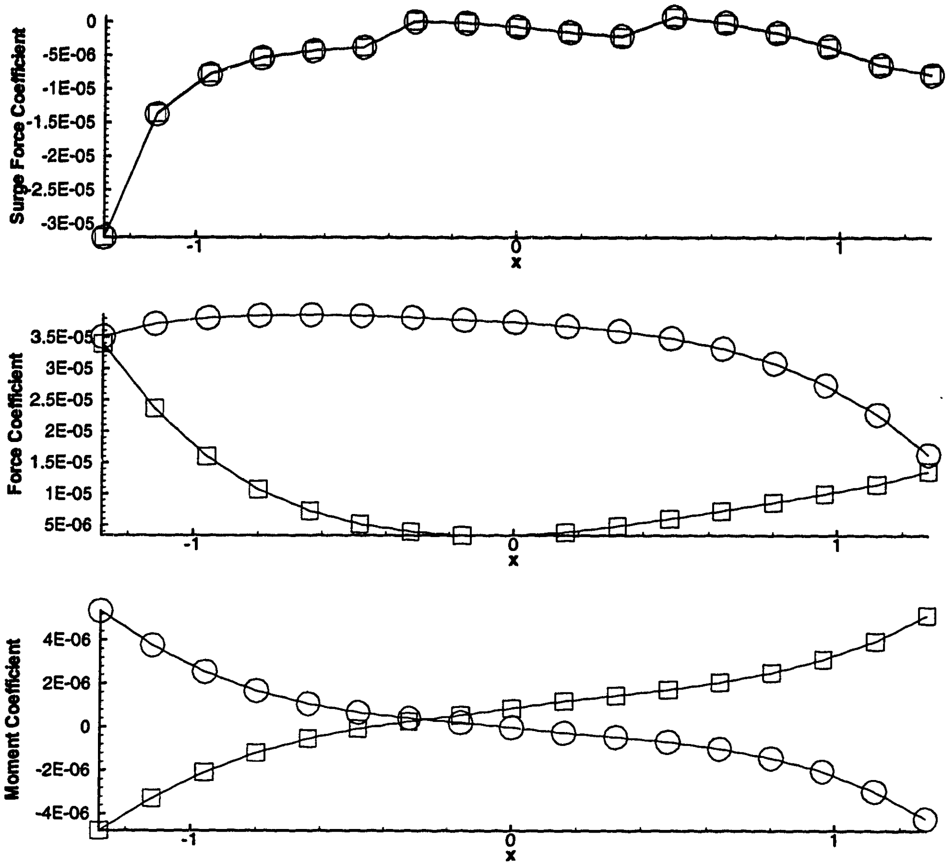

Figure 4-13: Forces on body 1 for vertical motions verification case.

the surge force trend is what we have come to expect (as seen in [9]); the trend of the sway force for the ship approaching the pier is similar to Figure 9 in [21] for the force peak experienced near the edge of the pier, however, the attraction experienced as the bow passes the edge of the pier is not present in the results shown here. It is reasonable to assume this is due to the ratio of the distance of the ship from the pier to the distance to the opposite wall. As the distance to the pier decreases, the sway attraction is apparent (Figure 4-16). As for yaw, a similar explanation would suffice for the approaching case, though the bow-in peak as the center of the ship passes the tip of the pier is not expected. The yaw moment for the ship leaving the pier correlates well with the Yeung and Tan results [21](Figure 9b).

The sample case detailed above was run but the body was not restricted to rec-

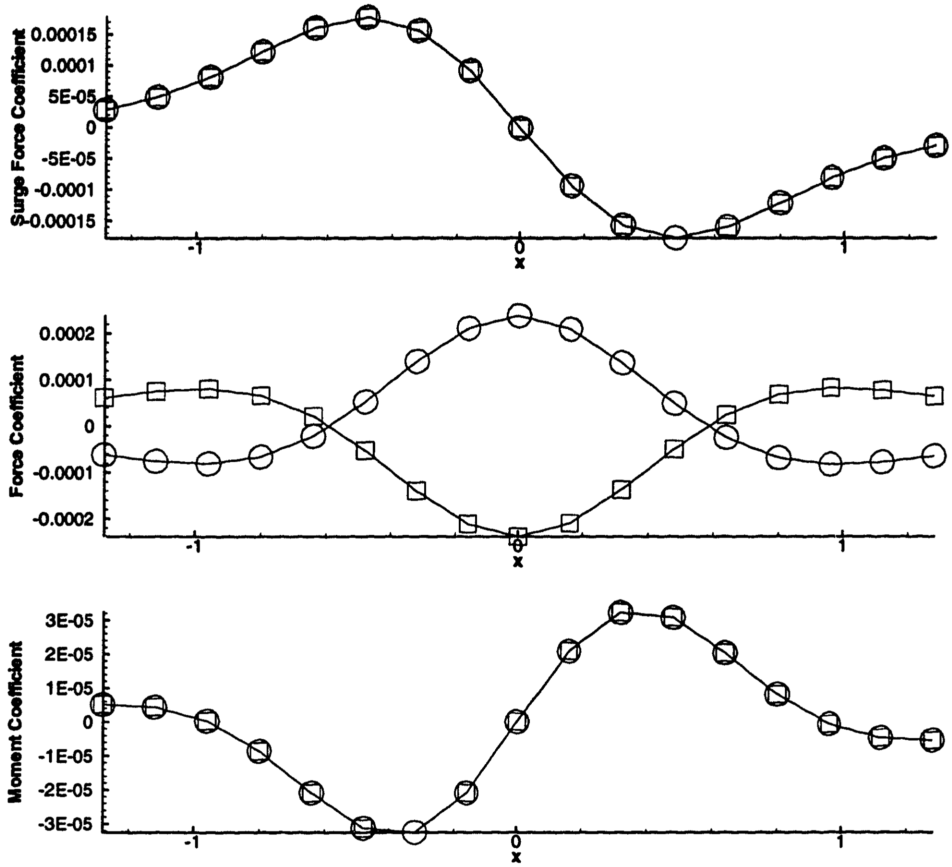

Figure 4-14: Forces on body 2 for vertical motions verification case.

tilinear motion. Here, the magnitude of the forces decreased by half. Figure 4-18 shows the force on the ship for each water depth. Figure 4-19 shows the magnitude of the forces with and without body motions. The trend of the forces with body motions being approximately half that of the forces without body motions (restricted to rectilinear) is consistent with what has been found in comparisons of the original rectangular channel code and the rectangular code with body motions.

Until very small keel clearances can be modeled with this code, it is difficult to say how well this code compares with the strip theory in [21]. This is because both the strip theory code and this panel method code show the influence of keel clearance and distance from the pier on the magnitude and trend of the forces and moments. The yaw plot in Figure 4-16 shows that halving of the pier clearance begins to show a negative yaw moment prior to the positive yaw moment as the ship approaches the pier, and in addition, a strong bow-in moment after the middle of the ship passes the tip of the pier, not seen in the strip theory results. It is also not apparent in ship/ship interaction results due to the lack of long parallel middlebody, i.e. most ship/ship interaction studies have ships of similar size. However, this is similar to ship/whale interactions, where the whale experiences the sudden appearance of the parallel middlebody of an SL7, which, to the whale, appears to be a long wall. The first numerical ship/whale study sponsored by the National Marine Fisheries Service [6] used the original rectangular channel code to model a ship moving with constant velocity passing a fixed whale. This case is similar to the present study due to the disparate dimensions of the objects (previously the whale and ship, here the ship and pier). Since the ship in the current study is moving with rectilinear motion, we should expect to see similar moment trends. In fact, the moment trends in [6] Figure 25, do compare well with the current case. An initial negative yaw moment is followed by a strong positive moment which goes negative strongly negative again as the whale travels along the middle body. If the ship passing the whale were very long, we could expect to see the yaw taper to a constant negative value just as the yaw results do in 4-16.

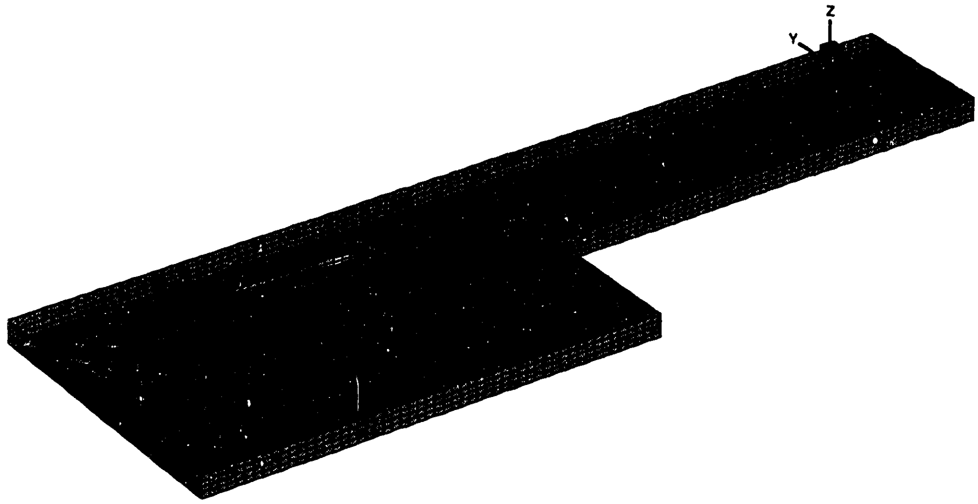

Figure 4-15: Geometry for comparison with Yeung and Tan experiments. The keel clearance to depth ratio for geometry shown is .667 with a wall clearance of .416 ship lengths

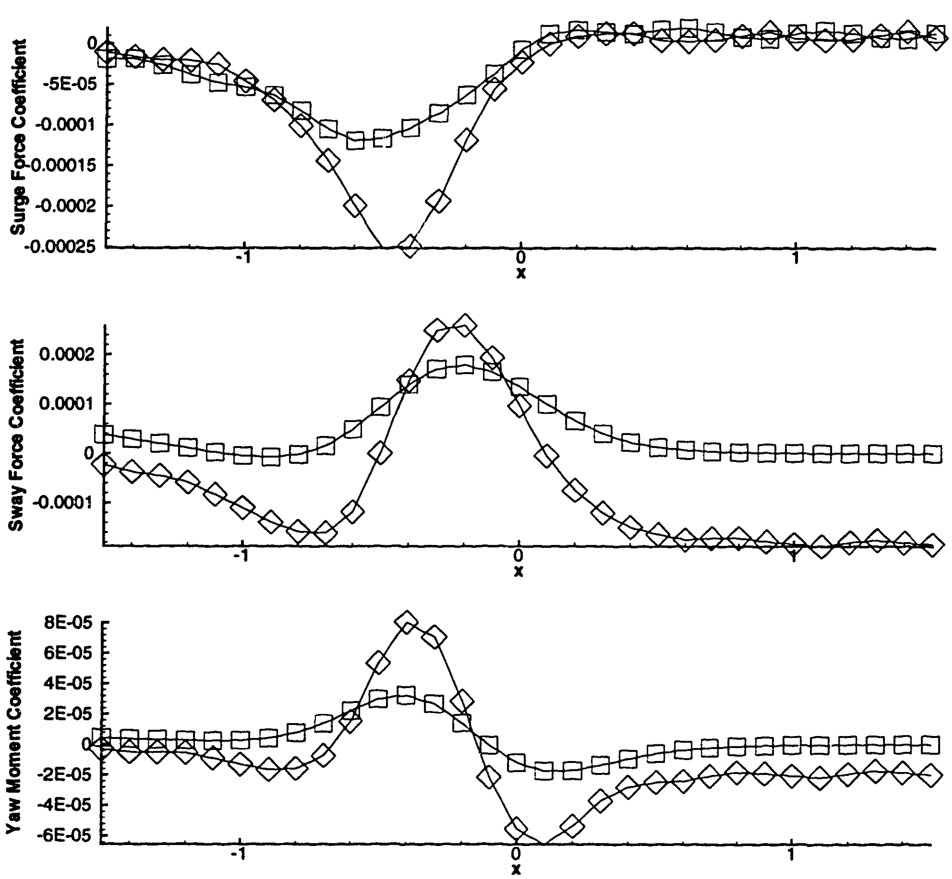

Figure 4-16: Comparison of forces on a VLCC past a right-angle pier for a horizontal clearance of .216 (diamond) and .416 (square) ship lengths.

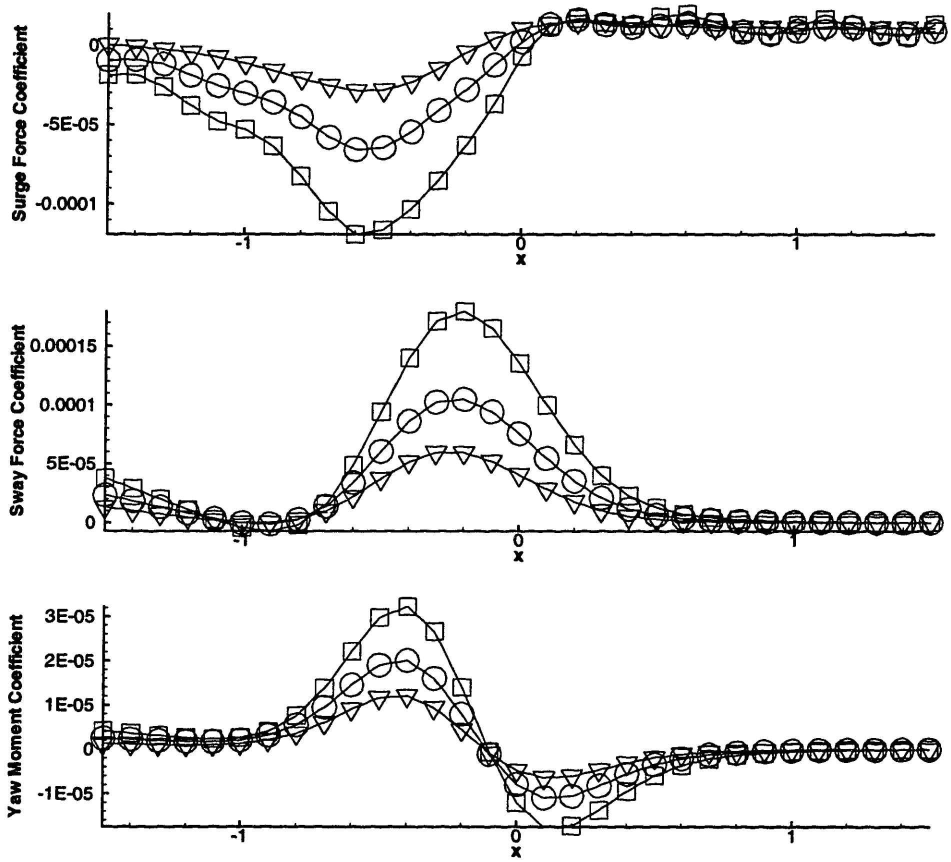

Figure 4-17: Forces on a VLCC in a channel with a right-angle pier, as in the Yeung and Tan paper, Figures 4 and 5. Data for three bottom depths is shown.

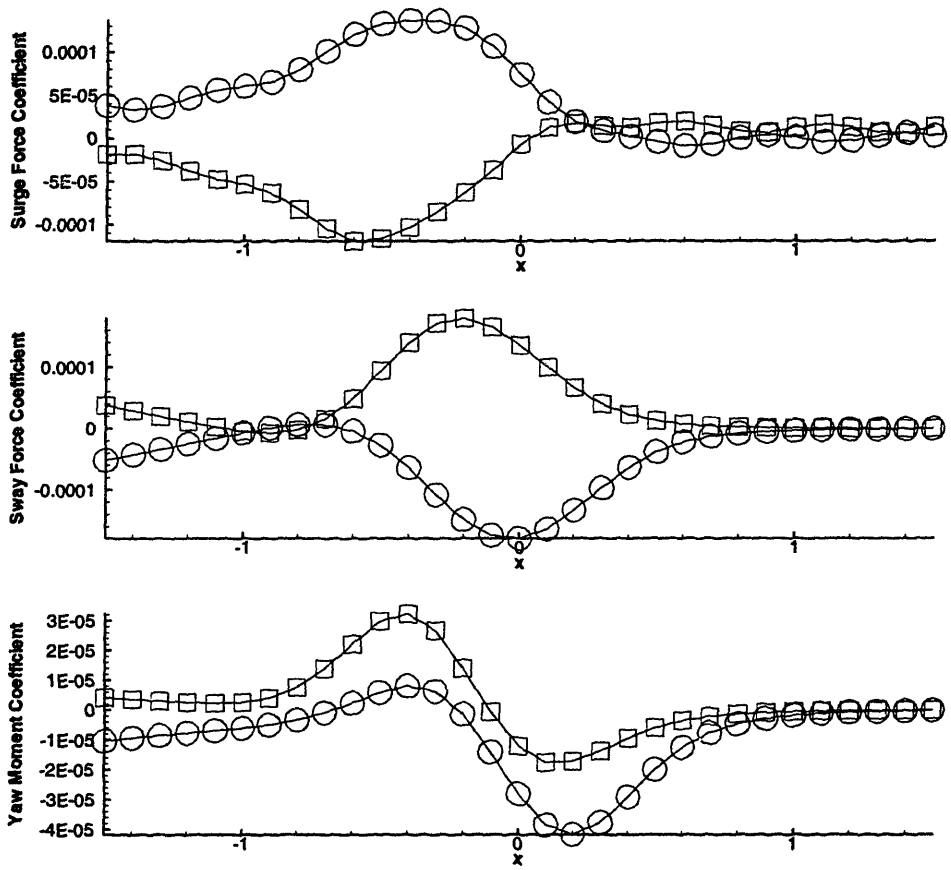

Figure 4-18: Forces on a VLCC in a channel with a right-angle pier, as in the Yeung and Tan paper, Figure 9. Data for approaching (squares) and leaving (circles) the wharf is shown.

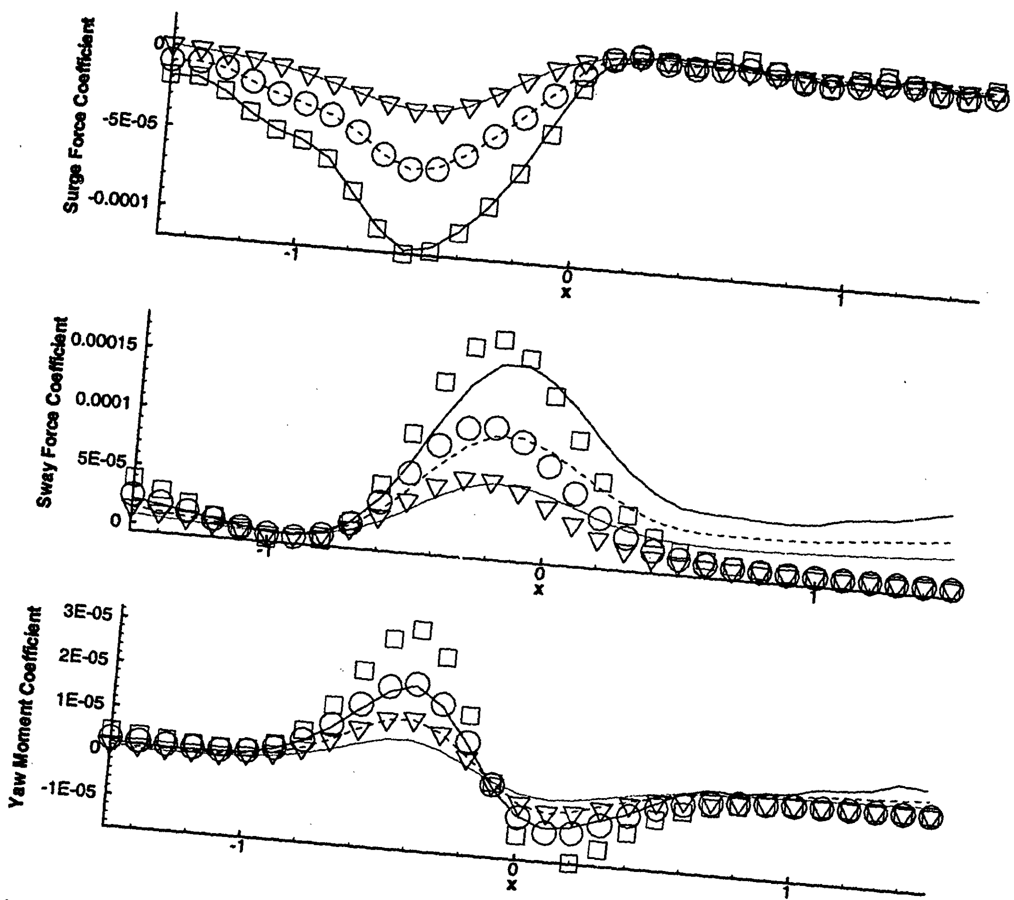

Figure 4-19: Comparison of forces on a VLCC that is moving with rectilinear motion with one that is allowed to move in the horizontal plane for the same initial conditions past a right-angle pier.

Chapter 5

Disparate Body/Panel Size Study

One use for general channel code is to model shipping scenarios in a harbor. Due to the range in size of bodies indicative of this environment (whales, tugs and tankers), the characteristic panel dimension of each mesh may differ greatly. This is of importance because a guideline in low order panel methods is to have panels in proximity with equivalent characteristic panel dimensions. If a shallow channel is to be modeled, one needs to know how small the clearance between the ship hull and the channel bottom can be, as a function of the characteristic panel dimensions.

To investigate, a study is performed modeling a 300m VLCC passing a 1m diameter sphere, and a 50m sphere passing a .1m, 1m, 2m, and 4.95m sphere; the 4.95m sphere has the same volume as the whale used in [6], [5], and [7]. The rectangular channel code is used for the studies in this chapter. All bodies are run with multiple panelizations. The motions of small bodies as a result of a much larger body passing are studied. Convergence studies are done in time and space.

5.1 Mines

In looking for similar studies, reports on mine damage were looked at in hopes of providing insight to the interactions of disparately sized bodies.

There are three main types of maritime mines: a floating mine, a moored mine, and a bottom mine. The floating mine is neutrally buoyant and usually floats near the surface. The moored mine is positively buoyant and must be anchored to the bottom. This mine is typically used in shallow water. The bottom mine is negatively buoyant and rests on the bottom, and is typically used in shallow water.

Three methods of actuation of mines are influence, contact and controlled. An influence mine may use a magnetic, acoustic, or pressure activated detonator, or a combination of detonators. A contact mine requires physical contact to be actuated. Controlled mines are detonated from land-based control centers.

Most mines reported in World War II [8] were influence mines. Only one instance is known to be a contact mine, a Japanese drifting mine hitting the US destroyer Abner Reid in July 1943. Due to the Hague Convention of 1907, the use of drifting mines has been limited [15]. However, they were used in the Persian Gulf 1987-88 (not by the US [14]) and in the Iraqi invasion of Kuwait, but collision and damage reports are not referenced in the publications I was able to find. This is of importance because though there have been studies of mine damage to ships, most of these mines were implied to be moored mines hence data on floating mines is not as readily available.

With the current computer model, each type of mine could be modeled, though only the influence and contact mines could be studied in any detail.

5.2 Sphere/Sphere Study

A closed form solution is known for the streamlines past a sphere in a uniform flow. Thus numerical results from a panel method simulation of a small sphere past another sphere may be compared to analytical results, as a test of the accuracy of the numerical method. In the limit that the size of the smaller sphere approaches the size of a water particle, the path of that sphere should lie on one streamline. This section contains a discussion of the scenario and the results from the analytical method, a convergence study of the size of the small body, and a time step convergence for such a geometry. Figures 5-2, 5-4 and 5-6 show the panelizations used for this study and the Ship/Sphere study in the following section. Figures 5-1, 5-3 and 5-5 are the some of the ship discretizations used in the Ship/Sphere study.

5.2.1 Simulation Criteria

A 50m, 1024 panel sphere is used. This sphere is free to move in surge and sway. The small sphere is discretized with 256 panels at .1, 1, 2.5 and 4.95m diameters, and a 1024 panel sphere is discretized with a 1m diameter. The small sphere is free to move in surge, sway, and heave. The channel depth is 6000m and the width is 6000m, 300 times the diameter of the largest body and assumed "infinite". The bodies are run at the center of the channel, with the initial coordinates (-330,3000,3000) and (0,3000,3000) respectively. The standard time step is 2.5s. Time steps (Δt) of 1.25, and 5 are also used. Note that these time steps have dimensions, while those used in chapters 4 and 6 have been non-dimensionalized.

The axis range on the plots is nondimensionalized with respect to the diameter of the large sphere. The numerical results of a large sphere passing a much smaller sphere are obtained using the Chanel code with the rectangular channel Green function. The results are shown in the body coordinate system of the larger sphere so they may be compared to the streamlines obtained using equation (5.1). The initial position of the spheres is the same as in the ship/sphere cases. The number of time steps is 300.

5.2.2 Streamlines Past a Sphere

Figure 5-7 shows the streamlines past a sphere of unit radius in a flow with unit velocity in the $-x$ direction. The streamlines are placed with .1 spacing between $y = 0.0$ and $y = 1.0$. The streamlines were computed by using equation (5.1) and using both secant method and regula-falsi iterative methods, choosing an initial position, calculating the stream potential at that point, then finding other points in the flow with that same stream potential.

The flow around the sphere is axisymmetric. In §6.8 of [2], Batchelor derives the

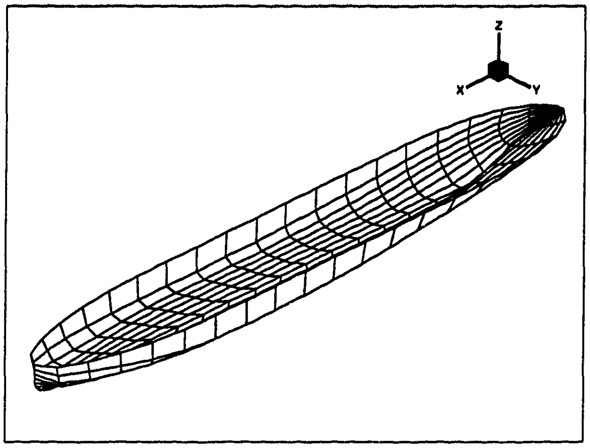

Figure 5-1: 280 panel VLCC.

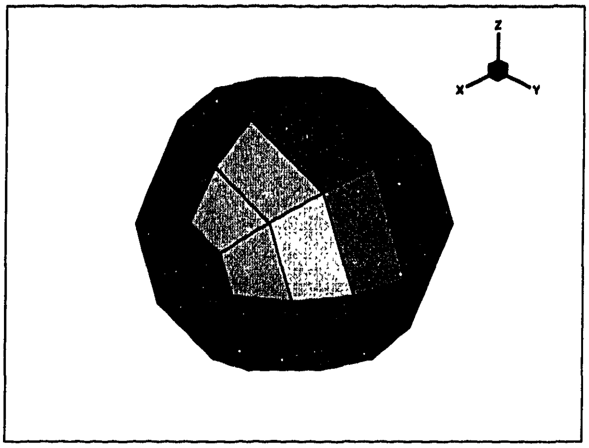

Figure 5-2: 64 panel sphere.

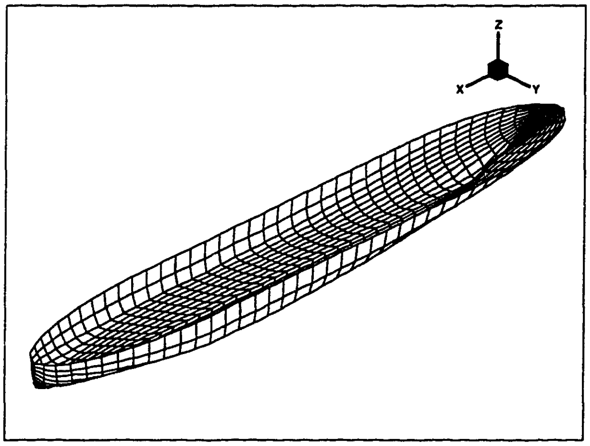

Figure 5-3: 820 panel VLCC.

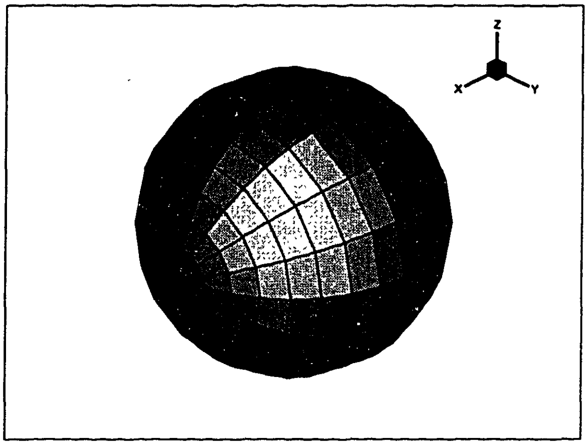

Figure 5-4: 256 panel sphere.

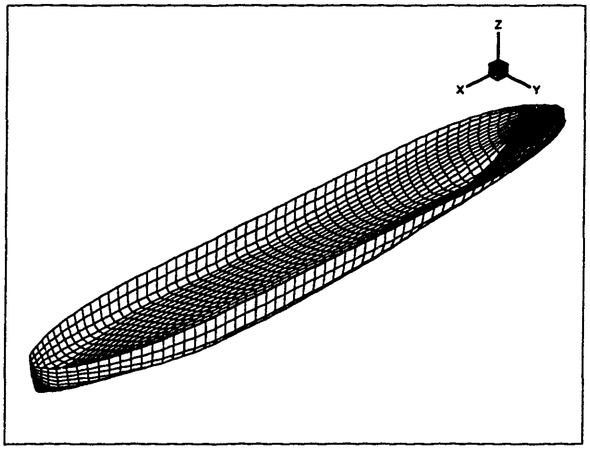

Figure 5-5: 1680 panel VLCC.

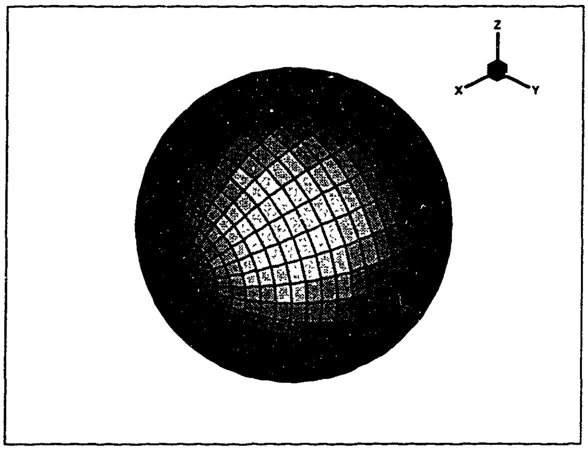

Figure 5-6: 1024 panel sphere.

stream function for a sphere in a flow in terms of fluid velocity, sphere radius, and radius and theta of the point of interest in the fluid.

$$\psi = -\frac{1}{2}Ur^2 sin^2\theta(1 - \frac{a^3}{r^3}) \tag{5.1}$$

where a is the radius of the sphere, r is the radial distance from the origin to the field point, and θ is the angle of the fieldpoint from the polar axis of the sphere. Figure 5-7 is the plot of the streamlines over which the numerical results are plotted. This plot shows the compression of the streamlines in the region of $-\frac{\pi}{2} < \theta < 0$. This is of significance because while a streamline may not hit the object it goes around, a body traveling on that streamline may collide with the object because the streamlines around the object compress. The distance between the surface of the object and the streamline the body is travelling on becomes less than the radius of the body, resulting in a collision.

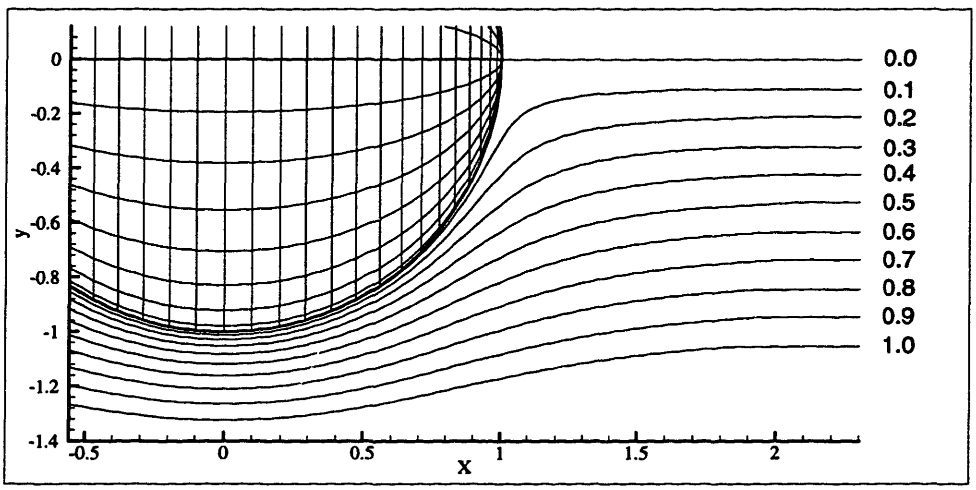

Figure 5-7: Streamlines past a sphere. Streamlines were started at fraction of large sphere beam stated, far in front of the sphere. The characteristic panel dimension is .2.

5.2.3 Effect of Small Sphere Size on Path

The convergence of the sphere path with the variation of sphere diameter is shown in Figure 5-8. Each sphere has 256 panels. Each time step is 2.5. The small sphere has diameters of .1, 1, 2, and 4.95m. The plot shows that the path of the sphere is unaffected by size in this range of diameters. This also implies that the whale used in the National Marine Fisheries Service (NMFS) study [6] [5] [7] does act as a water particle as it passes a body (shown in §5.4) and any collision that does result between a ship and a whale is due to the compression of streamlines around a body where the whale is closest.

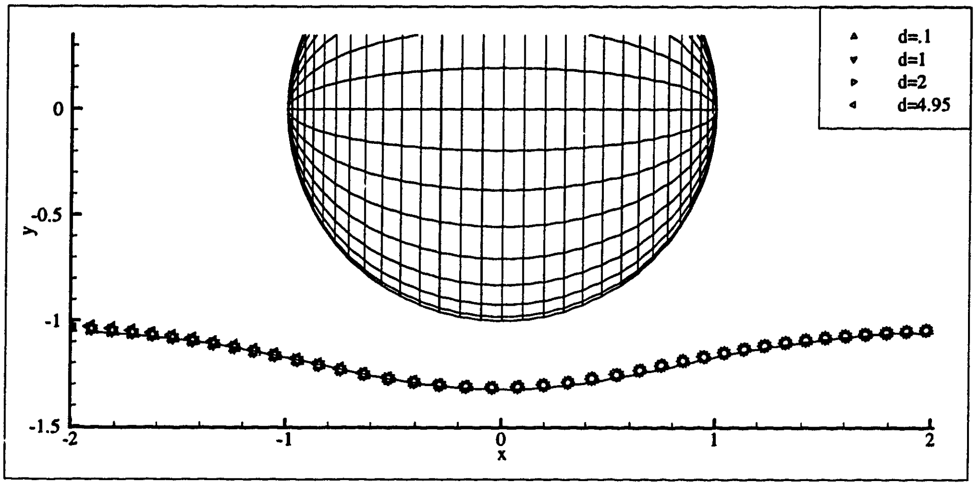

Figure 5-8: Sphere size convergence for large sphere passing small sphere. The small sphere has diameters stated in the legend. The large sphere is 50m in diameter and 1024 panels; the small sphere has 256 panels. The solid line is the streamline the small sphere started on.

5.2.4 Time Step Convergence of Numerical Solution

Figure 5-9 shows the convergence of the small sphere path with the reduction of the time step. The small sphere diameter is 1m, 256 panels are on both bodies, and the time steps are 1.25, 2.5 and 5. There is a "phase shift" in position that appears in the run $\Delta t = 5$. This shift appears to be on the order of a time step, thus it should disappear with the reduction of the time step, and we see that it does. This plot shows that the results are converging to a path similar to the streamline the sphere initially starts on. Thus ($\Delta t = 2.5$) is adequate for converged results.

A convergence test of the discretization of either sphere is done, keeping in mind the MPAR (Mean Panel Area Ratio). A large sphere with 1024 panels and a small sphere with 256 panels yielded the best results. The limiting factor in the simulations

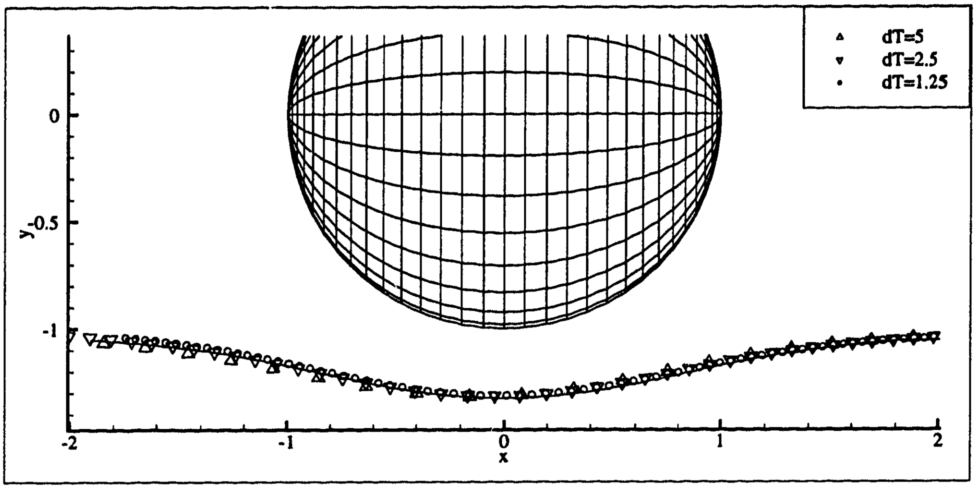

Figure 5-9: Time step convergence for large sphere passing a small sphere. Coordinate system origin is at the center of the large sphere, nondimensionalized by the radius of the larger sphere, $R = 25m$, and are in the large sphere frame. The large sphere is 50m in diameter and has 1024 panels; the small sphere is 1m in diameter and has 256 panels. dT is the time step in seconds. The solid line is the streamline that the spheres began on.

of disparate bodies passing is the characteristic panel dimension of both bodies. For an accurate solution of the source formulation, the bodies may only be as close as 2 characteristic panel dimensions in the region of the bodies where they are closest when passing. In the case of the two spheres shown above, for the 1024 panel large sphere and 256 panel small sphere, the characteristic panel dimension for $(-\frac{\pi}{2} < \theta < 0)$ is in the range of 2.25-3.25m.

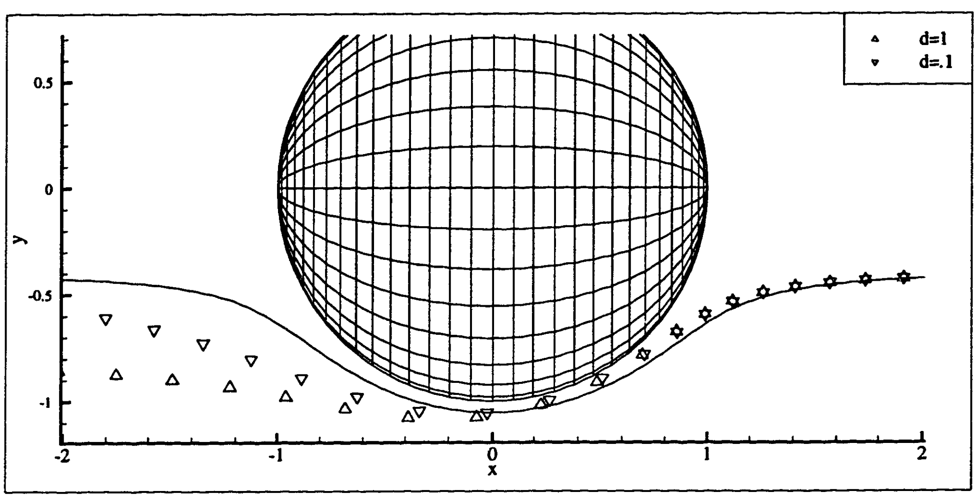

Figure 5-10: Path convergence for small sphere very close to the large sphere, with variance of the small sphere diameter. The solid line is the streamline the small sphere began on.

The result of the error incurred when the bodies are closer than 2 characteristic panel dimensions is shown in 5-10. There are 1024 panels on the large sphere and 256 on the small sphere. The time step is 2.5 and both 1m and .1m diameter small spheres are used. The initial deviation from the streamline may be due to momentum but the deviation is only noticable once the small sphere is within 2 panel dimensions of the large sphere, so it difficult to determine which condition is the cause for the deviation from the streamline. In any case as the small sphere passes $\theta = -\frac{\pi}{4}$, the two spheres begin to follow the same path, divergent from the streamline. The streamline is used merely as a reference point; the important result is the sphere positions are no longer on the same for each time step. Figure 5-8 shows that small spheres ranging in diameters .1 to 4.95 passing a large sphere with a diameter of 50, all act as particles in the flow past the larger sphere. This is not the case in Figure 5-10 due to the divergence after passing $\theta = -\frac{\pi}{4}$. This divergence may be credited to the bodies coming within 2 characteristic panel dimensions.

5.3 Ship/Sphere Study

This study tested the limit of panel methods, concerning disparately sized bodies. It is known that proximate panels should have similar characteristic dimensions [4], however this leads to problems with a very large number of unknowns if the size of the bodies differs greatly. In the case explored here, over 6 million panels would be required for the ship for only 256 panels on the sphere, for the characteristic panel dimensions to be of the same order. Given current technology, a run with this number of unknowns is unreasonable. However, results converged to graphical accuracy may be obtained with far fewer unknowns. For the geometries tested, the ratio of the characteristic panel dimensions does not need to be O(1), as suggested in [4], but $O(10^{-3})$.

Ship–Sphere	32 (4x4)	64 (8x4)	128 (8x8)	256 (16x8)	400 (20x10)	576 (24x12)	1024 (32x16)
140(14x05)	X	X	X	O			
280(20x07)	X	X	X	X	O	O	O
392(28x07)	X	X	X	X		O	O
820(40x10)	X	X	X	X		X	O
1680(60x14)				X		X	X
3360(80x21)	X	X	X	X	X	X	

Table 5.1: Test Matrix for Ship/Sphere study. The numbers indicate the number of panels on the body (total panel number and (LENGTH)x(GIRTH) for half body)

5.3.1 Simulations

A 300m VLCC is used with the following numbers of panels: 140, 280, 392, 820, 1680, and 3360. The ship is free to move in surge sway and yaw. A 1m diameter sphere is used with the following numbers of panels 8, 32, 64, 128, 256, 400, 576, and 1024. The sphere is free to move in surge, sway, and heave. The channel depth is 20m and the width is 6000m. The position of the bodies is set at the center of the channel. The time step is 5s.

Table 5.1 shows the ship/sphere combinations run and whether the results were the converged results (X) or not (O). The trend of the non-converged results (O) indicate the ratio of a characteristic of the panelizations affects convergence. This is further discussed in §5.3.5.

5.3.2 Time step Convergence

Figure 5-11 shows the convergence in time step for the ship/sphere study. The ship has 400 panels and the sphere has 256 panels. Time steps of .5, .7, 1, 2.5, 5, 10, and 20s were tested. The initial positions of the ship and sphere are centered at $(-330, 3000, 0)$ and $(0, 2990, -2)$ respectively. The coordinates are dimensioned in meters. The results indicate that a time step of 5 is adequate for converged results.

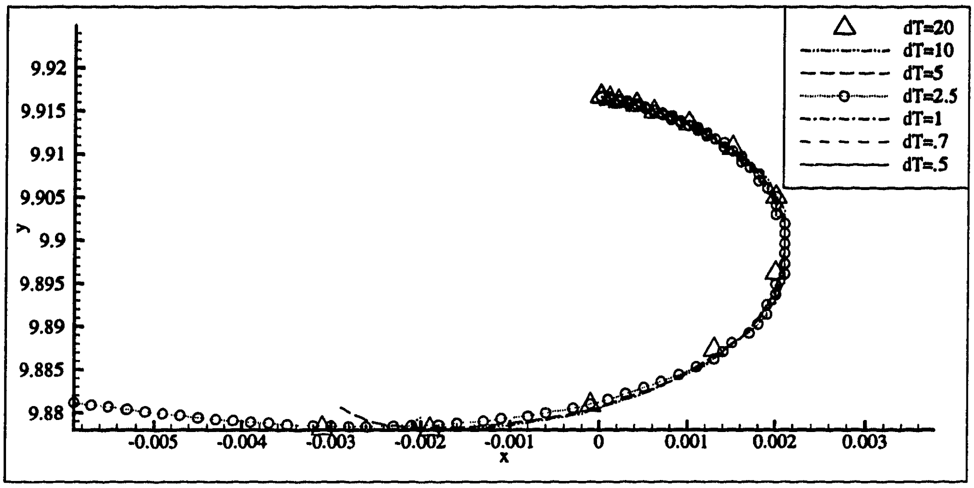

Figure 5-11: Temporal convergence test. Path of sphere in global frame due to influence of 300m VLCC. dT=time step in seconds. Velocity is of unit magnitude. Axis units normalized by length of ship.

5.3.3 Small Body Discretization Variance

Figure 5-13 shows the results for convergence in force on a sphere for a fixed ship discretization and varying the sphere discretization. The ship used in this test has 280 panels (Figure 5-1). The corresponding convergence test for the path of the sphere is shown in Figure 5-12. The surge plot shows the force on the small sphere with 400, 576 and 1024 panels diverging from the force on the sphere with coarser panelizations. This is counterintutive, since it is often the case that as the discretization is made finer, the results converge, not diverge. This trend is not seen in the sway force plot. However, if we look at the plot of the path of the small sphere in the global frame, the results from the higher discretizations are also diverging from the paths of the coarser spheres. Apparently due to finer discretizations, this divergence is interesting and suggests a convergence criterion dependent on relative panel characteristics between bodies.

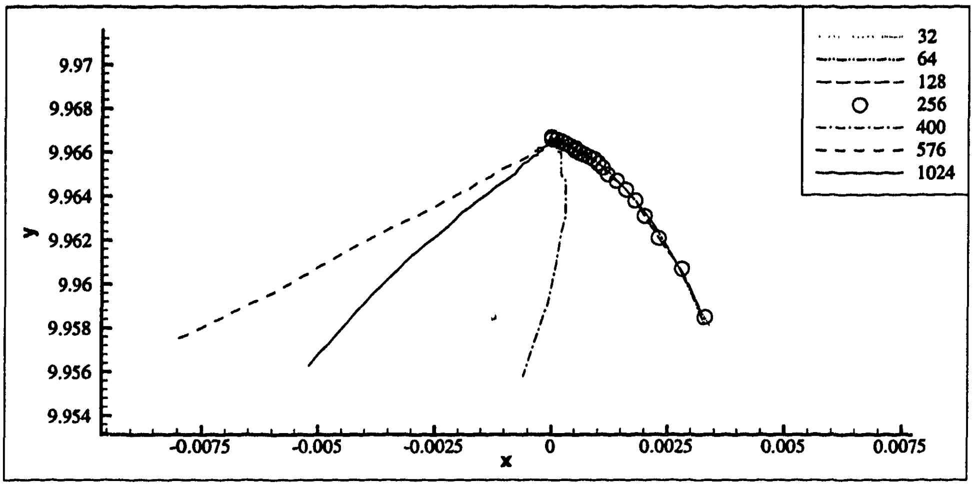

Figure 5-12: Path convergence test with variance of sphere discretization. Path of sphere in global frame due to influence of 300m 280 panel VLCC. Legend shows sphere panel number for entire sphere.

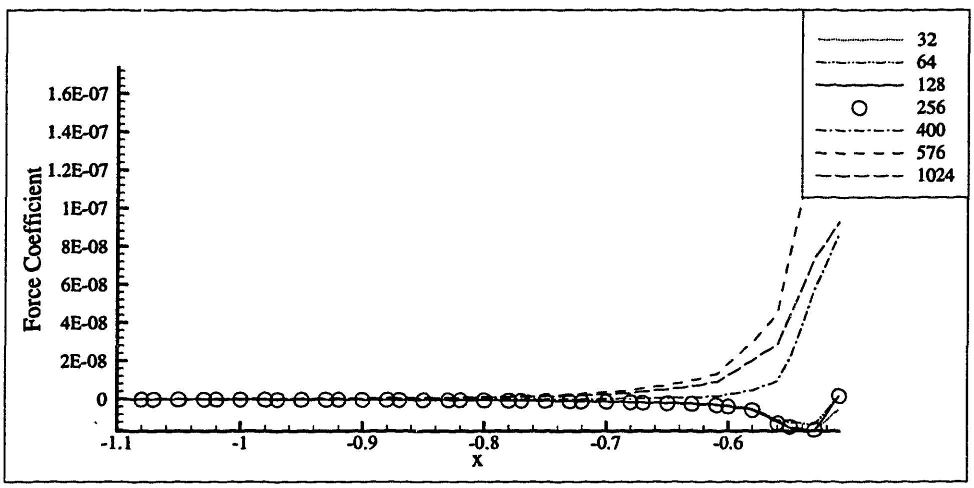

Figure 5-13: Surge force convergence test. The horizontal axis is the position of the ship at the time when that force was induced on the sphere. The vertical axis is the force non-dimensionalized. The numbers in the legend indicate total number of panels on sphere.

5.3.4 Large Body Discretization Variance

Figure 5-16 shows the results for convergence in force on a sphere for varying the ship discretization and varying the sphere discretization. The sphere used in this test has 256 panels. The corresponding convergence test for the path of the sphere is seen in Figure 5-15. The surge force plot for this scenario shows typical convergence as the discretization becomes finer for the ship. The sway force plot appears to

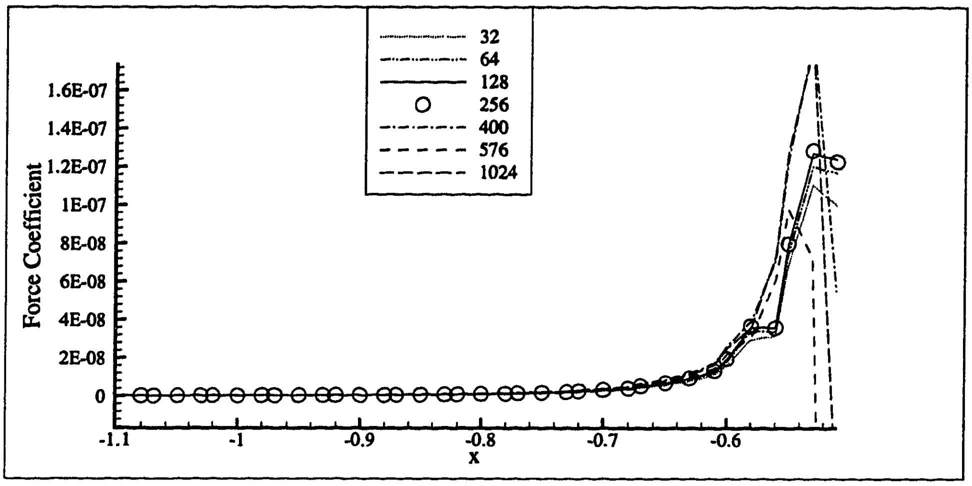

Figure 5-14: Sway force convergence test. The horizontal axis is the position of the ship at the time when that force was induced on the sphere. The vertical axis is the force non-dimensionalized. The number in the legend indicate total number of panels on sphere.

be converging or converged for every discretization. The path plot in Figure 5-15 confirms that converged results are given for ship discretizations of 820 panels and more. While this test does not suggest a relationship between panel characteristics on bodies, it does support the known idea that for panel methods, results converge as the characteristic dimension of panels in proximity on different bodies becomes similar.

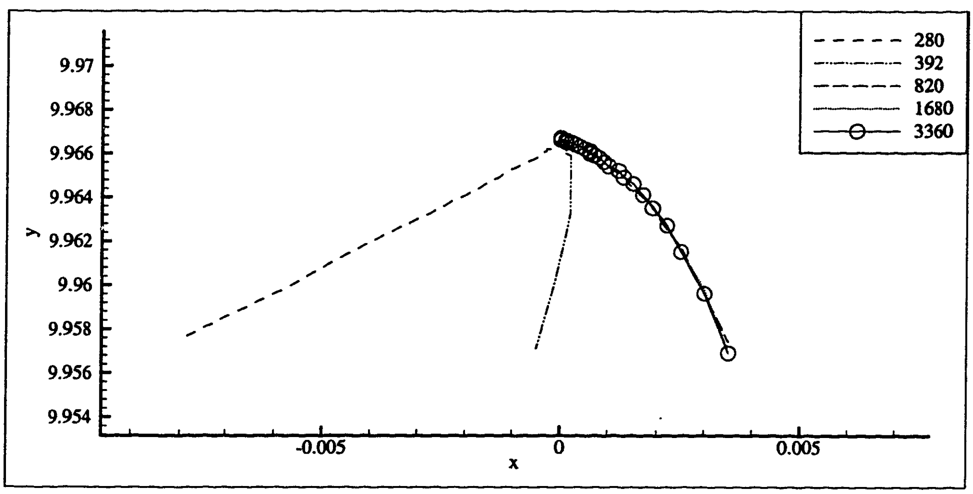

Figure 5-15: Path convergence test with variance of ship discretization. The legend shows the sphere panel number for the entire ship. The sphere has 256 panels.

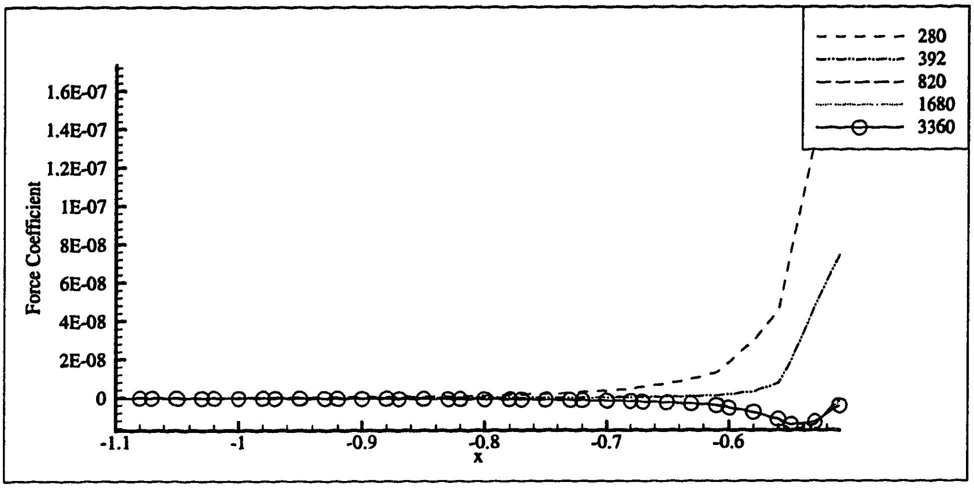

Figure 5-16: Surge force convergence with variance of ship ship discretization. The legend shows the sphere panel number for the entire ship. The sphere has 256 panels.

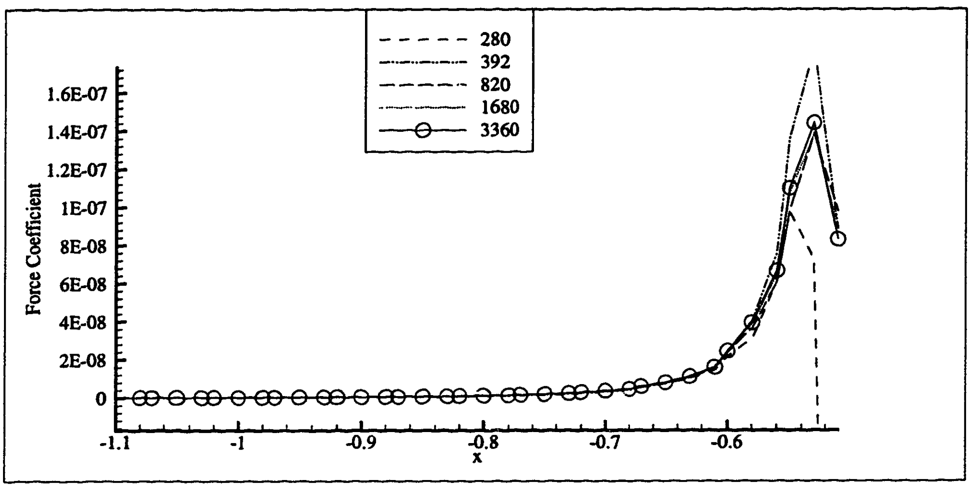

Figure 5-17: Sway force convergence with variance of ship ship discretization. The legend shows the sphere panel number for the entire ship. The sphere has 256 panels.

5.3.5 Mean Panel Area Ratio as a Convergence Indicator

The total number of panels for a run versus the ratio of the mean panel areas (MPA) of the two bodies is shown in Figure 5-18; the MPA of the smaller body is in the numerator. There is a point on the plot for each of the runs in 5.1. The line at the bottom of the plot, at $y = 1 \times 10^{-4}$ is the MPA ratio found to be the threshold for converged results for this ship/sphere geometry.

As the results from the above ship/sphere panel convergence tests indicate, there is a correlation between panel size on bodies in proximity and converged results. Figure 5-18 shows the ratio of the MPA on each body versus one over the total number of panels. The lines indicate constant ship discretization. They are drawn as a visual aid. There is a threshold value for the MPA ratio below which the code gives non-converged results for this simulation geometry. It is reasonable to conclude that such a threshold exists for other geometries, so these results can be used as a guideline as to whether the simulation will yield converged results when using sufficient temporal discretization by knowing only the MPA ratio.

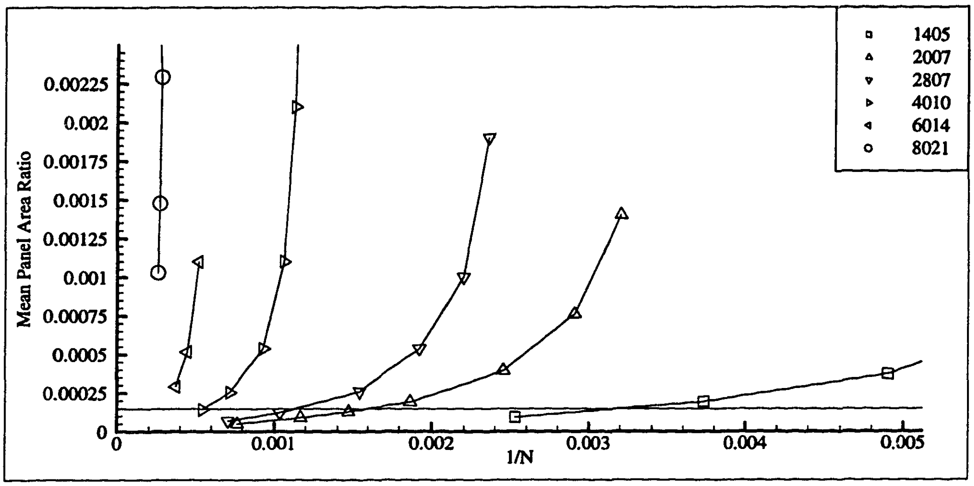

Figure 5-18: Mean Panel Area Ratio vs. 1/N. Lines through symbols are lines of constant ship discretization. Horizontal line at $y = 1.5 \times 10^{-4}$ is threshold for runs with converged results.

5.4 Application: Ship/Whale

Similar to the ship/sphere scenario outlined above, a ship/whale test is performed. The main purpose is to demonstrate the above findings to an audience not in the computational hydrodynamics community in a format they are more likely to understand. This portion of the research was funded by the National Marine Fisheries Service and the New England Aquarium.

The simulations for the report [5] were done with a 420 panel, 151m DDG-51 destroyer, a 280 panel, 300m SL7, a 280 panel, 307m VLCC and a 200 panel, 15m whale. The time step is 5 for the destroyer, and 10 for the SL7 and VLCC. The ship has a unit velocity in the positive x-direction and the whale has no initial velocity. The ship is free to move in surge sway and yaw; the whale is free to move in surge, sway, heave, pitch and yaw.

These tests show that in order to hit a whale, the whale must be within .9 of the ship beam, for a whale initially in the far field; or the whale must be within 1.4 of the ship beam if it surfaces just ahead of the bow. A whale with forward speed was also studied. In most cases, if the whale had any forward speed, it would be able to swim out of the path of the ship. However, collisions occur when the whale's direction and velocity take it very close to the bow; these are cases where collisions are obvious and hydrodynamics are not necessary for analysis.

To more closely examine where along the ship hull the whale collides, a finer discretization than what was used on the ship hull, would be necessary. For full details of this study, please see reference [5].

For this comparison between ship/whale and ship/sphere results, a scenario with a ship passing each body with identical initial conditions is run. A 300m VLCC with 280 panels is used for the first body. The second body is a 1m sphere as used previously in this chapter, a 4.95m diameter sphere with mass equivalent to the 15m long and 3.25m (at its greatest breadth) whale used here and in the NMFS report, and the whale. The dimensions of the whale were obtained from the average offsets of dead right whales studied by Omura [16]. See [6] for more information on the creation of the whale discretization. The water depth is 20m, width is 6000m, and a time step, $\Delta t = 5$.

The ship begins centered at $(-330, 3000, 0)$ and the whale and spheres at $(0, 2990, -6)$. The ship has an initial unit velocity in the positive x diretion and is free to move in surge sway and yaw; the whale has no initial velocity and is free to move in surge, sway and yaw in this comparison. Figures 5-19 and 5-20 show that using the whale

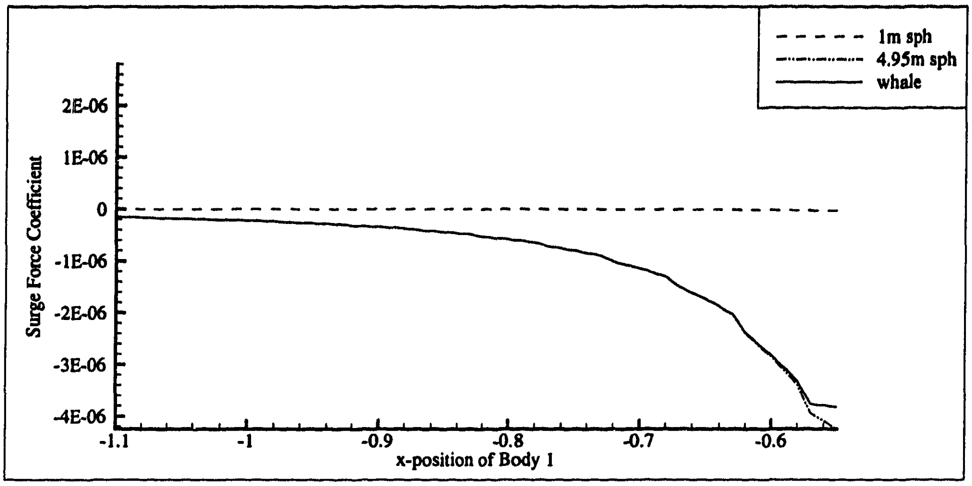

Figure 5-19: Surge force on a 1m sphere, 4.95m sphere and a 15m whale.

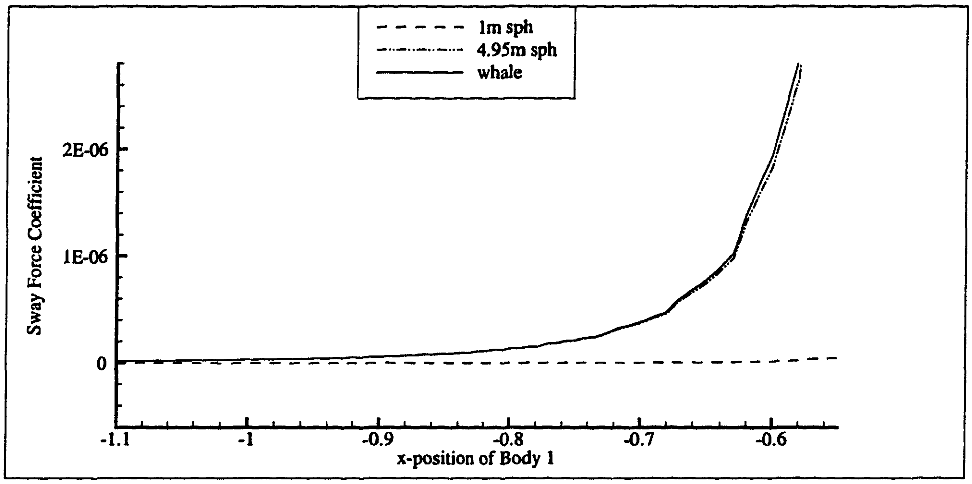

Figure 5-20: Sway force on a 1m sphere, 4.95m sphere and a 15m whale.

yields results which compare well with the ship/sphere result. Figures 5-21 and 5-22 are magnified to show the trend of the force on the 1m sphere. It follows the trend set by the larger bodies. Figure 5-19 and 5-21 indicate the bodies are initially pushed away from the approaching ship, as found for a ship passing another ship [9]. The sway force plots (Figures 5-20 and 5-22) show the bodies pushed away from the centerline of the approaching ship, also as expected. The force plots are truncated because body collisions occured. The comparison of the paths of the bodies shows the larger bodies following the same path as the small sphere, though the whale deviates from the path slightly, most likely due to its non-uniform shape. From this, we may

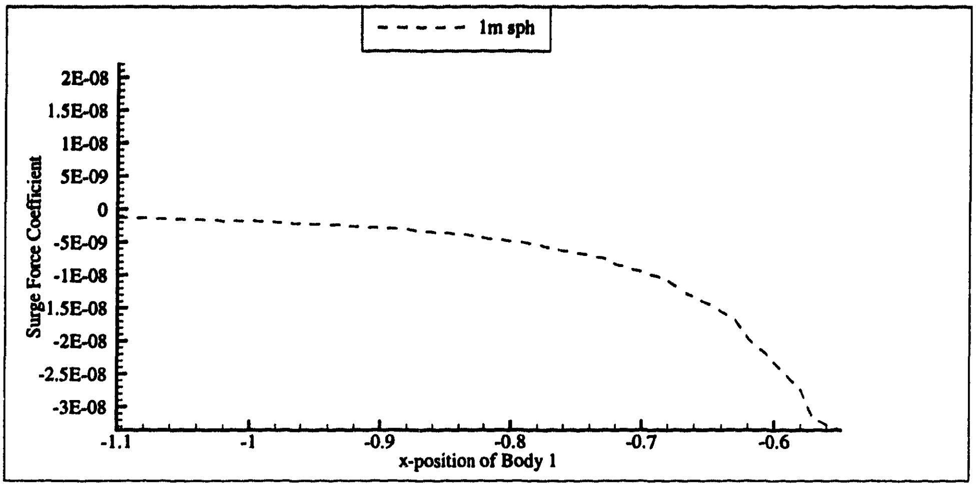

Figure 5-21: Surge force on a 1m sphere.

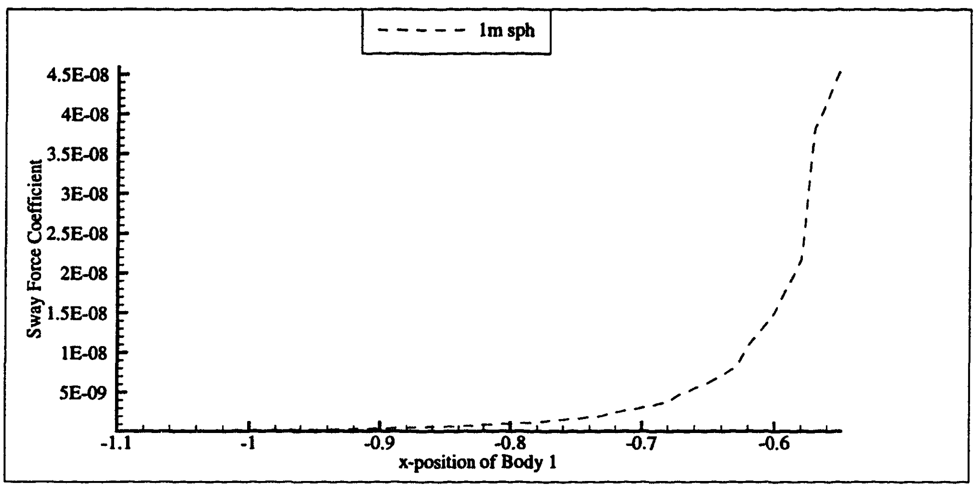

Figure 5-22: Sway force on a 1m sphere.

conclude that a passive whale does respond like a water particle, though due to its size, may still be close enough to collide with the hull of a ship.

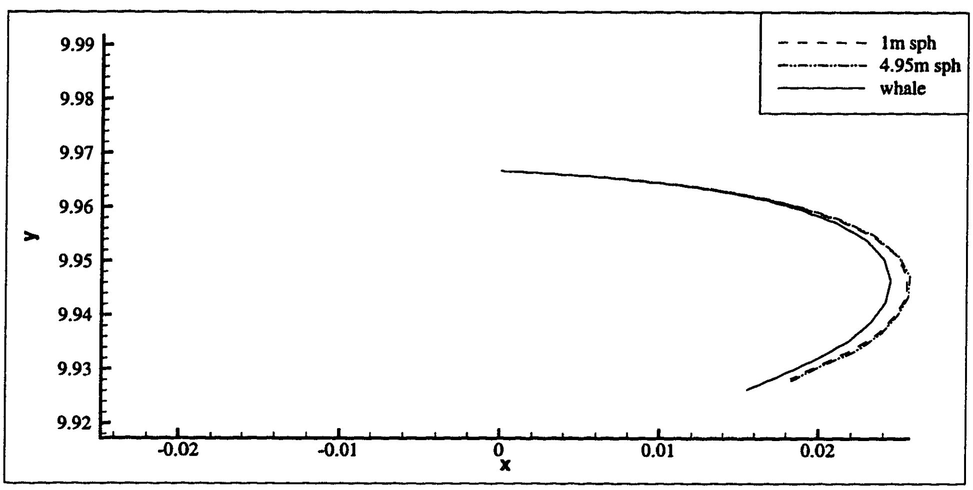

Figure 5-23: Path of a 1m sphere, 4.95m sphere and a 15m whale in the global coordinate system.

Chapter 6

Arbitrary Channels and Mooring with Damped Springs

This chapter shows results from simulations we were unable to model prior to the modifications made in the course of the research for this thesis. These results include body motions and forces on bodies in the vertical modes due to channels with varying depth and body motions and forces on bodies moored with damped springs.

6.1 Channels with Arbitrary Topography

The purpose of this study is to model a body moving in a channel with a varying cross section, i.e. arbitrary bathymetry. The forces on the ship will be analyzed. A channel with a step (a 90^o rotation of the Yeung and Tan scenario, but with a submerged body) and a channel with bottom undulations are used. While Yeung and Tan could perform these particular tests (in a coordinate system rotated 90^o about the x-axis with respect to the one used here), the ability to make the topography completely arbitrary, in both side and bottom contours, is what makes this code so powerful.

6.1.1 Channel with Step Bottom

Spheroid $\mathcal{B}$ at an initial position of $(-1, 0, -.4, 0, 0)$ is run from a channel section of depth 1.6 to a depth of .8 and back again. A second spheroid is present in the channel at $(-1, 0, -1.2, 0, 180)$. The bodies are free to move in surge, heave and pitch. The step is at $x = 0$, as seen in Figures 6-1 and 6-2. The forces and moments on body

1 for both geometries in Figure 6-1 are shown in Figure 6-3. The squares and the dashed line represent the forces for the spheroid approaching the step. The circles and the dotted line represent the forces for the spheroid leaving the step. The surge force indicates a repulsion as it goes over the step, similar to the surge repulsion seen in the VLCC past a right-angle pier, Figure 4-18. As expected the forces on the spheroid approaching and leaving are opposite in sign and time. The heave force plot also exhibits the temporal anti-symmetry seen in surge (and later in pitch).

For heave, as the spheroid approaches the step, it is first pulled toward the free surface, but as it passes over the step, it is pulled down again. Looking closely, the heave force is seen to taper off just as the bow passes the step and then as soon as more than half the hull is past the edge of the step, the body heaves down again. The shift by a constant seen in the heave force is due to the change in initial geometry, i.e. the ratio of the distances from the free surface and the bottom. As mentioned above, there is temporal anti-symmetry in pitch also. We see that as the spheroid passes over the step, the bow pitches up, and as it leaves the step, the bow pitches down. This trend is what Yeung and Tan [21] were able to show for the yaw moment as a ship passes a right-angle pier. Figure 6-4 shows the forces on body 2 as body 1 passes over the step in either direction, or just moves along in a channel with no step; the same symbols are used as above. We can see that the effect of the step on the forces on body 2 is small, i.e. for a body motionless in the water near a step, the difference in force is negligible. It is reasonable to suggest the position of body 2 relative to the step is very important as far as the forces imparted on it by body 1, and in which case, this geometry is not the most interesting. A more interesting case would place the second body much closer and parallel to the step. However, this case does present some interesting results seen in Figure 6-5, where the forces on body 1 are compared for the effect of the presence of the second body on body 1. We can see the force of the step is the dominant force on body 1. Unfortunately, both Figure

6-4 and 6-5 suggest the bodies are too far apart to have much effect on each other. For the channel without the step, the forces on the bodies are nearly constant, with deviations due to the channel ends and interaction with the other body .

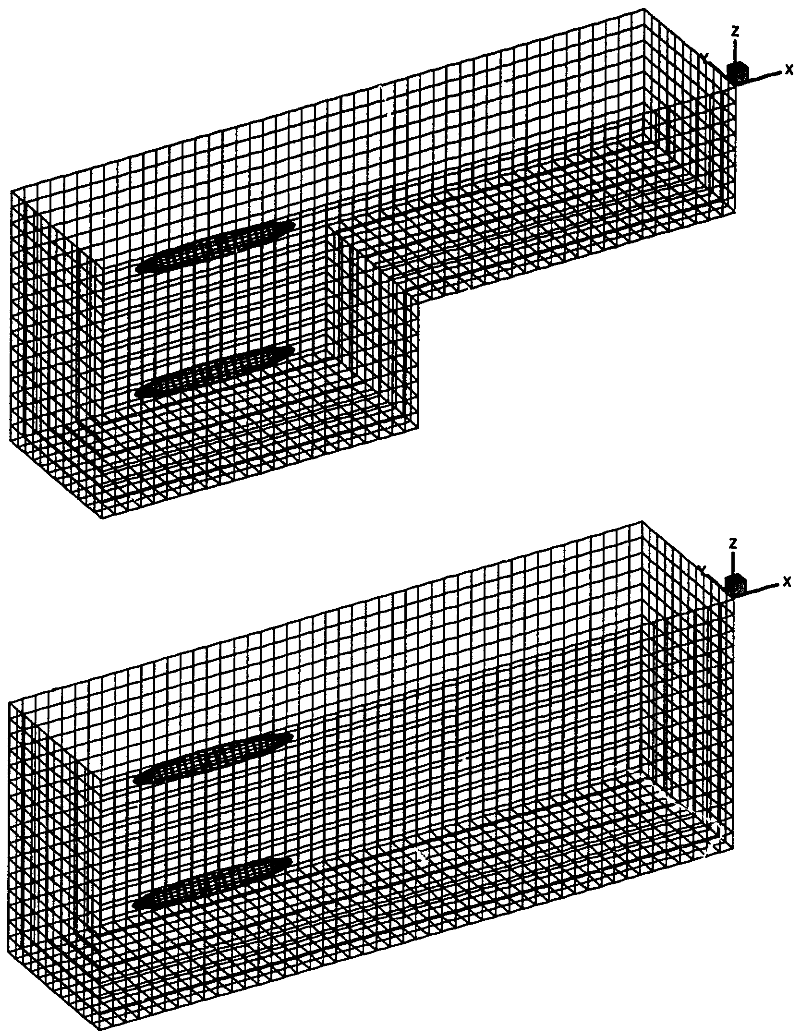

Figure 6-1: Geometry for a spheroid approaching a step with another body present. The same geometry without the step is also shown.

6.1.2 Undulating Bottom

This study is a demonstration of the flexibility of the code, with possible use as verification with an Australian Maritime College tow tank project studying the effect of undulating channel bottoms on ships [1], if and when the results are published. A sample geometry is shown in Figure 6-6.

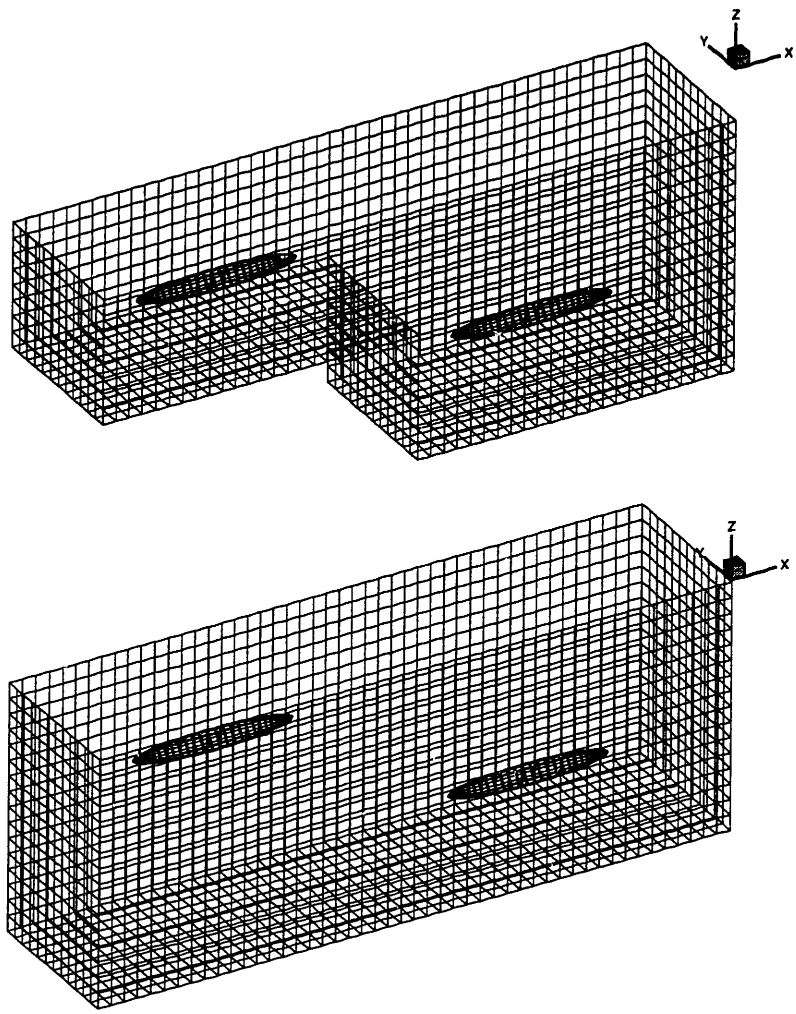

Figure 6-2: Geometry for a spheroid leaving a step with another body present. The same geometry without the step is also shown.

Cases are run with a VLCC moving with rectilinear motion; the body is not allowed to accelerate in any direction. The VLCC has an initial position of $(-1, 0, 0, 0, 0)$ and a positive initial unit velocity in surge. The channels have a mean depth of .35 and a length of 4. The amplitudes of the undulations are .05 and .1. For the amplitude of .05 the wave length of the undulations is 1. For amplitudes equal to .1, the wave lengths are equal to $.5(\tilde{\mathcal{A}})$, $.75(\tilde{\mathcal{B}})$, $1(\tilde{\mathcal{C}})$ and $2(\tilde{\mathcal{D}})$. The case where the body is free to move yields very small difference in the forcing, a maximum of 6% in the first half of the run for heave and pitch, increasing to 13% in heave and 9% in pitch for the second half of the run. Surge varied as much as 120% (at $x = .9$).

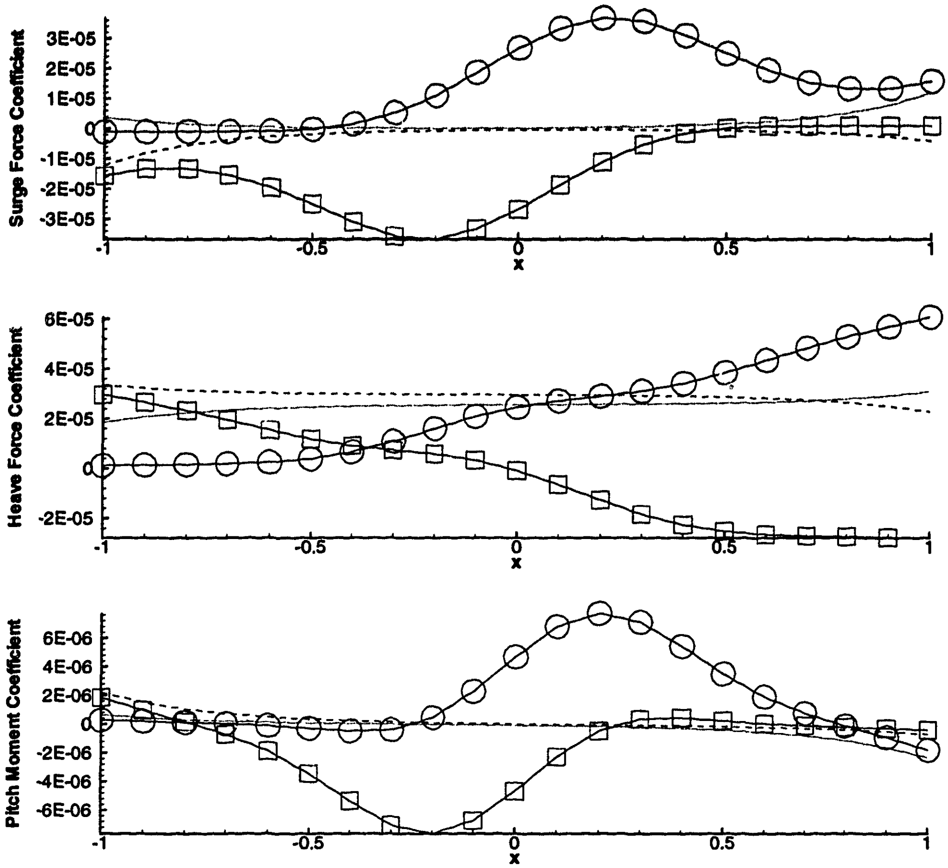

Figure 6-3: Forces on a submerged body passing a step, with a second body present compared to the same bodies moving in a channel without a step.

Figure 6-7 illustrates the directly proportional effect of the amplitude of the bottom undulations on the force experienced by the body. The force plots have been aligned with the channels so it is clearer to see when in the channel the ship experiences the associated force. The three plots are surge, heave and pitch. The flat bottom channel is represented by the triangles, the channel $\tilde{\mathcal{A}}$ is shown by the left triangles, and the channel $\tilde{\mathcal{B}}$ is shown with the gradient symbol. As the amplitude of the undulation is halved, so is the force experienced by the VLCC; these results suggest this to be a linear relation. However, the effect of the wavelength of the undulations does not appear to be linear with the magnitude of the forces, but the frequency of the oscillations in the forcing is proportional to the frequency of the bottom undulations.

Figure 6-8 provides better data for the relation of forcing with the ship position in

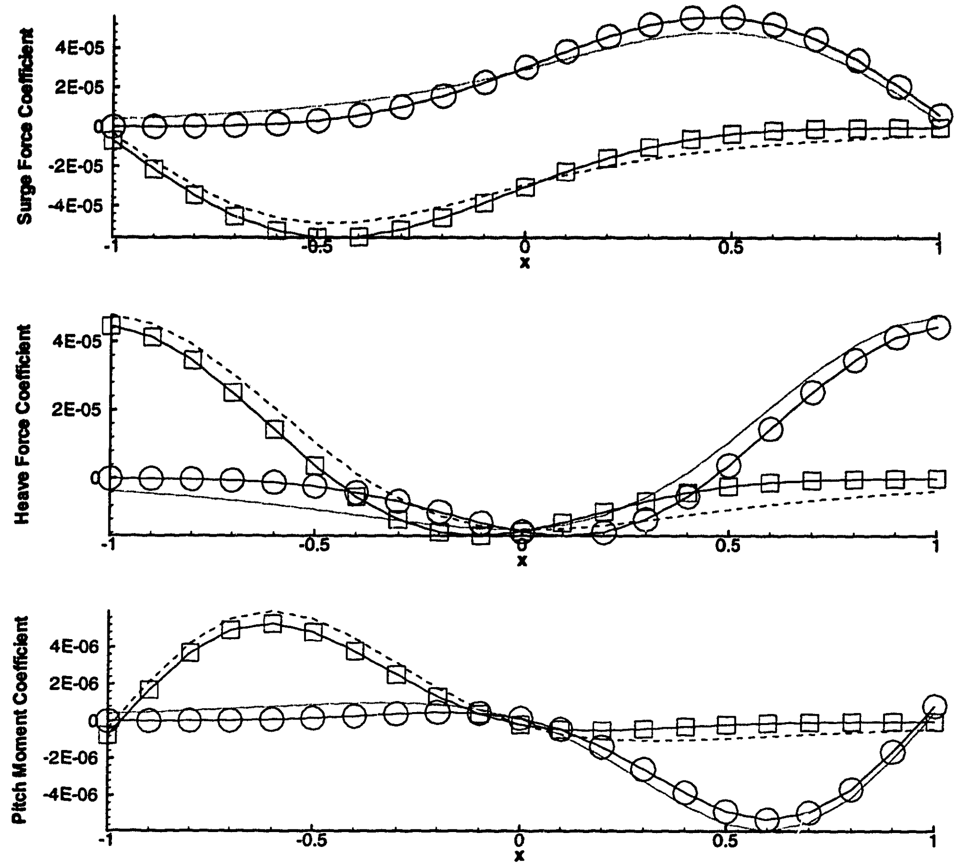

Figure 6-4: Forces on a body in a channel with a step as another body passes over the step compared with the same bodies in a channel without a step.

the channel. Channel $\tilde{\mathcal{A}}$ is represented by the dashed line, channel $\tilde{\mathcal{B}}$ is represented by the dotted line, $\tilde{\mathcal{C}}$ is represented by the solid line, and $\tilde{\mathcal{D}}$ is represented by the long dashed line. Just after the ship passes over the peak of an undulation, it experiences a maximum surge forward. As it approaches another undulation peak and the bow is just past being above the peak, the ship experiences a maximum surge force backwards. This is valid for undulations equal to or longer than the length of the ship (channels $\tilde{\mathcal{C}}$ and $\tilde{\mathcal{D}}$). For channel $\tilde{\mathcal{A}}$, maximum surge occurs with the center of the ship between the trough and peak, a phase shift of -90^o. For channel $\tilde{\mathcal{B}}$ maximum surge occurs with the center of the ship just past an undulation peak and maximum negative surge just past a trough, about 40^o out of phase with the channel.

Pitch is nearly in phase with surge, perhaps phase shifted 20^o, experiencing a

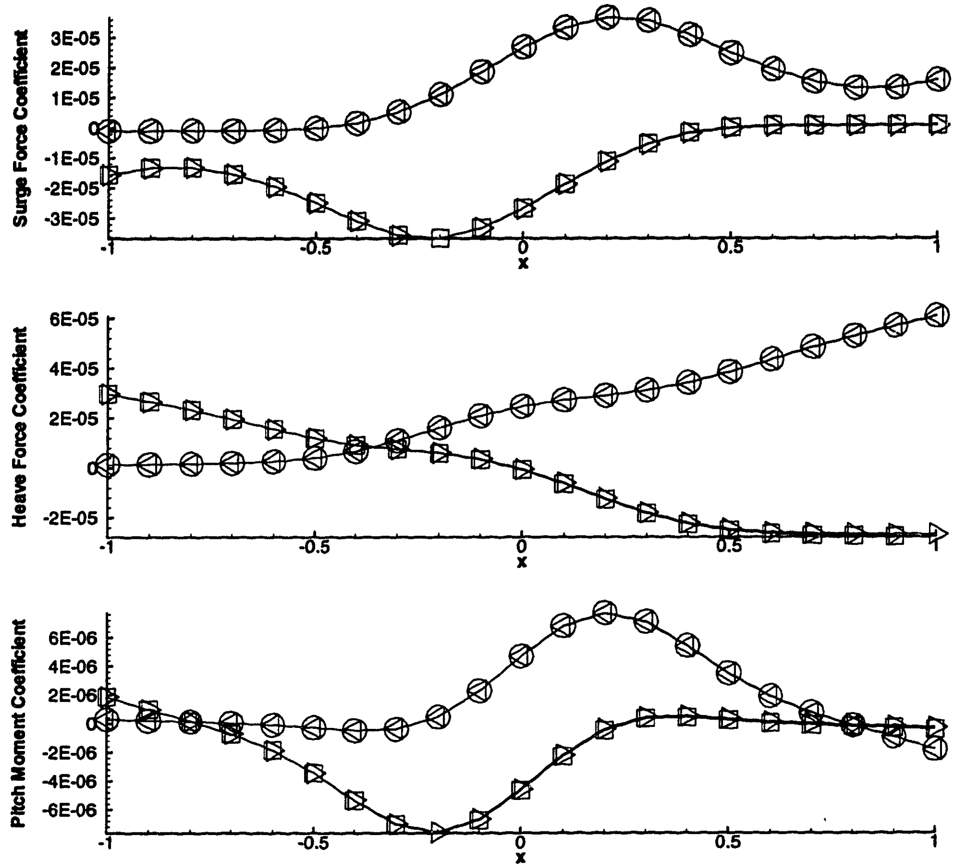

Figure 6-5: Comparison of forces on the body moving past a step with and without a second body present.

maximum bow-down just as the center of the ship is 1/3 of the way between peak and trough ($\frac{\pi}{3}$ if the undulation peak is at zero). This is the case for channels $\tilde{\mathcal{B}}$, $\tilde{\mathcal{C}}$ and $\tilde{\mathcal{D}}$; the magnitude for pitch moment from channel $\tilde{\mathcal{A}}$ is negligible compared to the others.

Maximum heave appears to be out of phase with the channel undulations by 60^o for channel $\tilde{\mathcal{A}}$, -30^o for channel $\tilde{\mathcal{B}}$, and -60^o for channels $\tilde{\mathcal{C}}$ and $\tilde{\mathcal{D}}$. This means for the channel with the shortest undulation wave length, maximum heave is experienced after the center of the ship passes the shallowest draft. For all other wave lengths, the maximum heave happens prior to the center of the ship reaching minimum draft. For these longer wave length cases this also means that maximum squat (negative heave) occurs prior to reaching the maximum draft. The problem of achieving maximum squat with minimum draft occurs if the forcing and motions are 180^o out of phase with the undulations.

That the forces, shown in Figure 6-8 were reduced siginificantly as the wavelength of the undulations went from being on the order of the ship length to half the ship length implies that undulations that prove problematic for medium sized container vesels, would have a minimal effect on the very large container ships and tankers.

A more thorough study of this phenomenon is recommended, including investigation of whether the undulations could force the ship at a resonant frequency, and what the resultant motions would be.

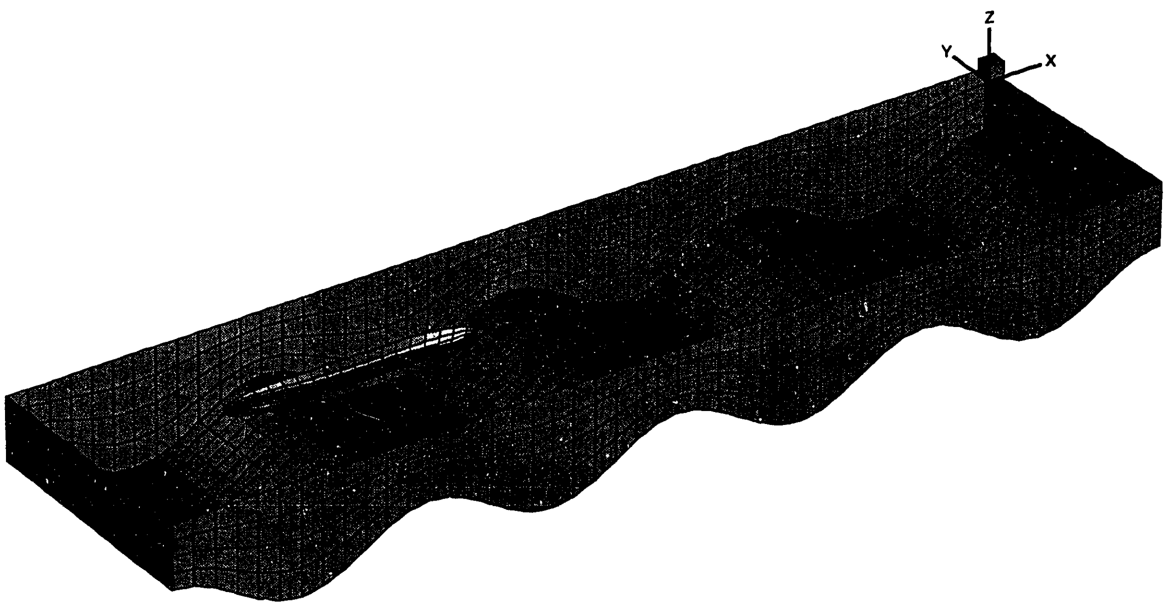

Figure 6-6: Geometry for a VLCC in a channel of mean depth .35 with an undulating bottom of wavelength 1 and amplitude .1.

For another scenario with a channel with an undulating bottom, a 688 class submarine is run at a depth of .3 in channel of length 4, mean depth .6, and width 1 (see Figure 6-9). The wavelength and amplitude of the channel bottom is 1 and .1, respectively. This case run with vertical body motions allowed.

Figure 6-10 shows the surge force, heave force, pitch moment, and pitch angle in degrees in relation to the submarine's position in the channel. The skewness in

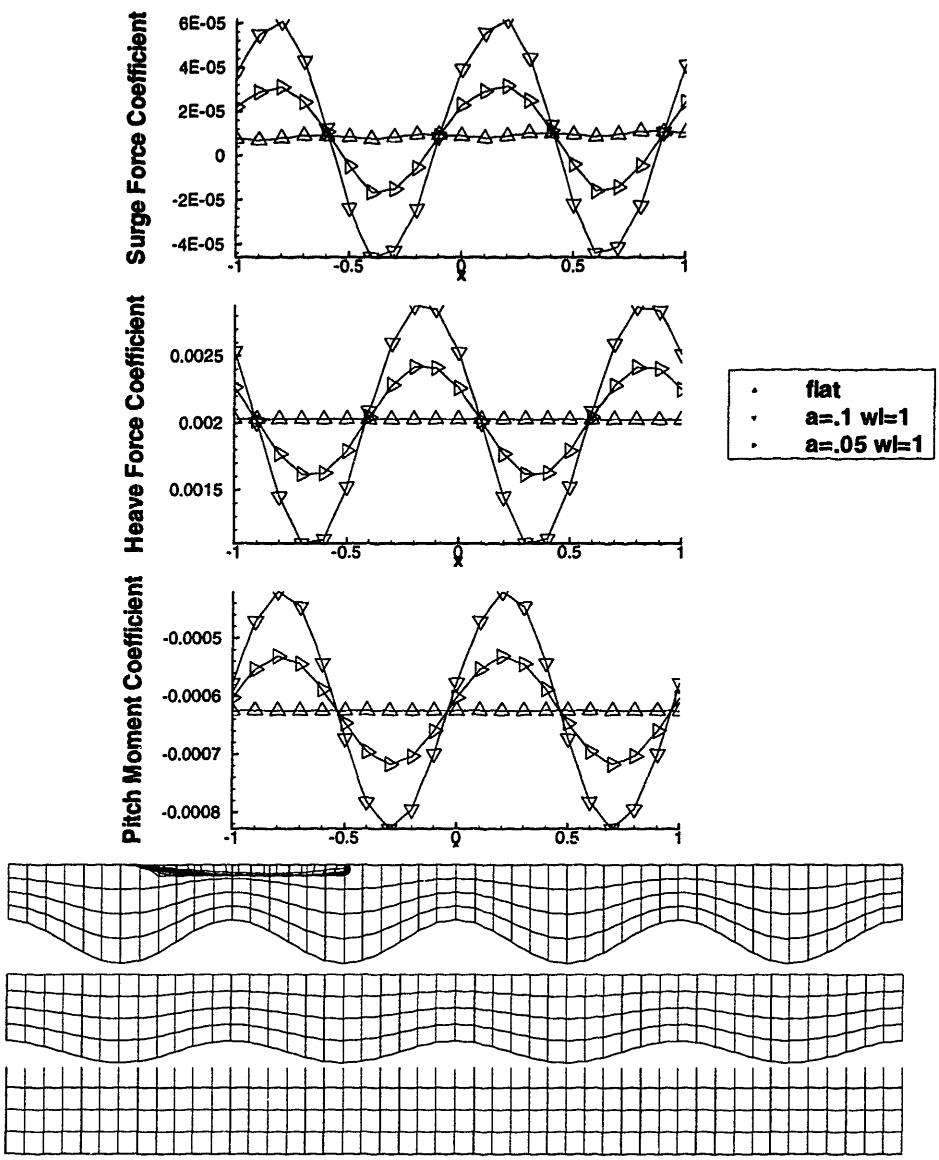

Figure 6-7: Forces on a VLCC in channels with bottom undulations of varying amplitudes. Channel profiles are shown, except for the flat channel.

the surge force implies the sub decelerates quickly as it approaches each undulation. Afterwards it accelerates forward, only to be abruptly slowed by the next undulation. The surge force is 90^o out of phase with the channel topography and surge is in phase with the pitch moment. The heave force is in phase with the channel topography. The sub is seen to climb steadily in the channel, i.e. it slowly surfaces. This is due to the net positive heave force. As it approaches the surface, there is an expected

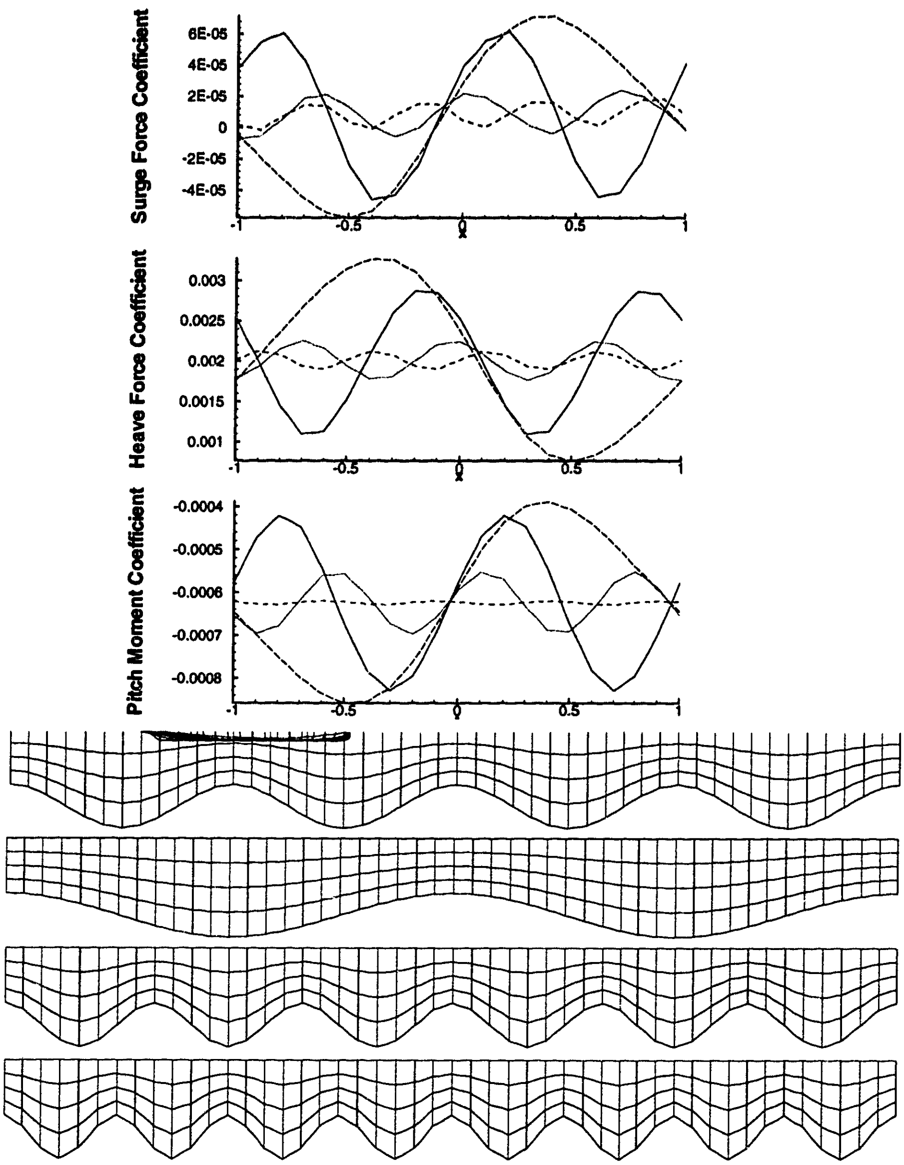

Figure 6-8: Forces on a VLCC in channels with bottom undulations of varying wave lengths. Channel profiles are shown.

decrease in the effect of the undulations. This can be seen in the heave force plot in 6-10 at $x = .5$ where the peak force has diminished compared to the peak force at $x = -.5$. Also affected by the decreasing effect of the channel bottom, the pitch angle steadily increases, though that progress is slowed by the negative pitch moment at $x = -.25$ and $x = .75$. Increases in the pitch angle correspond to the positive peaks in the pitch moment at $x = -.75$ and $x = .25$.

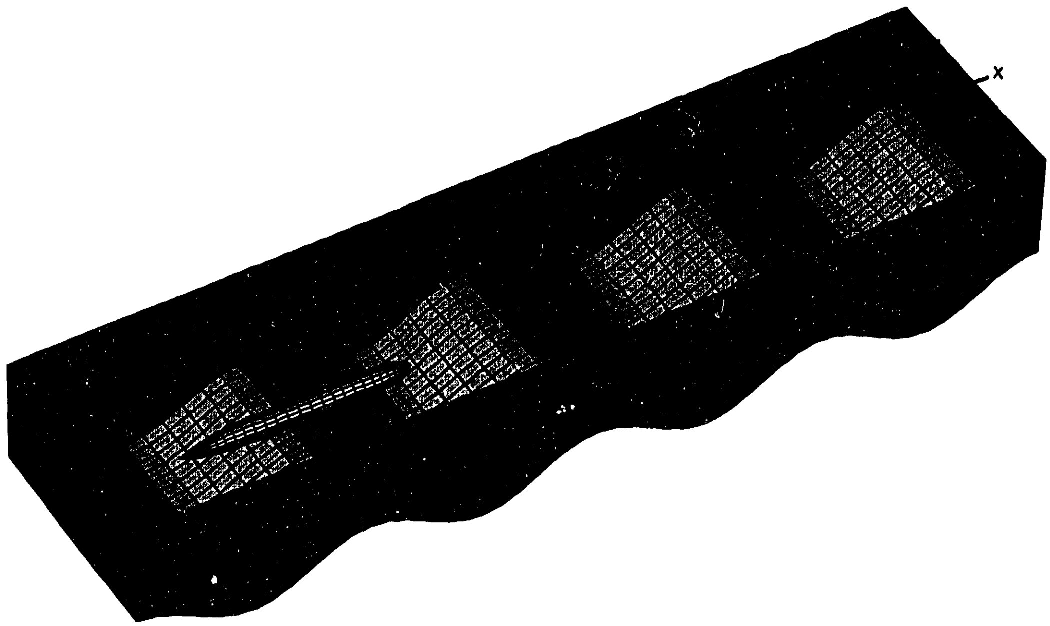

Figure 6-9: Geometry for a 688-class submarine in a channel of mean depth .6 with an undulating bottom of wavelength 1 and amplitude .1.

6.2 Ship Moored with Damped Springs

For this analysis, the rectangular channel code is used. This is necessary due to the very shallow keel clearance for the case we have chosen to study. If done with the general channel code, approximately 640,000 panels would be necessary for a uniform panelization of the bottom.

For this study, the following is the ODE of our forced and damped mass-spring system.

$$[m + m_{ij}]\ddot{x} + [B]\dot{x}_i + [C]x = F_i \tag{6.1}$$

The restoring matrix C must be positive in order for (6.1) to be stable and have bounded solutions as we have written it. For moored vessels, an overdamped case is desired, where

$$\beta = \left(\frac{\frac{1}{2}[B]}{[m + m_{ij}]}\right) - \frac{[C]}{[m + m_{ij}]} \tag{6.2}$$

is positive [17]. A negative value for β represents the underdamped case.

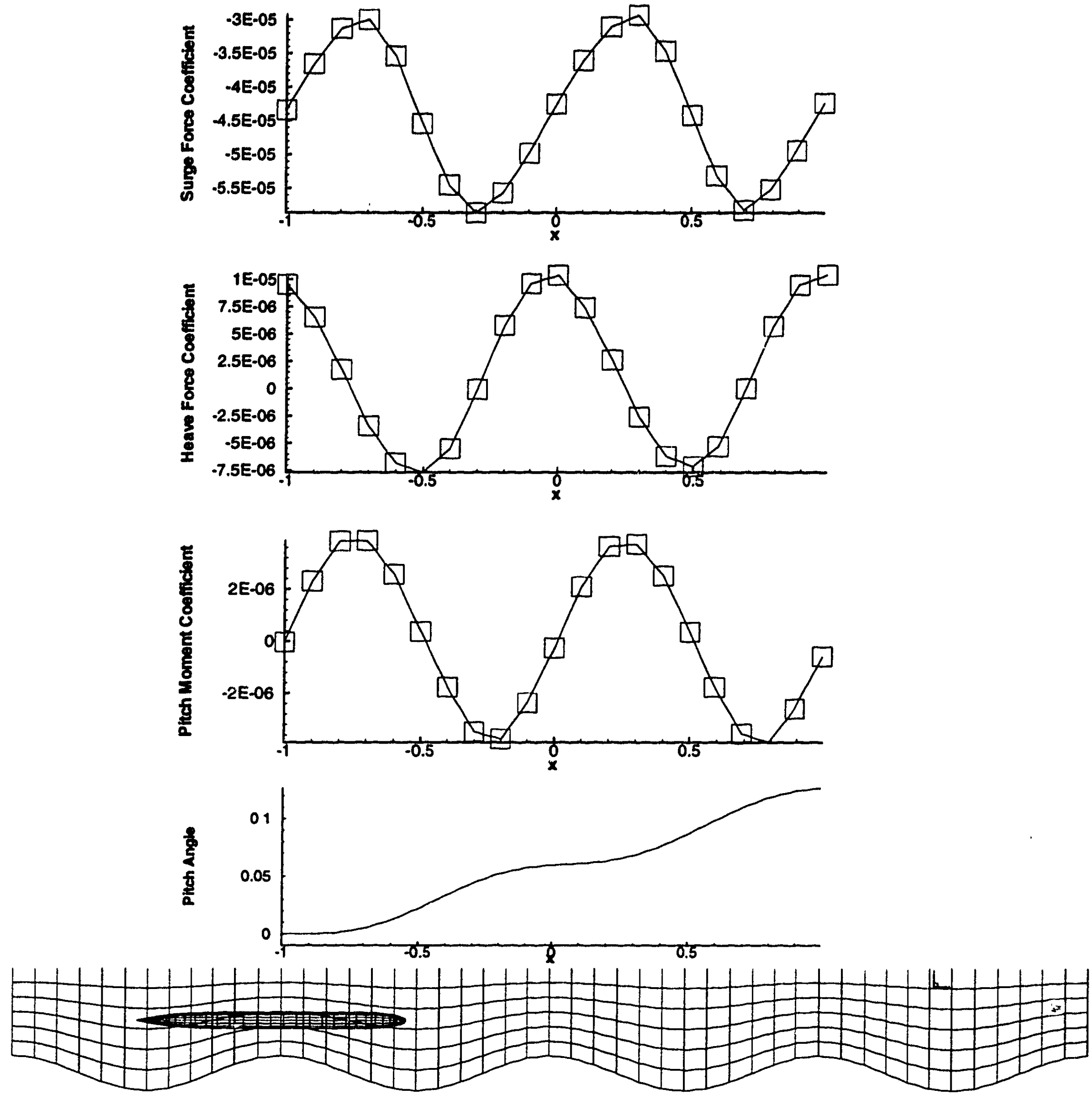

Figure 6-10: Forces, moment and pitch angle for a 688-class submarine in a channel with bottom undulations. Channel profile is shown.

6.2.1 Verification

To confirm damping and restoring were properly included in the equations of motion, the following cases were run. For moored body damping and restoring, the rectangular channel code is used. The test case is two 36 panel hemispheres of diameter .125 in a channel of depth .5. The hemispheres are initially placed at $(-.2, .7, 0, 0, 0)$ and $(0, .3, 0, 0, 180)$ as shown in 6-11 (the channel is shown for reference purposes only).

Time steps of $\Delta t = \{.05, .01, .005, .0025\}$ are used for temporal convergence. The damping and restoring matrices were non-zero only on the diagonal in the body 2 self-influence sub-matrix. The non-zero values were $B = \{0, .01, 1\}$ for the damping matrix and $C = \{0, 1\}$ for the restoring matrix. The restoring matrix was chosen to show unbounded behavior, for the sake of demonstration. For the results comparing damping and restoring, a time step of $\Delta t = .01$ is used. The first hemisphere is given an initial unit velocity, while the second hemisphere has zero initial velocity.

Figure 6-12 shows the time step convergence for the zero-damping/zero-restoring case. The dotted, dashed, long dashed and solid lines represent the time steps of $\Delta t = .05, .01, .005, .0025$, respectively. A time step of .01 is sufficient for converged results. Figure 6-13 shows the time step convergence for the damped and restored case. These results do not converge, though a time step of .01 appears to be stable. For the purposes of this verification, $\Delta t = .01$ is used.

The dotted, dashed, solid lines represent the damping of $B = \{0, .01, 1\}$ and restoring of $C = \{0, 1, 1\}$, respectively. Figure 6-14 shows the surge force on body 2, the x-coordinate of body 2 as a function of the x-coordinate of body 1, and the sway force on body 2 for the different values of damping and restoring. The dotted line shows the undamped and unrestored case. The dashed line shows the case with unit restoring and light damping. The force plots show unstable behavior for the lightly damped case due to the restoring matrix chosen. The solid line shows unit damping, sufficient to damp out the unbounded behavior. The damping is also sufficient to limit the motion of body 2 in surge. This information is sufficient to show that damping and restoring have been properly incorporated into the equations of motion, though it is up to the user to choose damping and restoring matrices suitable for the scenario.

6.2.2 Actual Scenario

The scenario was provided by MacKnight, LTD. in Brisbane, Australia. The rectangular channel code is used for this simulation since the keel clearance would require

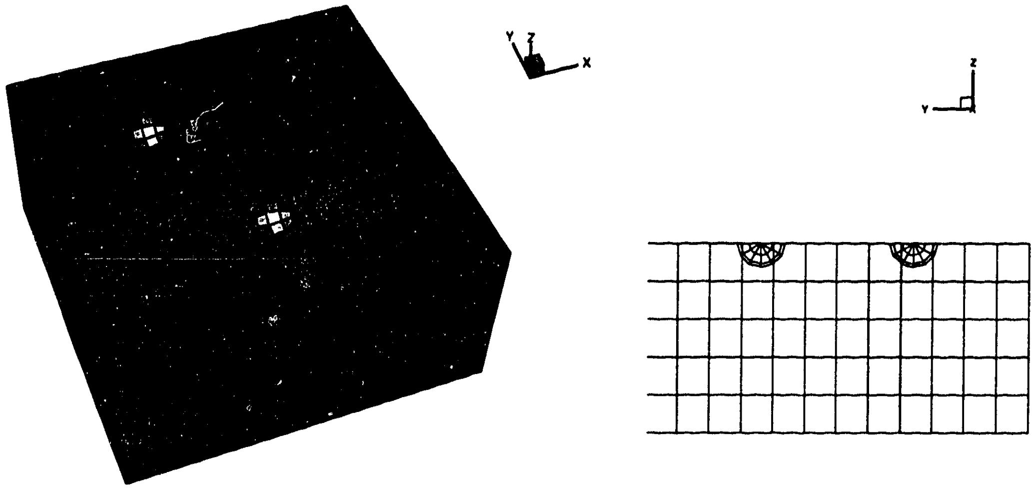

Figure 6-11: Geometry for the damping and restoring test case. The channel is shown as a reference.

640,000 panels if uniformily sized panels are used. The type of ship is not defined but the dimensions are a length of 278 meters, beam of 45m and draft of 15.2m for the moving ship and length, beam and draft of 283m, 47m, and 15.2m for the moored ship. The values for the remainder of this section are normalized on the 278m ship length unless otherwise noted. The depth of the channel is .06 and the width is .971. The initial positions are $(-1.5, .544, 0, 0, 0)$ and $(0, .087, 0, 0, 0)$ respectively as seen in Figure 6-15. This puts the moored vessel next to the channel wall with a clearance of .007 or approximately 2 meters. Caution should be taken to have sufficient panels on a body near a wall, since it will be interacting with its mirror image, and the warnings in §4 hold.

The initial damping matrix provided is

$$\begin{bmatrix} b_{7,7} & b_{7,8} & b_{7,12} \\ b_{8,7} & b_{8,8} & b_{8,12} \\ b_{12,7} & b_{12,8} & b_{12,12} \end{bmatrix} = \begin{bmatrix} 0 & 0 & 0 \\ 0 & .4 & 0 \\ 0 & 0 & .4 \end{bmatrix} \tag{6.3}$$

and the initial non-dimensional stiffness matrix is

$$\begin{bmatrix} c_{7,7} & c_{7,8} & c_{7,12} \\ c_{8,7} & c_{8,8} & c_{8,12} \\ c_{12,7} & c_{12,8} & c_{12,12} \end{bmatrix} = \begin{bmatrix} .263217 & .104171 & .0780801 \\ .104171 & 39.5034 & -.0858429 \\ .0780801 & -.0858429 & 1.88449 \end{bmatrix} \tag{6.4}$$

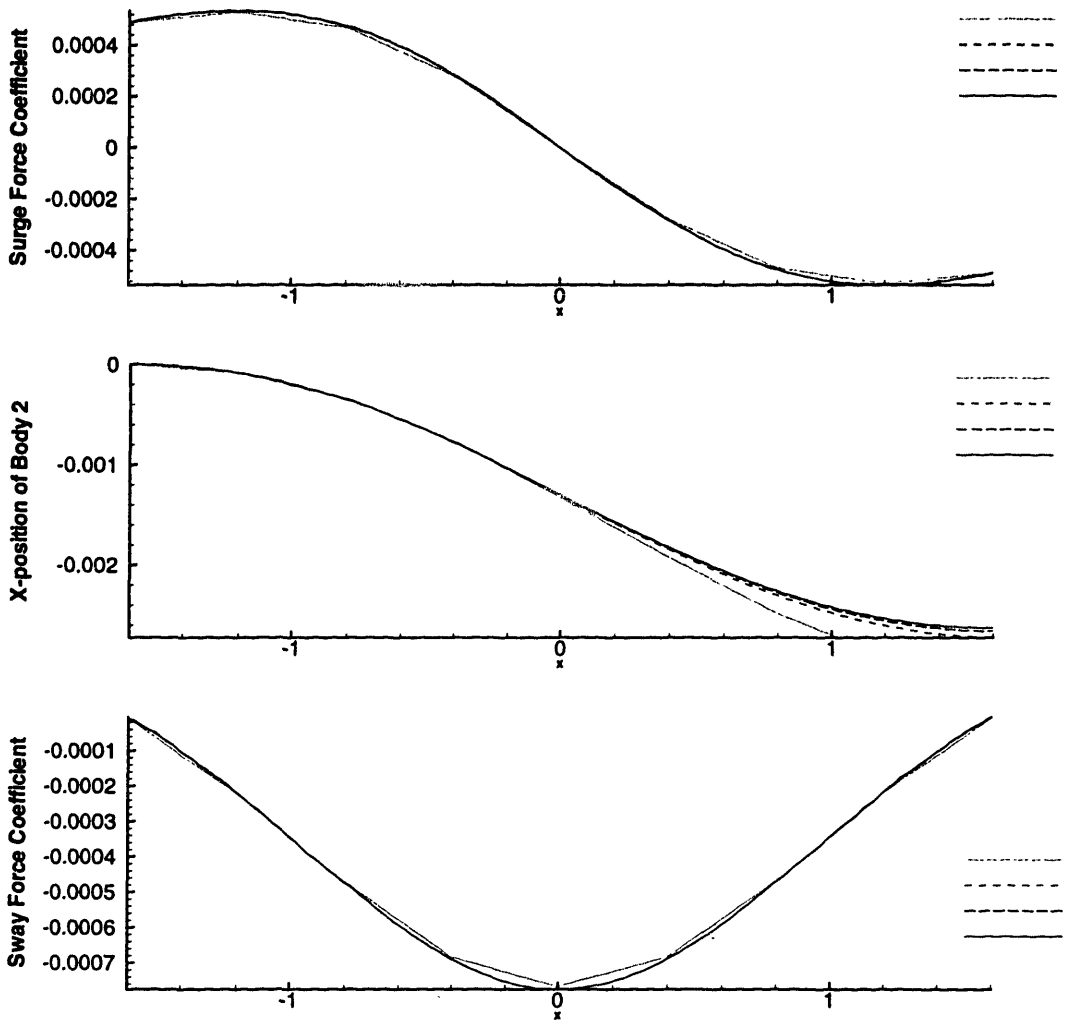

Figure 6-12: Temporal convergence for undamped and unrestored motions in surge and sway modes.

These values are dimensionalized to the length and initial velocity of the passing ship. For this case, $\rho = 998\frac{kg}{m^3}$ $U = 1.66\frac{m}{s}$ and $L = 278m$. Following the analysis surrounding equation (6.2), this system is underdamped in all modes except yaw $(i, j = 12, 12)$ and the coupled terms $i, j = \{12, 7; 12, 8; 8, 12\}$.

The results we were provided were calculated using a post-processor for moored body motions that took forces from a fixed body as input. These results suggest a displacement of between -2.5m and 3.6m from equilibrium in surge, between -.5m and .03m in sway, and between -.0017 and .0053 degrees in yaw are expected. The time step, $\Delta t = .1$ they used, is sufficient for the calculations of forces on a captive

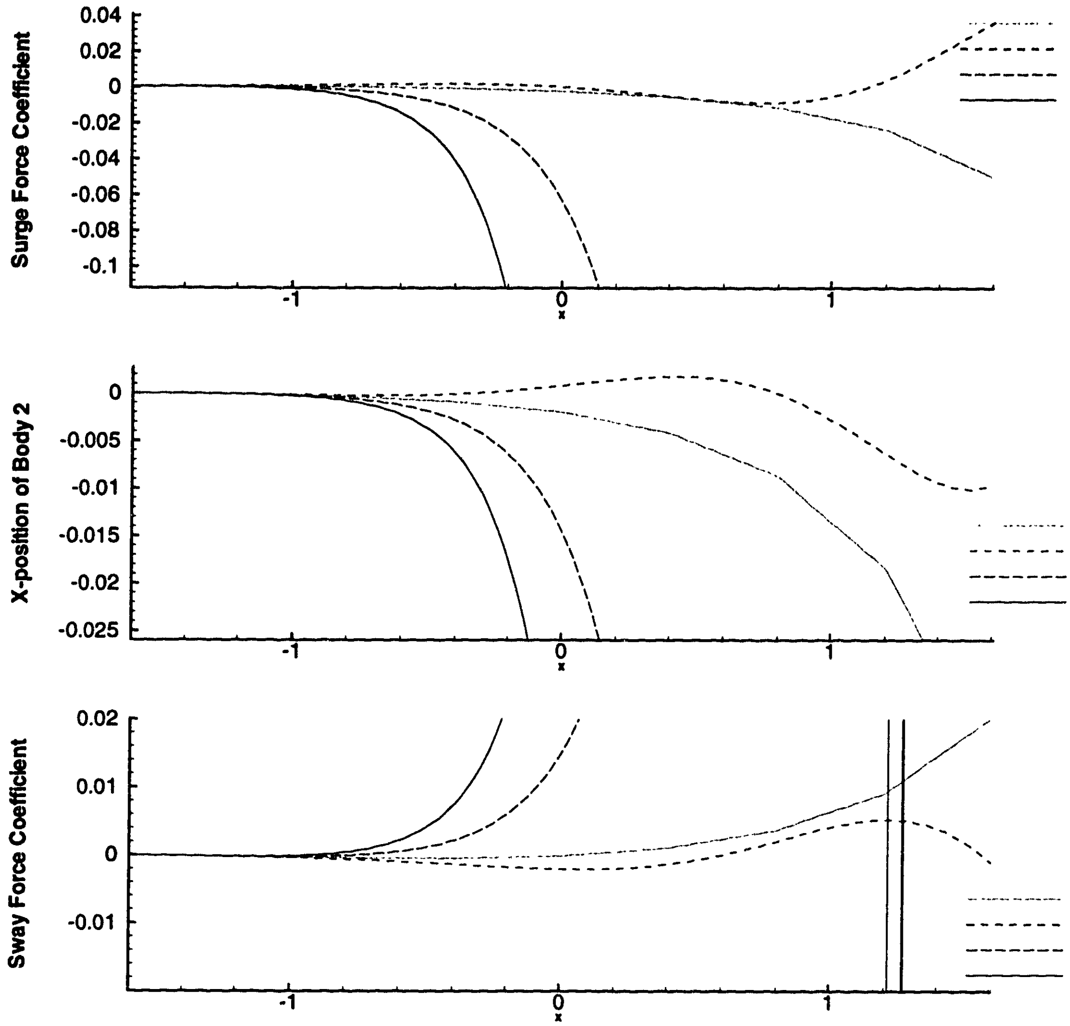

Figure 6-13: Temporal convergence for the damping and restoring of the motions in surge and sway modes.

vessel, but for a solution with body motion, it is too large. In addition, zero damping was used due to numerical stability issues. Numerical tests found yaw to be the least stable mode, i.e. an extremely small time step would be necessary for an accurate and stable solution. The restoring matrix they provide is very stiff in sway. The results for displacements they provide indicate less than 1m total movement in sway. From this, it is reasonable to assume that the hydrodynamic effects of motion in this mode are small and fixing motion for this mode will yield similar results. With surge as the only active mode for the moored vessel, a time step as large as $\Delta t = .01$ was found to

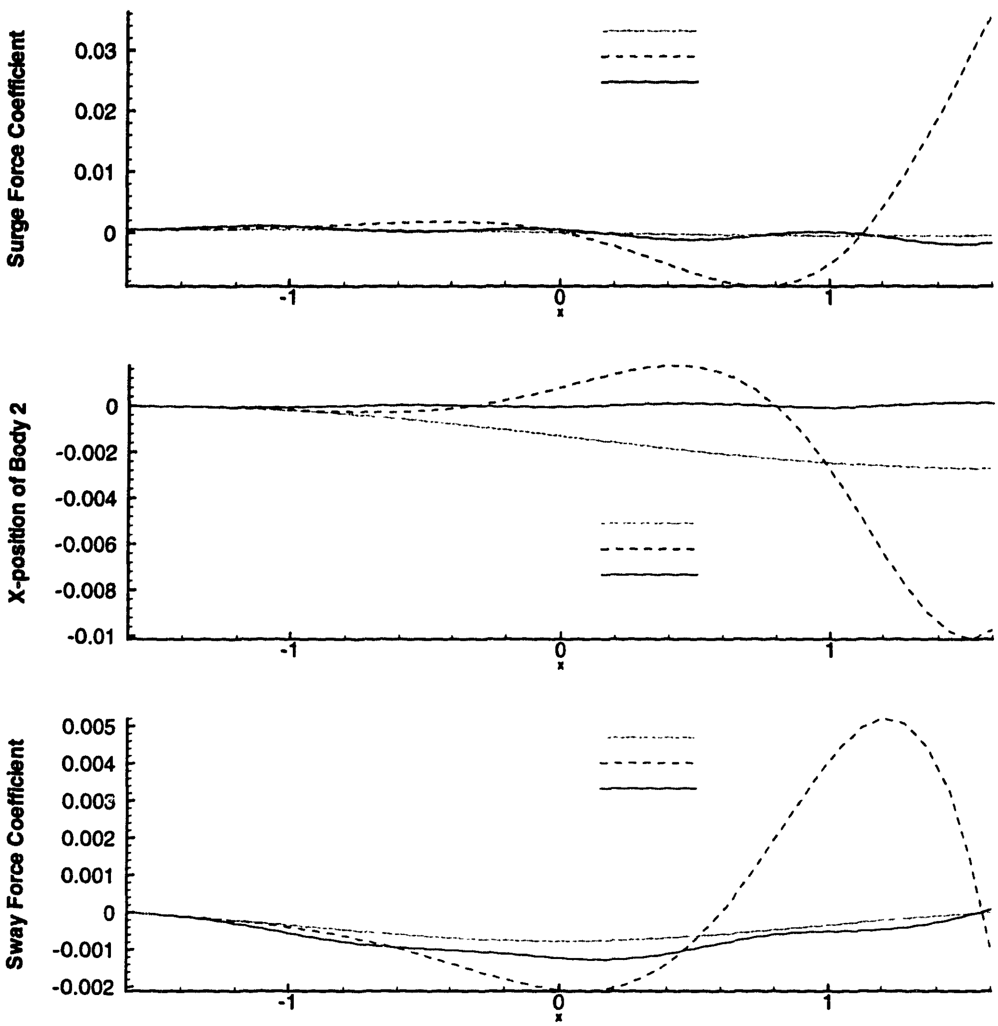

Figure 6-14: Forces and position for body 2 varying the damping and restoring for the surge and sway modes.

be stable. For a time step of $\Delta t = .005$, force results are shown in Figure 6-16. The maximum deflection in surge is $\pm.0003$, or .08m. The peak deflections were -.0001 for a body 1 position of $x = -1.32$, .0003 for $x = -1.12$, and -.0022(.61m) by the end of the run at $x = -.91$. From this, the need for damping is apparent.

With freedom of surge and sway included, a time step as small as $\Delta t = .005$ was not stable. This finding emphasizes the point that due to the high stiffness of the restoring matrix, a very small time step is necessary for accurate motions, or the inclusion of an appropriate damping matrix would overdamp the system, thus allowing for a larger

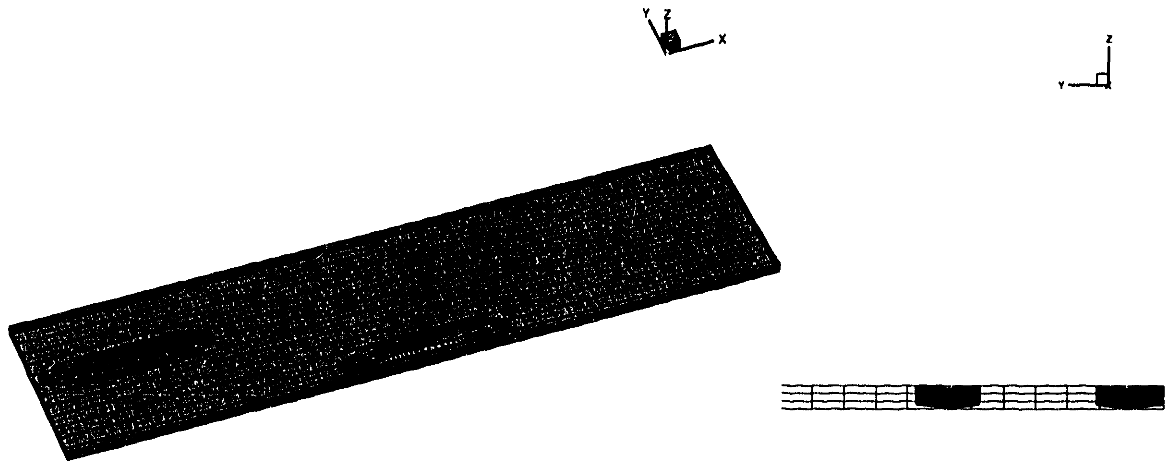

Figure 6-15: Geometry for Macknight simulation configuration. The channel is shown as a reference.

time step. These findings also suggest that for very stiff systems, the method of finding the hydrodynamic forces on a fixed body then post-processing the force data to determine displacements for each mode is a more efficient approach. For more compliant systems and systems with more complex geometries, where hydrodynamics of the moored body and the geometry of the body system are important, this method of including the damping and restoring in the equations of motion should yield a better solution.

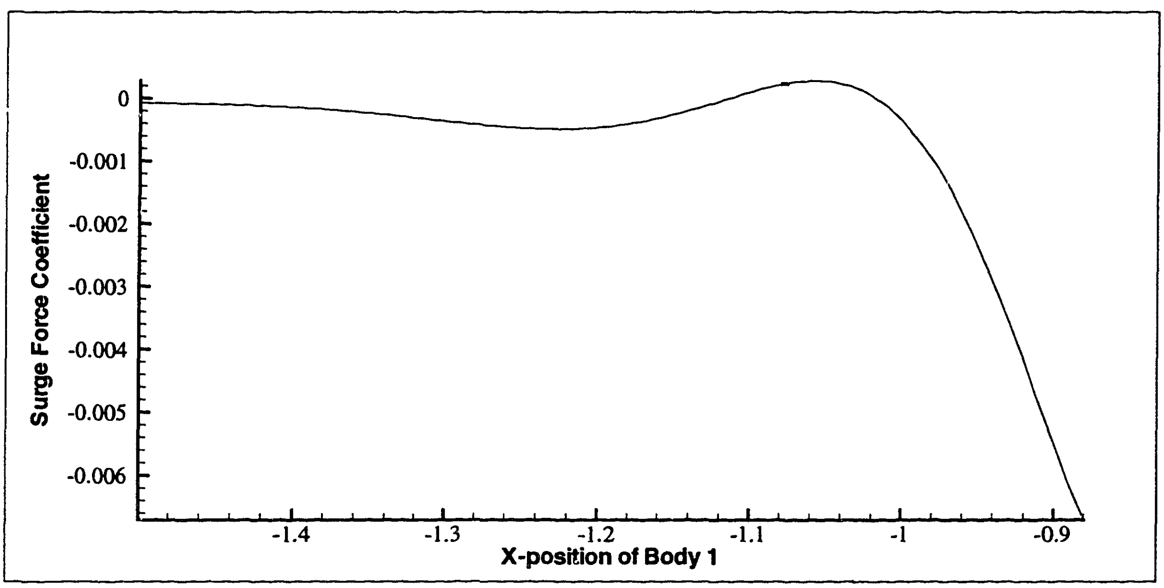

Figure 6-16: Forces on body 2 for the surge-only with restoring case.

Chapter 7

Conclusion

The equations of motion with damping, restoring and 5 degrees of freedom have been implemented in the general channel code. The method of "possible displacement" detailed in [20] was implemented for the computation of the time derivative of the added mass.

Verification of results was performed using existing versions of the channel code, with and without the periodic Green function to satisfy the reflections about the channel walls [13]. Given sufficient panelization, the general channel code was able to reproduce or converge toward previous results. In addition, the results of this code were compared to results in a paper using slender body theory to calculate the sway force and moment of the body moving past a conformally mapped pier [21]. The trends of the force and moment of the ship shown in the figures in the paper were reproduced to sufficient levels, given the geometry and parameters of the case could not be reproduced exactly.

Analysis of disparate body interactions showed the importance of proper discretization of the bodies. The panel method rule-of-thumb of being further than 2 local characteristic panel dimensions from another body, whose basic theory is explained in [22], was repeatedly emphasized. However, another rule-of-thumb, that panels on two bodies in proximity must have similar dimensions, was found lacking. The important factor was found to be the panel area, specifically the ratio of the panel areas on the two bodies, which may be as small as 10^{-3}, but the exact value is geometry dependent. Small bodies passing much larger bodies were found to act as water particles, following the flow streamlines very closely. This result was expected. However, if a small body were to pass within 2 CPD of the larger body, its path would come closer to the larger body than if the "2 CPD limit" had not been violated (Figure 5-10). This would result in more body collisions.

Further study of body motion in channels of arbitrary contour was done: a ship in a stepped channel bottom and in channels with undulating bottoms. For the first scenario, results similar to §4.2.3, the Comparison with Strip Theory with Arbitrary Wall Contour section, were shown, since this geometry is the same with a rotation about the x-axis. Bodies approaching a step will be repelled in surge and pitch as they go over the step, in addition to heaving down as most of the hull comes over the step. A body that is below a step and one half body length away and orthogonal to the step will not notice much difference in force due to a vessel passing over the step.

For the second case, the amplitude of bottom undulations is linearly proportional to the force due to the undulations experienced by a passing vessel. However, the correlation of the wavelength with the force on the passing body is not so clear. For undulations shorter than the length of the passing body, the magnitudes of the forces was low compared to those channels with undulations on the order of the length of the body or longer. The surge and pitch forces were nearly in phase, while the heave force was nearly 180^o out of phase with them. With respect to the undulations of the bottom, the peak heave forces preceeded the peak undulations, except for the shortest undulation wave length; the peak surge forces followed the peaks of the undulations, except for the channel with the shortest undulations, where the surge forces were nearly 180^o out of phase.

Results for a hemisphere passing a moored hemisphere were shown as verification of the damping and restoring method. Non-damped, underdamped and overdamped cases were seen. An experiment with a ship passing a ship moored with damped springs was performed. Due to the high stiffness of the matrix, a very small time step was necessary for stable solutions. The size of the time step almost proved prohibitive. We were unable to reproduce the results provided by Macknight, Ltd., as the moored vessel collided with the channel wall, thus violating the boundary conditions of the problem and causing the simulation to end. However, we were able to show that the surge mode is unstable for the purely restored case, given the restoring matrix used.

The simulations described in this thesis are only a small sample of what the latest version of the general channel code can model. Other interesting scenarios for force and motion analysis may include

- further study of moored vessels;
- further study of forces on a ship and ship motion over arbitrary bottom topography;
- a ship passing a pier extending from a beach with varying slope;
- a ship or submarine over a tunnel in a narrow channel with a sloping beach;
- a ship passing under a bridge connecting 2 land masses;
- a ship passing orthogonal to an inlet bounded by piers or jetties;
- a submarine moving underneath ice.

Chapter 8

Recommendations

The following features are recommended additions to the general channel code, for both robustness and additions to code:

- allow N-bodies in the simulation;
- create a better collision check;
- implement acceleration for potential and source strength problems;
- implement a control system for each of the bodies;
- implement prescribed velocity, acceleration and motion;
- find the pressure on the channel itself;
- further study into discretization styles for the channel in an effort to reduce the total number of panels;
- re-panel the bodies at the free surface so surface piercing bodies with vertical motions can be simulated.

Bibliography

[1] The dangerous attraction of undulating bottoms. Australian Maritime College News, Launceston, Tasmania, March 1997.

[2] G. K. Batchelor. *An Introduction to Fluid Dynamics.* Cambridge University Press, New York, 1977.

[3] S. B. Cohen and R. F. Beck. Experimental and theoretical hydrodynamic forces on a mathematical model in confined waters. *Journal of Ship Research*, 27(2):75–89, June 1983.

[4] Department of Ocean Engineering, Massachusetts Institute of Technology, Cambridge, MA. *TIMIT: A panel-method program for transient wave-body interactions*, 1996.

[5] A. R. Knowlton, F. T. Korsmeyer, and B. Hynes. The hydrodynamic effects of large vessels on right whales: Phase two. Technical Report 98-2, National Marine Fisheries Service, June 1998.

[6] A. R. Knowlton, F. T. Korsmeyer, J. E. Kerwin, H.-Y. Wu, and B. Hynes. The hydrodynamic effects of large vessels on right whales. Technical Report In Fulfillment of Contract No. 40EANFF400534, National Marine Fisheries Service, March 1995.

[7] A. R. Knowlton, S. D. Kraus, D. F. Meck, and M. L. Mooney-Seus, editors. *Shipping/Right Whale Report*, number 97-3 in Aquatic Forum Series, Boston, December 1997. New England Aquarium.

[8] I. M. Korotkin. Battle damage to surface ships during world war ii. Technical Report Translation 310, Leningrad Sudpromgiz, February 1964.

[9] F. T. Korsmeyer, C. H. Lee, and J. N. Newman. Computation of ship interaction forces in restricted waters. *Journal of Ship Research*, 37(4):298–306, December 1993.

[10] L. M. Milne-Thomson. *Theoretical Hydrodynamics.* MacMillan, New York (Fourth Edition), 1960.

[11] J. N. Newman. *Marine Hydrodynamics.* M.I.T. Press, Cambridge, Mass., 1977.

[12] J. N. Newman. Theoretical methods in ship maneuvering. In *Advances in Marine Techonology*, International Symposium on Advances in Marine Techonology, pages 335–359, Trondheim, Norway, June 1979. The Norwegian Institute of Technology.

[13] J. N. Newman. The green function for a rectangular channel. *Journal of Engineering Mathematics*, 26(1):51–59, February 1992.

[14] NMWEA. Navsea mine familiarizer. Technical report, Naval Mine Warfare Engineering Activity, April 1985.

[15] NMWEA. U. S. navy mine countermeasures familiarizer. Technical report, Naval Mine Warfare Engineering Activity, October 1991.

[16] H. Omura, S. Oshumi, T. Nemoto, K. Nasu, and T. Kasuya. *Black Right Whales in the North Pacific*, volume 21. Sci. Rep. Whales Res. Inst., Tokyo, 1969.

[17] R. Redheffer. *Introduction to Differential Equations.* Jones and Bartlett, Boston, 1992.

[18] G. F. M. Remery. Mooring forces induced by passing ships. In *Sixth Annual Offshore Technology Conference*, pages 349–363, Dallas, Texas, May 1974.

[19] E. O. Tuck and J. N. Newman. Hydrodynamic interactions between ships. In *10th Symposium on Naval Hydrodynamics*, pages 35–58, 1974.

[20] H.-Y. Wu. Simulation of the hydrodynamic interaction of bodies. Master's thesis, Massachusetts Institute of Technology, Department of Ocean Engineering, February 1995.

[21] R. W. Yeung and W. T. Tan. Hydrodynamic interactions of ships with fixed obstacles. *Journal of Ship Research*, 24(1):50–59, March 1980.

[22] R. Zhao and O. Faltinsen. A discussion of the m_{ij}-terms inthe wave-current-body interaction problem. In J. Grue, editor, 4^{th} *International Workshop on Water Waves and Floating Bodies*, pages 275–279, Oystese, Norway, May 1989. University of Oslo, Norway.